

1

Title goes here

2

Bálint Balázs

3



4

Pázmány Péter Catholic University

5

Faculty of Information Technology

6



7

European Molecular Biology Laboratory

8

Supervisors: Lars Hufnagel, *PhD*, Balázs Rózsa, *MD, PhD*

9

A thesis submitted for the degree of

10

Doctor of Philosophy

11

2017

¹ Abstract

² Abstract in English.

¹ Tartalmi kivonat

² Absztrakt magyarul.

Contents

1	Abstract	iii
2	Tartalmi kivonat	v
3	List of Figures	x
4	List of Tables	xi
5	Introduction	1
6	1 Live imaging in three dimensions	3
7	1.1 Wide-field fluorescence microscopy	4
8	1.2 Point scanning methods	10
9	1.3 Light-sheet microscopy	14
10	1.4 Light-sheet microscopy for mouse imaging	22
11		
12	2 Dual Mouse-SPIM	29
13	2.1 Microscope design concept	29
14	2.2 Optical layout	33
15	2.3 Optical alignment	38
16	2.4 Control unit	42
17	2.5 Results	45
18	2.6 Methods	52
19	2.7 Conclusions	53
20	3 Image processing for multi-view microscopy	55
21	3.1 Multi-view image fusion	55
22	3.2 Image compression	56
23	3.3 Noise in light microscopy images	59

CONTENTS

1	4 Real-time, GPU accelerated image processing pipeline	61
2	4.1 Challenges in data handling for light-sheet microscopy	61
3	4.2 Live fusion	62
4	4.3 B³D image compression	67
5	4.4 Noise dependent lossy compression	69
6	4.5 Methods	70
7	5 Discussion	77
8	5.1 New scientific results	77
9	Acknowledgements	79
10	Appendix A Bill of materials	81
11	Appendix B Appendix B	83
12	Appendix C Light collection efficiency of an objective	87
13	References	89

¹ List of Figures

2	1.1	Tradeoffs in fluorescence microscopy for live imaging	4
3	1.2	Excitation and emission spectrum of enhanced green fluorescent protein (EGFP)	5
4	1.3	Wide-field fluorescence microscope	7
5	1.4	Axial cross section of the PSF and OTF of a wide-field microscope	8
6	1.5	Airy pattern	9
7	1.6	Resolution of a wide-field microscope	11
8	1.7	Basic optical components of a confocal laser scanning and confocal-theta microscope	12
9	1.8	Axial cross section of the PSF and OTF of a confocal laser scanning mi- croscope	13
10	1.9	Basic concept of single-plane illumination microscopy	15
11	1.10	Different optical arrangements for light-sheet microscopy	16
12	1.11	Basic optical components of a SPIM	17
13	1.12	Light-sheet dimensions	19
14	1.13	DSLM illumination	21
15	1.14	Inverted light-sheet microscope for multiple early mouse embryo imaging.	24
16	1.15	Imaging mouse post-implantation development	25
17	1.16	Imaging adult mouse brain with light-sheet microscopy.	26
18	2.1	Dual view concept with high NA objectives	30
19	2.2	Lateral and axial resolution of a multi-view optical system.	31
20	2.3	The core unit of the microscope	34
21	2.4	Illumination branch splitting unit	36
22	2.5	Dual Mouse SPIM optical layout	37
23	2.6	Detection branch switching unit	39
24	2.7	Microscope control hardware and software architecture	43
25	2.8	Digital and analog control signals	44
26	2.9	Completed DualMouse-SPIM	45

LIST OF FIGURES

1	2.10 Stability measurements of view switcher unit	46
2	2.11 Illumination beam profile	47
3	2.12 Simulated and measured PSF of Dual Mouse-SPIM	49
4	2.13 Combined PSF of 2 views	50
5	2.14 Maximum intensity projection of a <i>Drosophila melanogaster</i> embryo recording	51
6	2.15 Multi-view recording of a mouse zygote	51
7		
8	3.1 Building the binary Huffman tree	58
9		
10	4.1 Experiment sizes and data rate of different imaging modalities	62
11	4.2 Real-time image processing pipeline for multi-view light-sheet microscopy	62
12	4.3 Operating principle of MuVi-SPIM	63
13	4.4 Multi-view fusion methods for light-sheet microscopy	65
14	4.5 Classes of LVCUDA library	66
15	4.6 GPU fused images of a <i>Drosophila melanogaster</i> embryo. Two stacks were taken in quick succession first without fusion, then with fusion enabled. Fused images are shown in the middle of each subfigure, while the individual camera images are in the bottom insets. The top-left inset depicts the z-position of the shown images. a) Image from closer to the left camera.	
16	b) Image from the center of the embryo. c) Image from closer to the right camera.	67
17		
18	4.7 B ³ D algorithm schematics	69
19	4.8 Lossless compression performance	70
20	4.9 Options for noise dependent lossy compression	71
21	4.10 Within noise level compression performance	72
22	4.11 Image quality of a WNL compressed dataset	72
23	4.12 Compression error compared to image noise	73
24	4.13 Influence of noise dependent lossy compression on 3D nucleus segmentation	73
25	4.14 Influence of noise dependent lossy compression on 3D membrane segmentation	74
26	4.15 Influence of noise dependent lossy compression on single-molecule localization	74
27	4.16 Change in localization error only depends on selected quantization step	75
28		
29	C.1 Light collection efficiency of an objective	88
30		
31		
32		
33		

¹ List of Tables

2	3.1 Examples of a random binary code (#1) and a prefix-free binary code (#2)	57
3	3.2 Huffman code table	58
4	3.3 Huffman code table	59
5	B1 Data sizes in microscopy	83
6	B2 Lossless compression performance	84
7	B3 Datasets used for benchmarking compression performance	85

LIST OF TABLES

¹ Introduction

² Coming soon.

INTRODUCTION

¹ Chapter 1

² Live imaging in three dimensions

³ Unraveling the secrets of mammalian development has been a long standing challenge
⁴ for developmental biologists and medical professionals alike. This phase of early life is
⁵ an incredibly complex and dynamic process spanning through large scales in space and
⁶ time. Subcellular processes at the nanoscale are happening in the range of milliseconds
⁷ or faster, while whole embryo reorganizations and tissue migration events take place
⁸ over the course of hours [1]. Resolving these processes presents a true challenge, since
⁹ to understand the underlying mechanisms, molecular specificity is just as crucial as high
¹⁰ spatial and temporal resolution.

¹¹ Light microscopy is one of the oldest methods that is still widely used today to
¹² investigate the inner workings of microscopic life. A particularly important branch is
¹³ fluorescence microscopy [2], that relies on using fluorescent labels to mark specific regions
¹⁴ inside the specimens. Light-sheet microscopy is a relatively new addition to the arsenal of
¹⁵ tools that comprise light microscopy methods, and is especially suitable for live imaging
¹⁶ of embryonic samples over extended periods of time [3–6]. It is also easily adapted to
¹⁷ the sample, allowing to image a large variety of specimens, from entire organs, such as
¹⁸ cleared mouse brains [7], to the subcellular processes occurring inside cultured cells [8].

¹⁹ In an ideal setting, the ultimate microscope would be able to record a continuos,
²⁰ 3D, and multicolor dataset of any biological process of interest with the highest possible
²¹ resolution. Unfortunately this is not possible; due to several limitations in physics and
²² biology, a compromise is necessary. The diffractive nature of light, the lifetime of fluo-
²³ rescent probes and the photosensitivity of biological specimens all require microscopy to
²⁴ be able to adapt to answer the question at hand. In order to acquire useful data one has
²⁵ to choose a tradeoff between spatial and temporal resolution, and signal contrast, while
²⁶ making sure the biology is not affected by the imaging process itself (Fig. 1.1) [9].

1. LIVE IMAGING IN THREE DIMENSIONS

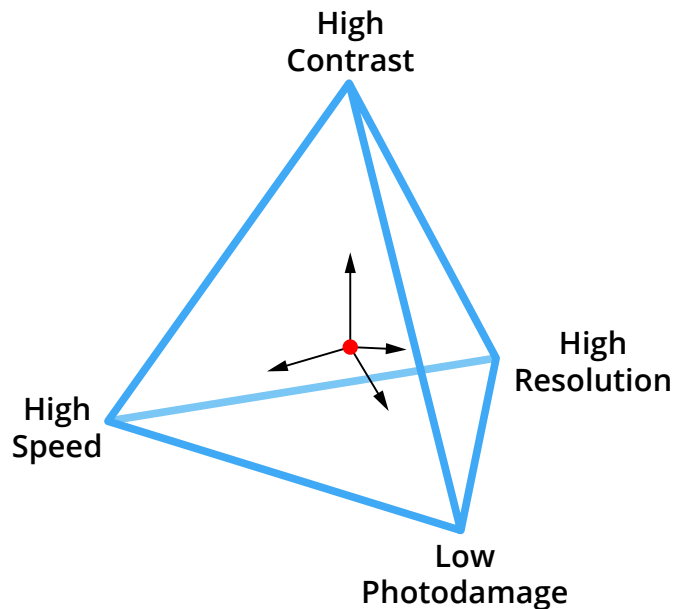


Figure 1.1: Tradeoffs in fluorescence microscopy for live imaging. Also called the “pyramid of frustration”. When optimizing the imaging conditions (red dot), a tradeoff has to be made between resolution, contrast, and imaging speed, while avoiding photodamage. One can only be improved at the expense of the others due to the limited photon budget of the fluorescent molecules. Adapted from [9].

¹ 1.1 Wide-field fluorescence microscopy

² Fluorescence microscopy [2, 10], as a subset of light microscopy is one of the few methods
³ that allows subcellular imaging of live specimens. The first use of the term fluorescence is
⁴ credited to George Gabriel Stokes [11], and it refers to the phenomenon when a molecule
⁵ emits light after absorbing light or other electromagnetic radiation. As the name of the
⁶ technique suggests, this method collects fluorescent light from the specimens which has
⁷ numerous advantages, but also some drawbacks. Since biological tissue is usually not
⁸ fluorescent, except for some autofluorescence at shorter wavelengths, fluorescent dyes or
⁹ proteins have to be introduced to the system in order to be able to collect the necessary
¹⁰ information. The advantage of this is that the signal of the labeled structures will be of
¹¹ very high ratio compared to the background.

¹² A fluorescent molecule is capable of absorbing photons in a given range (excitation
¹³ spectrum) and temporarily store its energy by having an electron in a higher energy
¹⁴ orbital, *i.e.* in an excited state. This excited state, however, is not stable, and the electron
¹⁵ quickly jumps back to the ground state while emitting a photon with equal energy to the
¹⁶ energy difference between the excited and ground states. The energy of the absorbed and
¹⁷ emitted photons are not the same, as energy loss occurs due to internal relaxation events,
¹⁸ and the emitted photon has lower energy than the absorbed photon. This phenomenon
¹⁹ is called the Stokes shift, or red shift, and can be exploited in microscopy to drastically
²⁰ increase the signal to noise ratio by filtering out the illumination light (Fig. 1.2).

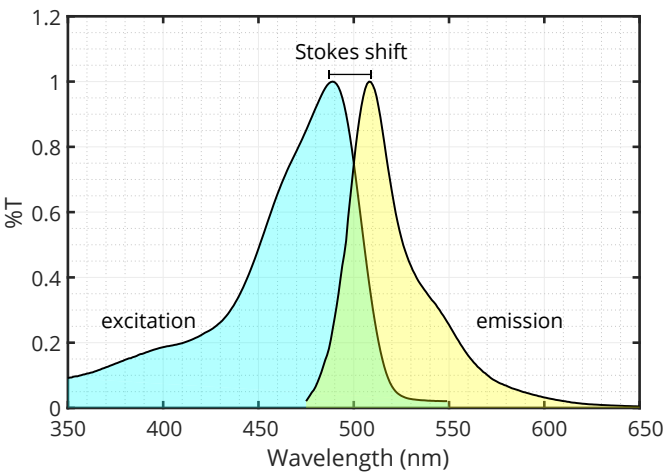


Figure 1.2: Excitation and emission spectrum of enhanced green fluorescent protein (EGFP). Excitation spectrum in blue, emission spectrum in yellow. The separation between the two spectra is due to the Stokes shift, which is 19 nm for EGFP. Emitted and excitation light can be separated by a long-pass filter at 500 nm. Data from [12].

¹ 1.1.1 Fluorescent proteins

² Traditionally, synthetic fluorescent dyes were used to label certain structures in the specimens.
³ Some of these directly bind to their target, and others can be used when conjugated
⁴ to an antibody specific to the structure of interest. The drawback of these methods is
⁵ that the fluorescent label has to be added to the sample from an external source, and, in
⁶ many cases, this also necessitates sample preparation techniques incompatible with live
⁷ imaging, such as fixation [13].

⁸ The discovery of fluorescent proteins have revolutionized fluorescence microscopy.
⁹ Since these molecules are proteins, they can be produced directly by the organism if
¹⁰ the proper genetic modifications are performed. Even though this was a hurdle at the
¹¹ time of discovering the green fluorescent protein (GFP) [14], the first of its kind, genetic
¹² engineering techniques evolved since then [15], and not only has it been successfully
¹³ integrated in the genome of nematodes [16], zebrafish [17], and mice [18], but many
¹⁴ variants have been also engineered by introducing mutations to increase fluorescence
¹⁵ intensity, and to change the fluorescence spectrum to allow multicolor imaging [18–21].
¹⁶ The usefulness and impact of these proteins are so profound, that in 2008 the Nobel
¹⁷ Prize in chemistry was awarded to Osamu Shimomura, Martin Chalfie, and Roger Tsien
¹⁸ “for the discovery and development of the green fluorescent protein, GFP” [22].

¹⁹ 1.1.2 Wide-field image formation

²⁰ By imaging fluorescently labelled specimens, a wide-field fluorescence microscope has the
²¹ capability of discriminating illumination light from fluorescent emitted light due to the
²² Stokes shift described in the previous section. The microscope’s operating principle is

1. LIVE IMAGING IN THREE DIMENSIONS

¹ depicted in Figure 1.3.

² A light source, typically a mercury lamp is focused on the back focal plane of the
³ objective to create even illumination at the sample. Before entering the objective, the
⁴ light is filtered, so only the wavelengths that correspond to the excitation properties
⁵ of the observed fluorophores are transmitted. Since the same objective is used for both
⁶ illumination and detection, a dichroic mirror is utilized to decouple the illumination
⁷ and detection paths. The emitted light is filtered again to make sure any reflected and
⁸ scattered light from the illumination source is blocked to increase signal to noise ratio.
⁹ Finally, the light is focused by a tube lens to create a magnified image in the camera
¹⁰ sensor.

¹¹ This type of imaging is called infinity corrected optics, since the back focal point of
¹² the objective is in “infinity”, meaning that the light exiting the back aperture is parallel.
¹³ This is achieved by placing the sample exactly at the focal point of the objective. Infinity
¹⁴ corrected optics has the advantage that it allows placing various additional optical
¹⁵ elements in the infinity space (*i.e.* the space between the objective and the tube lens)
¹⁶ without affecting the image quality. In this example such elements are the dichroic mirror
¹⁷ and the emission filter.

¹⁸ The combination of the objective and tube lens together will determine the magnifi-
¹⁹ cation of the system, it will be the ratio of the focal lengths of these lenses:

$$M = \frac{f_{TL}}{f_{OBJ}}. \quad (1.1)$$

²⁰ The final field of view (FOV) of the microscope will depend on the magnification, and
²¹ also on the size of the imaging sensor (D), and the objective field number (FN):

$$FOV = \frac{\min(D, FN)}{M}. \quad (1.2)$$

²² Apart from magnification, the most important property of the objective is the half-
²³ angle of the light acceptance cone, α (Figure 1.3, inset). This not only determines the
²⁴ amount of collected light, but also the achievable resolution of the system (see subsec-
²⁵ tion 1.1.3). This angle depends on the size of the lens relative to its focal length. In
²⁶ other words depends on the aperture of the lens, which is why the expression *numerical*
²⁷ *aperture* (NA) is more commonly used to express this property of the objective:

$$NA = n \cdot \sin \alpha. \quad (1.3)$$

²⁸ For small α angles, the following approximation holds true: $\sin \alpha \approx \tan \alpha \approx \alpha$. Thus,
²⁹ the numerical aperture can also be expressed as a ratio of the radius of the lens and the

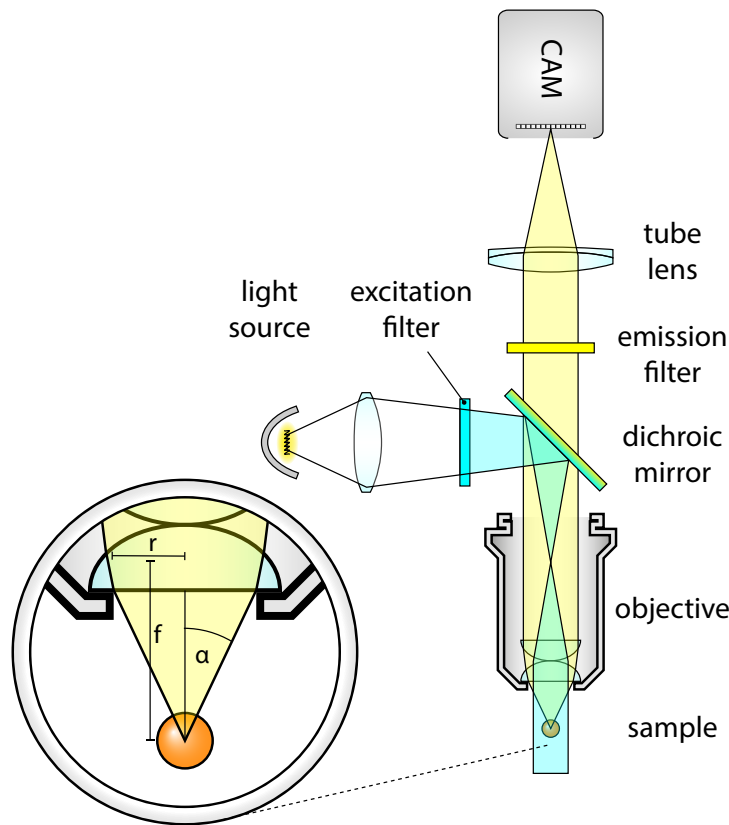


Figure 1.3: Wide-field fluorescence microscope. The light source is focused on the back focal plane of the objective to provide an even illumination to the sample. Emitted photons are collected by the objective, and are separated from the illumination light by a dichroic mirror. Inset: Light collection of an objective lens. α : light collection half-angle; f : focal length; r : radius of lens.

¹ focal length:

$$NA \approx n \frac{r}{f}, \quad \text{when } \alpha \ll 1. \quad (1.4)$$

² 1.1.3 Resolution of a wide-field microscope

³ The resolution of an optical systems is defined by the size of the smallest distinguishable
⁴ feature on the image. Practically this means the minimum distance between two point-
⁵ like objects so that the two objects can still be resolved. This mainly depends on two
⁶ factors: the NA of the objective, and the pixel size of the imaging sensor.

⁷ Even if the imaging sensor would have infinitely fine resolution, it is not possible to
⁸ reach arbitrary high resolutions due to the wave nature of light and diffraction effects
⁹ that occur at the aperture of the objective. This means that depending on the wavelength
¹⁰ of the light, any point source will have a finite size on the image, it will be spread out,
¹¹ that will limit the resolution. The shape of this image is called the *point spread function*,
¹² or PSF (Fig. 1.4), as this function describes the behavior of the optical system when
¹³ imaging a point like source. This property of lenses was already discovered by Abbe in

1. LIVE IMAGING IN THREE DIMENSIONS



Figure 1.4: Axial cross section of the PSF and OTF of a wide-field microscope. Simulated PSF and OTF for a wide-field microscope with a water immersion objective ($n = 1.33$). $NA = 1.1$, $\lambda = 510\text{ nm}$

¹ 1873 [23], when he constructed his famous formula for resolution:

$$\delta = \frac{\lambda}{2 \cdot NA}. \quad (1.5)$$

² where d is the smallest distance between two distinguishable features.

³ Another representation of the optical performance, is the *optical transfer function*,
⁴ or OTF (Fig. 1.4), which is the Fourier transform of the PSF:

$$\text{OTF} = \mathcal{F}(\text{PSF}). \quad (1.6)$$

⁵ As this function operates in the frequency space, it describes how the different frequencies
⁶ are affected by the system. The resolution can also be defined as the support of the OTF,
⁷ since this describes the highest frequency that is still transmitted through the optical
⁸ system. Any pattern with higher frequency will be lost, thus beyond the resolution limit.
⁹ For circularly symmetric PSFs, the OTF will be real valued, however if this is not the
¹⁰ case, the Fourier transform also introduces complex components.

¹¹ Abbe's formula can be derived from the scalar theory of diffraction using a paraxial
¹² approximation (Fraunhofer diffraction, [24]) that describes the intensity of the electric
¹³ field in the focus of a lens [25]:

$$H(u, v) = C_0 \left| \int_0^1 J_0(vr) e^{-i\frac{1}{2} \cdot ur^2} r dr \right|^2, \quad (1.7)$$

¹⁴ where C_0 is a normalization constant, and J_0 is the zero order Bessel function of the first
¹⁵ kind. Furthermore, instead of the commonly used Cartesian coordinates x , y and z , the

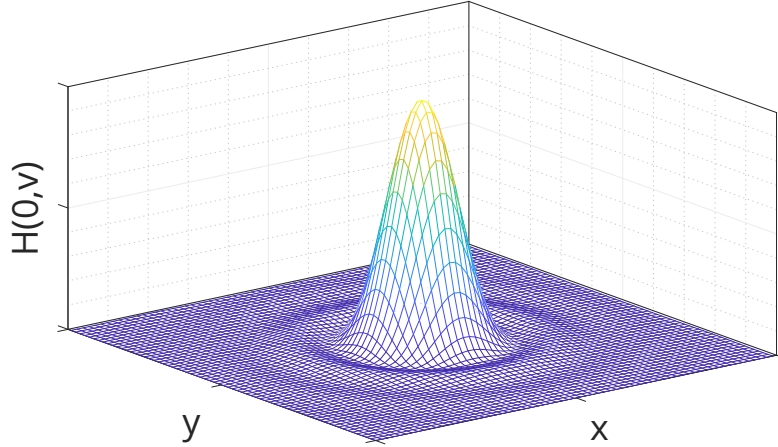


Figure 1.5: Airy pattern. Airy pattern calculated in Matlab based on Eq. 1.9

1 following optical coordinates are defined:

$$v = \frac{2\pi nr}{\lambda_0} \sin \alpha, \quad u = \frac{8\pi nz}{\lambda_0} \sin^2 \frac{\alpha}{2} \quad (1.8)$$

2 where $r = \sqrt{x^2 + y^2}$ is the distance from the optical axis, and α is the light collection
3 angle as shown on Fig. 1.3.

4 To determine the lateral resolution of the system, let's substitute $u = 0$ as the axial
5 optical coordinate, and evaluate Eq. 1.7 which will give the intensity distribution in the
6 focal plane:

$$H(0, v) = C_0 \left| \int_0^1 J_0(vr) r dr \right|^2 = \left(2 \frac{J_1(v)}{v} \right)^2, \quad (1.9)$$

7

8 where J_1 is the first order Bessel function of the first kind. This equation describes
9 the famous Airy pattern (Fig. 1.5) which will be the shape of the PSF in the focal plane.
10 The width of this pattern is the resolution, and although there are multiple definitions
11 for this, the most commonly accepted is the Rayleigh criterion [24, 26] which defines the
12 resolution as the distance between the central peak and the first local minimum. As this
13 lies at $v = 3.83$, the resolution can be expressed by substituting this value to Eq. 1.8 and
14 calculating the real distance (r):

$$\delta_{xy} = \frac{3.83}{2\pi} \frac{\lambda_0}{n \cdot \sin \alpha} \approx 0.61 \frac{\lambda_0}{NA}, \quad (1.10)$$

15 which is equivalent to Abbe's original formula (Eq. 1.5). The only difference is the scaling
16 factor which is due to the slightly different interpretations of width of the Airy disk as
17 mentioned earlier.

1. LIVE IMAGING IN THREE DIMENSIONS

1 Similarly, to calculate the intensity distribution along the axial direction, let's sub-
2 stitute $v = 0$ to Eq. 1.7:

$$H(u, 0) = C_0 \left(\frac{\sin \frac{u}{4}}{\frac{u}{4}} \right)^2. \quad (1.11)$$

3 For this expression the first minimum lies at $u = 4\pi$. Converting back to Cartesian
4 coordinates, the axial resolution can be expressed as:

$$\delta_z = \frac{2n\lambda_0}{NA^2}. \quad (1.12)$$

5 So far we only considered a single, point-like emitter. As the intensity function de-
6 scribes how an optical system “spreads out” the image of a point, it is also called the
7 Point Spread Function (PSF, Fig. 1.4). In a more realistic scenario, however the emitters
8 are neither point-like, nor single. Effectively, however, for every emitter the PSF would
9 be imaged on the sensor, and this creates the final image. In mathematical terms, this can
10 be expressed as a convolution operation between the underlying fluorophore distribution
11 of the object (O) and the PSF (H):

$$I(u, v) = O(u, v) * H(u, v). \quad (1.13)$$

12 The effective result of this kind of diffraction limited image formation is a blurred
13 image with a finite resolution of δ_{xy} in the lateral direction, and δ_z in the axial direction.

14 The PSF is further affected by the illumination pattern as well. Since the number of
15 emitted fluorescent photons are roughly proportional to the illumination intensity, if the
16 illumination has any structure at the order of the detection resolution, it will have an
17 effect on the overall PSF of the system, which can be expressed as:

$$H_{sys} = H_{ill} \cdot H_{det}, \quad (1.14)$$

18 where H_{ill} is the point spread function of the illumination, and H_{det} is the point spread
19 function of the detection.

20 1.2 Point scanning methods

21 In most cases, a wide-field microscope is used to image a section of a tissue, thus axial
22 resolution is not a concern. Imaging live specimens, however is not so straightforward,
23 as these samples are usually much thicker than a typical section. For these samples 3-
24 dimensional (3D) imaging is highly beneficial, which necessitates some kind of optical
25 sectioning technique to be able to discriminate the features at different depths.

26 Due to the design of the wide-field microscope, any photons emitted from outside the
27 focal plane will also be detected by the sensor, however as these are not originating from

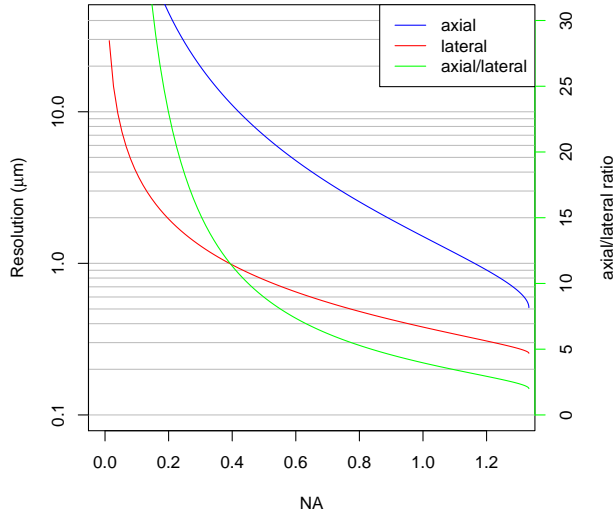


Figure 1.6: Resolution of a wide-field microscope. Axial (blue) and lateral (red) resolutions of a wide-field microscope are shown with respect to the numerical aperture (NA). Resolutions are calculated with $\lambda = 510\text{nm}$, the emission maximum of GFP and $n = 1.33$, the refractive index of water, for water dipping objectives.

1 the focus, only a blur will be visible. This blur potentially degrades image quality and
 2 signal-to-noise ratio to such extent that makes imaging thick sample very difficult if not
 3 impossible in a wide-field microscope.

4 Evaluating Equations 1.10 and 1.12 for a range of possible numerical apertures reveals
 5 the significant differences in lateral and axial resolution for any objective (Fig. 1.6).
 6 Especially for low NAs, this can be significant, a factor of ~ 20 difference. For higher
 7 (>0.8) NAs the axial resolution increases faster than the lateral, however they will only
 8 be equal when $\alpha = 180^\circ$. This means that isotropic resolution with a single lens is only
 9 possible if the lens is collecting all light emitting from the sample, which seems hardly
 10 possible, and would be highly impractical. For commonly used high NA objectives the
 11 lateral to axial ratio will still be around 3–6.

12 Instead of using a single lens to achieve isotropic resolution, it is more practical
 13 to image the sample from multiple directions to complement the missing information
 14 from different views. When rotating the sample 90° for example, the lateral direction
 15 of the second view will correspond to the axial direction of the first view. If rotation
 16 is not possible, using multiple objectives can also achieve similar result, such as in the
 17 case of Multi-Imaging Axis Microscopy (MIAM) [27, 28]. This microscope consisted of 4
 18 identical objectives arranged in a tetrahedral fashion to collect as much light as possible
 19 from multiple directions, and provide isotropic 3D resolution, albeit at the expense of
 20 extremely difficult sample handling, since the sample was completely surrounded by

1. LIVE IMAGING IN THREE DIMENSIONS

1 objectives from all directions.

2 1.2.1 Confocal laser scanning microscopy

3 Confocal laser scanning microscopy (CLSM) [29, 30] addresses most of the problems
4 of wide-field microscopy we mentioned in the previous section. It is capable of optical
5 sectioning by rejecting out of focus light, which makes it a true 3D imaging technique.
6 Furthermore, the light rejection also massively reduces out of focus background, and
7 increases contrast.

8 This is achieved by two significant modifications compared to the wide-field optical
9 path. To be able to reject the out of focus light, an adjustable pinhole is placed at the focus
10 of the tube lens. Light rays originating from the focal point will meet at this position,
11 and are able to pass through the pinhole, however out-of-focus light will converge either
12 before or after the aperture, and thus the aperture blocks these rays. To maximize the
13 fluorescence readout efficiency for the single focal point, a photomultiplier tube is used
1 instead of an area sensor (Fig. 1.7a).

2 To maximize the signal from the focal point, the illumination light is also focused
3 here by coupling an expanded laser beam through the back aperture of the objective.
4 This not only increases illumination efficiency (since other, not detected points are not
5 illuminated), but has the added benefit of increasing the resolution as well. This is due to
6 the combined effect of illumination and detection PSFs as described in Eq. 1.14 (Fig. 1.8).
7 For Gaussian-like PSFs, the final resolution (along a single direction) can be calculated
8 in the following way:

$$\frac{1}{\delta_{sys}^2} = \frac{1}{\delta_{ill}^2} + \frac{1}{\delta_{det}^2}, \quad (1.15)$$

9 where δ_{ill} and δ_{det} are the resolutions for the illumination and detection, respectively.
10 Since the same objective is used for both illumination and detection, and the difference
11 in wavelength is almost negligible, $\delta_{ill} = \delta_{det} = \delta$, the final system resolution will be:

$$\delta_{sys} = \frac{1}{\sqrt{2}}\delta. \quad (1.16)$$

12 This means that the distinguishable features in a confocal microscope are ~ 0.7 times
13 smaller than in a wide-field microscope using the same objective.

14 Because of the different detection method in a confocal microscope, direct image
15 formation on an area sensor is not possible, since at any given time, only a single point is
16 interrogated in the sample. Instead, it is necessary to move the illumination and detection
17 point in synchrony (or in a simpler, albeit slower solution, to move the sample) to scan
18 the entire field of view. The image can be later computationally reconstructed by a
19 computer program that records the fluorescence intensity of every point of the field of

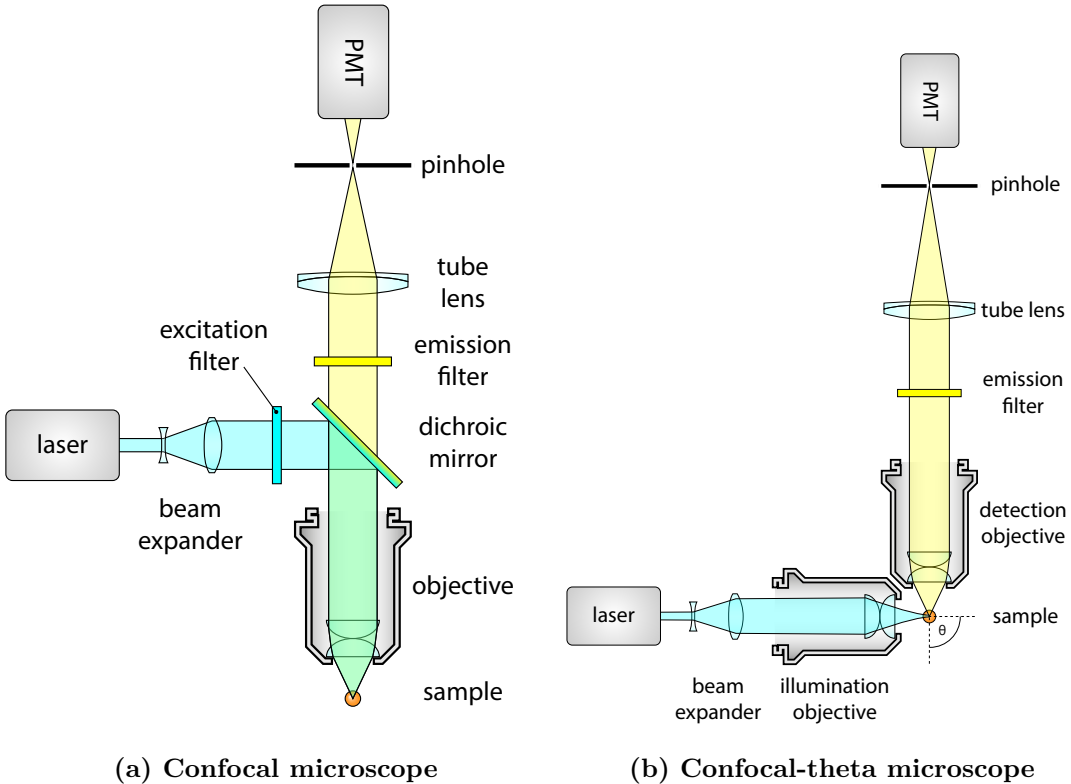


Figure 1.7: Basic optical components of a confocal laser scanning and confocal-theta microscope. Both type of microscopes use confocal images detection, which means that a pinhole is used to exclude light coming from out of focus points. Light intensity is measured by a photomultiplier for every voxel in the region of interest. The final image is generated on a computer using the positions and recorded intensity values. A regular confocal microscope (1.7a) uses the same objective for illumination and detection, while a confocal-theta microscope (1.7b) uses a second objective that is rotated by ϑ around the focus. In this case, $\vartheta = 90^\circ$.

1 view, and displays these values as a raster image.

2 1.2.2 Confocal-theta microscopy

3 Although confocal microscopy already has 3D capabilities, its axial resolution is still lim-
 4 ited compared to the lateral, since it uses only one objective. An alternative realization
 5 of the confocal microscope, the confocal theta microscope [31] introduces a second objec-
 6 tive to the system, that is used to illuminate the sample (Fig. 1.7b). Since this decouples
 7 the illumination and detection, using a filter cube is no longer necessary. The second
 8 objective is rotated by θ around the focus, this is where the name of this setup originates
 9 from.

10 As in the case of standard confocal microscopy, the system PSF is improved by the
 11 illumination pattern. Here, however, the axial direction of the detection coincides with
 12 the lateral direction of the illumination, which results in a dramatic improvement of
 13 axial resolution compared to standard confocal microscopy. Lateral resolution will also

1. LIVE IMAGING IN THREE DIMENSIONS

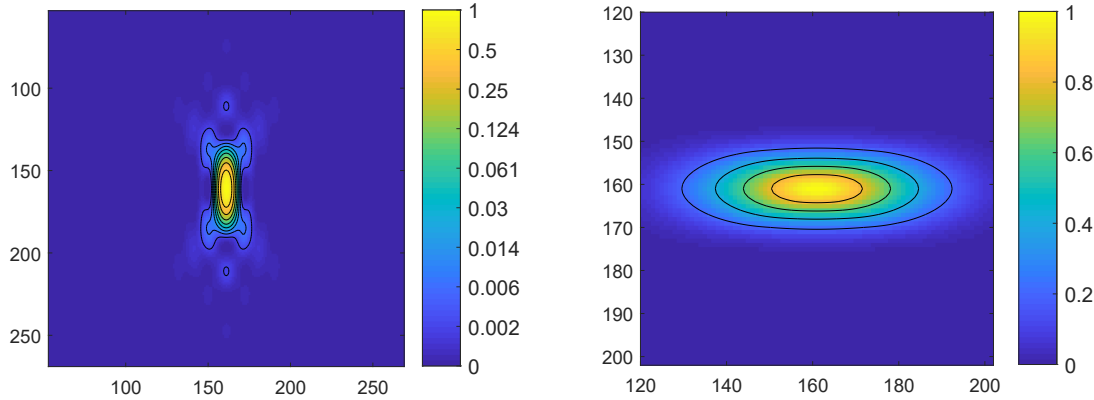


Figure 1.8: Axial cross section of the PSF and OTF of a confocal laser scanning microscope. Simulated PSF and OTF for a laser scanning confocal microscope with a water immersion objective ($n = 1.33$). $NA = 1.1$, $\lambda = 510\text{ nm}$

14 be increased, but by a smaller extent, resulting in an almost isotropic PSF, and equal
15 axial and lateral resolutions (Fig. ??).

16 Although this is a big improvement to confocal microscopy in terms of resolution,
17 this technique did not reach a widespread adoption as it complicates sample handling,
18 while still suffering from two big drawbacks of confocal microscopy techniques that limits
19 its live imaging capabilities.

20 Imaging live specimens for an extended period of time with confocal microscopy
21 although possible [32, 33], is not ideal. For each voxel imaged, a large portion of the
22 specimen has to be illuminated, which results in a very high dose of radiation on the
23 samples. This can be as much as 30–100 times larger, than the dose used for the actual
24 imaging [34]. Illumination with high power of laser for an extended time frame can
25 result in bleaching the fluorophores, which in turn will lower the signal at later times.
26 Furthermore, any absorbed photon has the possibility to disrupt the chemical bonds
27 inside the specimen, which can lead to phototoxic effects. Moreover, the usage of the
28 pinhole although increases resolution, also decreases the detectable signal intensity, thus
29 has a negative impact on image contrast [35].

30 1.3 Light-sheet microscopy

31 A selective-plane illumination microscope (SPIM) uses a light-sheet to illuminate only
32 a thin section of the sample (Fig. 1.9). This illumination plane is perpendicular to the
33 imaging axis of the detection objective and coincides with the focal plane. This way, only
34 the section in focus will be illuminated, thus providing much better signal to noise ratio.
35 In case of conventional wide-field fluorescence microscopy, where the whole specimen

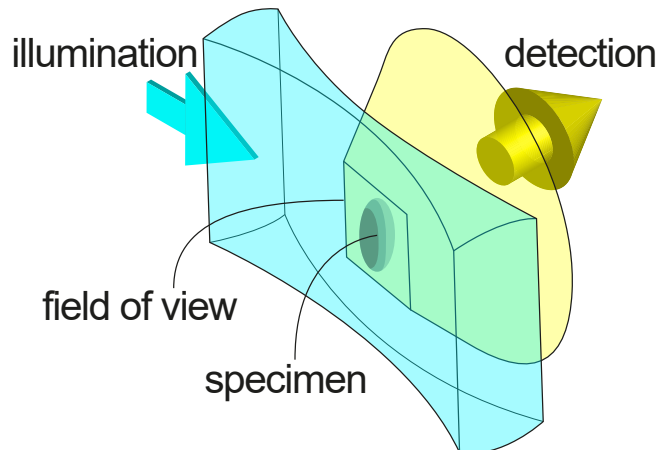


Figure 1.9: Basic concept of single-plane illumination microscopy. The sample is illuminated from the side by laser light shaped to a light-sheet (blue). This illuminates the focal plane of the detection lens, that collects light in a wide-field mode (yellow). The image is recorded, and the sample is translated through the light-sheet to acquire an entire 3D stack.

36 is illuminated, out of focus light contributes to a significant background noise. With
 1 selective-plane illumination, this problem is intrinsically solved, and it also provides a
 2 true sectioning capability. This makes SPIM especially suitable for 3D imaging.

3 The main principle behind single plane illumination microscopy, that is illuminat-
 4 ing the sample from the side by a very thin light-sheet, dates back to the early 20th
 5 century, when Siedentopf and Zsigmondy first described the ultramicroscope [36]. This
 6 microscope used sunlight as an illumination source, that was guided through a precision
 7 slit to generate a thin light-sheet. This allowed Zsigmondy to visualize gold nanoparti-
 8 cles floating in and out of the light-sheet. Since these particles are much smaller than
 9 the wavelength of the light, the device was called an ultramicroscope. His studies with
 10 colloids, and the development of the ultramicroscope led Zsigmondy to win the Nobel
 11 Prize in 1925.

12 After Zsigmondy, this method was forgotten until rediscovered in the 1990s, when
 13 Voie *et al.* constructed their Orthogonal-plane Fluorescent Optical Sectioning (OPFOS)
 14 microscope [37]. They used it to image a fixed, optically cleared and fluorescently labelled
 15 guinea pig cochlea. In order to acquire a 3D dataset, the sample was illuminated from the
 16 side with a light-sheet generated by a cylindrical lens, then rotated around the center axis
 17 to obtain multiple views. Although they only reached a lateral resolution around 10 µm
 18 and axial resolution of 26 µm, this method allowed them to generate a 3D reconstruction
 19 of the guinea pig cochlea [38].

20 Later, in 2002, Fuchs *et al.* developed Thin Light-Sheet Microscopy (TLSM) [39]
 21 and used this technique to investigate the microbial life in seawater samples without
 22 disturbing their natural environment (by e.g. placing them on a coverslip). Their light-
 23 sheet was similar to the one utilized in OPFOS, being 23 µm thin, and providing a

1. LIVE IMAGING IN THREE DIMENSIONS

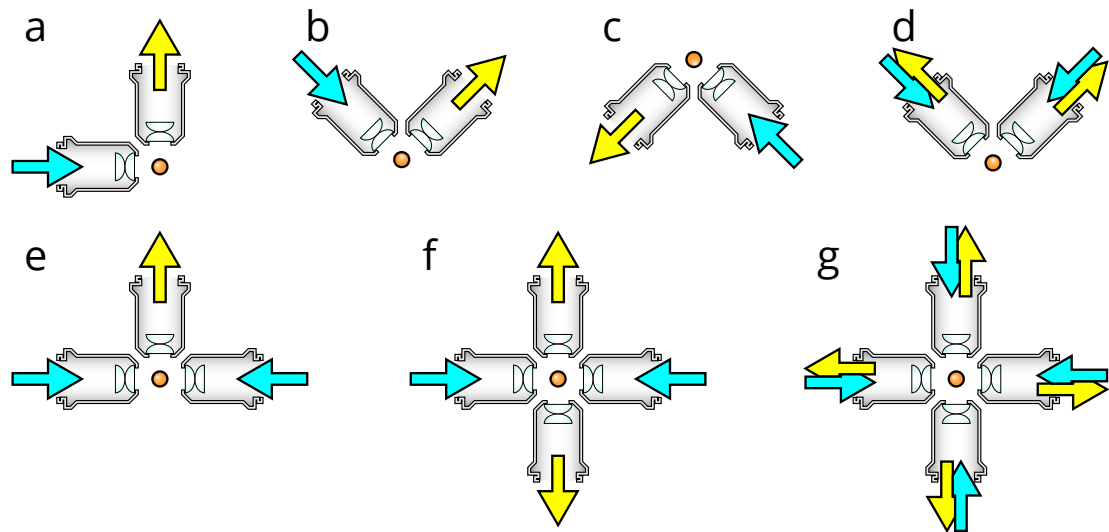


Figure 1.10: Different optical arrangements for light-sheet microscopy. (a) Original SPIM design with a single lens for detection and illumination. [40] (b) Upright SPIM to allow for easier sample mounting such as using a petri dish (iSPIM, [41, 42, J1]). (c) Inverted SPIM, where the objectives are below the sample, which is held by a thin foil [J2]. (d) Dual-view version of the upright configuration, where both objective can be used for illumination and detection (disPIM, [43]). (e) Multidirectional-SPIM (mSPIM) for even illumination of the sample with two objectives for illumination [44]. (f) Multi-view SPIM with two illumination and detection objectives for *in toto* imaging of whole embryos (MuVi-SPIM [45], SimView [46], Four-lens SPIM [47]). (g) A combination of (d) and (f), using four identical objectives, where both can illuminate and detect in a sequential manner, to achieve isotropic resolution without sample rotation (IsoView [48]).

²⁴ 1 mm × 1 mm field of view.

¹ Despite these early efforts, the method did not gain larger momentum. The real
² breakthrough in light-sheet imaging happened at the European Molecular Biology Labo-
³ ratory (EMBL) in 2004, where Huisken *et al.* [40] combined the advantages of endogenous
⁴ fluorescent proteins and the optical sectioning capability of light-sheet illumination to
⁵ image Medaka fish embryos, and the complete embryonic development of a *Drosophila*
⁶ *melanogaster* embryo. They called this Selective-Plane Illumination Microscopy (SPIM),
⁷ and it quickly became popular to investigate developmental biological questions.

⁸ Since then, light-sheet based imaging has gained more and more popularity, as it can
⁹ be adapted and applied to a wide variety of problems. Although sample mounting can
¹⁰ be challenging because of the objective arrangement, this can also be an advantage, since
¹¹ new microscopes can be designed with the sample in mind [4, J3] (Fig. 1.10). This made
¹² it possible to adapt the technique for numerous other specimens, such as zebrafish larvae
¹³ [49], *C. elegans* embryos [42], mouse brain [7], and even mouse embryos [J2, 50, 51].

¹⁴ As many of these specimens require very different conditions and mounting tech-
¹⁵ niques, these microscopes have been adapted to best accommodate them. An upright
¹⁶ objective arrangement for example (Fig 1.10b) allows imaging samples on a coverslip,
¹⁷ while its inverted version is well suited for mouse embryos, where a foil is separating them

from the immersion medium (Fig. 1.10c). A modified version of the upright arrangement allows for multi-view imaging using both objectives for illumination and detection in a sequential manner (Fig. 1.10d) [52].

For larger samples, to achieve a more even illumination, two objectives can be used from opposing directions to generate two light-sheets (Fig. 1.10e) [44]. This arrangement can further be complemented by a second detection objective, to achieve parallelized multi-view imaging (Fig. 1.10f) [45–47]. For ultimate speed, 4 identical objectives can be used to achieve almost instantaneous views from 4 different directions by using all objectives for illumination and detection (Fig. 1.10g) [48].

Furthermore, because of the wide-field detection scheme it is possible to combine SPIM with many superresolution techniques, such as single molecule localization [53], STED [54], RESOLFT [J1], or structured illumination [8, 55, 56].

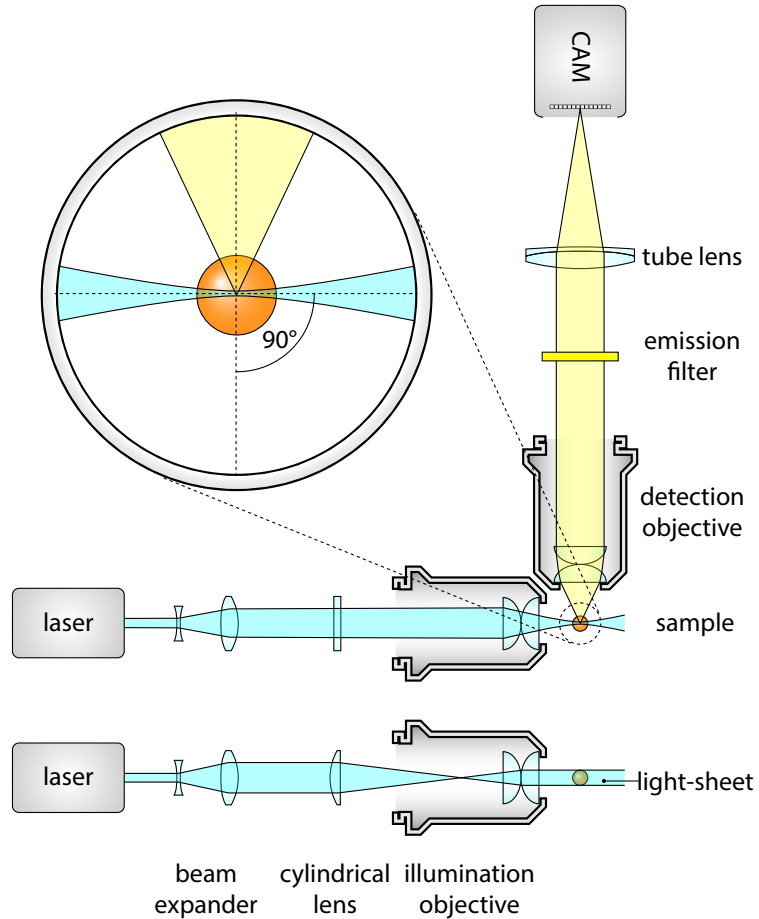


Figure 1.11: Basic optical components of a SPIM. A dedicated illumination objective is used to generate the light sheet, which is an astigmatic Gaussian beam, focuses along one direction. Astigmatism is introduced by placing a cylindrical lens focusing on the back focal plane of the objective. Detection is performed at a right angle, with a second, detection objective. Scattered laser light is filtered, and a tube lens forms the image on an area sensor, such as an sCMOS camera.

1. LIVE IMAGING IN THREE DIMENSIONS

11 Since illumination and detection for light-sheet microscopy are decoupled, two inde-
1 dependent optical paths are implemented.

2 The detection unit of a SPIM is basically equivalent to a detection unit of a wide-field
3 microscope, without a dichroic mirror (Fig. 1.11). The most important components are
4 the objective together with the tube lens, filter wheel, and a sensor, typically a CCD or
5 sCMOS camera.

6 One of the most important aspects that determines the resolution of the microscope
7 is the detection objective. Since imaging biological specimens usually requires a water-
8 based solution, the objectives also need to be directly submerged in the medium to
9 minimize spherical aberrations. Since the refraction index of water ($n = 1.33$) is greater
10 than the refraction index of air, these objectives tend to have a higher NA, which results
11 in higher resolution. The final resolution, however, also depends on the pixel size of the
12 sensor which determines the spatial sampling rate of the image.

13 Although image quality and resolution greatly depends on the detection optics, the
14 real strength of light-sheet microscopy, the inherent optical sectioning is due to the
15 specially designed illumination pattern, that confines light to the vicinity of the detection
16 focal plane.

17 There are two most commonly used options to generate a light-sheet: either by using
18 a cylindrical lens, to illuminate the whole field of view with a static light-sheet, as in the
19 original SPIM concept [40]; or by quickly scanning a thin laser beam through the focal
20 plane, thus resulting in a virtual light-sheet [49].

21 1.3.1 Static light-sheet illumination

22 For a static light-sheet, the normally circular Gaussian laser beam needs to be shaped
23 in an astigmatic manner, i.e. either expanded or squeezed along one direction, to shape
24 it into a sheet instead of a beam. This effect can be achieved by using a cylindrical lens,
25 which as the name suggests has a curvature in one direction, but is flat in the other, thus
26 focusing a circular beam to a sheet (Figure 1.11).

27 However, to achieve light-sheets that are thin enough, one would need to use cylindri-
28 cal lens with a very short focal length, and these are hardly accessible in well corrected
29 formats. For this reason, it is more common to use a longer focal length cylindrical lens
30 in conjunction with a microscope objective, which is well corrected for chromatic and
31 spherical aberrations [57]. This way, the light-sheet length, thickness and width can be
32 adjusted for the specific imaging tasks.

33 Light-sheet dimensions

34 The shape of the illumination light determines the optical sectioning capability and the
35 field of view of the microscope, so it is important to be able to quantify these measures.



Figure 1.12: Light-sheet dimensions. 1.12a The width and thickness of the field of view depends on the Rayleigh length of the beam ($z_{R,y}$) and the beam waist (W_0). 1.12b Height of the field of view is determined by the Gaussian profile of the astigmatic beam. 1.12c shows a light sheet, with the field of view indicated. Since the light-sheet intensity is uneven, the field of view has to be confined to a smaller region.

- 1 The most commonly used illumination source is a laser beam coupled to a single mode
- 2 fiber, thus its properties can be described by Gaussian beam optics.
- 3 For paraxial waves, i.e. waves with nearly parallel wave front normals, a general wave
- 4 equation can be approximated with the paraxial Helmholtz equation [58]

$$\nabla_T^2 U + i2k \frac{\partial U}{\partial z} = 0 \quad (1.17)$$

- 5 where $\nabla_T^2 = \frac{\partial^2}{\partial x^2} + \frac{\partial^2}{\partial y^2}$, $U(\vec{r})$ is the wave function, $k = \frac{2\pi}{\lambda}$ is the wavenumber and z is in
- 6 the direction of the light propagation.

7 A simple solution to this differential equation is the Gaussian beam:

$$U(r, z) = A_0 \cdot \frac{W_0}{W(z)} \cdot e^{-\frac{r^2}{W^2(z)}} \cdot e^{-i \cdot \phi(r, z)} \quad (1.18)$$

- 8 where A_0 is the amplitude of the wave, W_0 is the radius of the beam waist (the thinnest
- 9 location on the beam), $r = \sqrt{x^2 + y^2}$ is the distance from the center of the beam, $W(z)$
- 10 is the radius of the beam z distance from the waist, and $\phi(r, z)$ is the combined phase
- 11 part of the wave-function (Fig. 1.12a). Furthermore:

$$W(z) = W_0 \sqrt{1 + \left(\frac{z}{z_R} \right)^2} \quad (1.19)$$

- 12 where the parameter z_R is called the Rayleigh-range, and is defined the following way:

$$z_R = \frac{\pi W_0^2}{\lambda}. \quad (1.20)$$

- 1 Apart from the circular Gaussian beam, the elliptical Gaussian beam is also an eigen-
- 2 function of Helmholtz equation (1.17) which describes the beam shape after a cylindrical

1. LIVE IMAGING IN THREE DIMENSIONS

³ lens:

$$U(x, y, z) = A_0 \cdot \sqrt{\frac{W_{0,x}}{W_x(z - z_{0,x})}} \sqrt{\frac{W_{0,y}}{W_y(z - z_{0,y})}} \cdot e^{-\frac{x^2}{W_x^2(z - z_{0,x})}} \cdot e^{-\frac{y^2}{W_y^2(z - z_{0,y})}} \cdot e^{-i \cdot \phi(x, y, z)} \quad (1.21)$$

This beam still has a Gaussian profile along the x and y axes, but the radii ($W_{0,x}$ and $W_{0,y}$), and the beam waist positions ($z_{0,x}$ and $z_{0,y}$) are uncoupled, which results in an elliptical and astigmatic beam. The beam width can be now described by two independent equations for the two orthogonal directions:

$$W_x(z) = W_{0,x} \sqrt{1 + \left(\frac{z}{z_{R,x}}\right)^2} \quad \text{and} \quad W_y(z) = W_{0,y} \sqrt{1 + \left(\frac{z}{z_{R,y}}\right)^2}. \quad (1.22)$$

Since the beam waist is different along the two axes, the Rayleigh range is also different:

$$z_{R,x} = \frac{\pi W_{x,0}^2}{\lambda}, \quad z_{R,y} = \frac{\pi W_{y,0}^2}{\lambda}. \quad (1.23)$$

⁴ Based on these equations, the light-sheet dimensions and usable field of view can be
⁵ specified (Fig. 1.12c). The light-sheet thickness will depend on the beam waist, $W_{0,y}$ (if
⁶ we assume the cylindrical lens is focusing along y), and the length of the light-sheet can
⁷ be defined as twice the Rayleigh range, $2 \cdot z_{R,y}$. As these are coupled (see Eq. 1.23), having
⁸ a thin light-sheet for better sectioning also means the length of it will be relatively short.
⁹ Fortunately, because of the quadratic relation, to increase the field of view by a factor
¹⁰ of two, the light-sheet thickness only needs to increase by a factor of $\sqrt{2}$.

¹¹ Light-sheet height is determined by the intensity profile of the beam along the vertical
¹² axis (Fig. 1.12b). Since this is a Gaussian function (see Eq. 1.18), only a small part in
¹³ the middle can be used for imaging, because towards the sides the intensity dramatically
¹⁴ drops. To allow a maximum 20% drop of intensity at the edges, the light-sheet height is
¹⁵ $h_{fov} = 2 \cdot 0.472 \cdot W_{x,0}$.

1.3.2 Digitally scanned light-sheet illumination

¹⁷ Although generating a static light-sheet is relatively straightforward, with the simple
¹⁸ addition of a cylindrical lens to the light path, it has some drawbacks. As already men-
¹⁹ tioned in the previous section, the light intensity distribution along the field of view is
²⁰ not constant, as the light-sheet is shaped from a Gaussian beam. Furthermore, along
²¹ the lateral direction of the light-sheet the illumination NA is extremely low, resulting
²² in effectively collimated light. Because of this, shadowing artifacts can deteriorate the
¹ image quality [44].

² A more flexible way of creating a light-sheet is by scanning a focused beam in the fo-

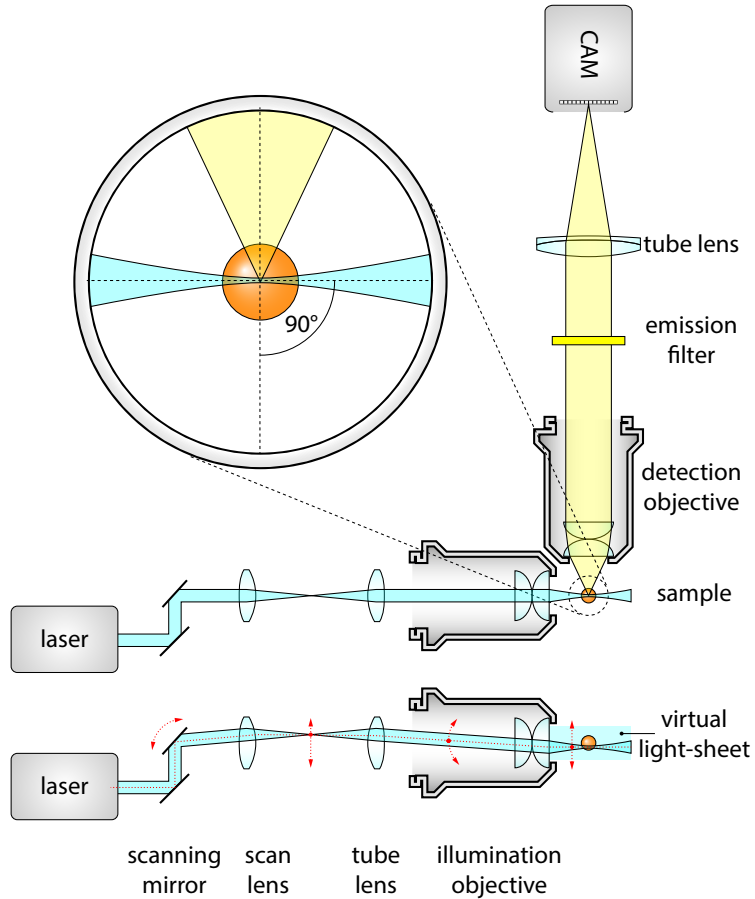


Figure 1.13: DSLM illumination. DSLM illuminates a specimen by a circularly-symmetric beam that is scanned over the field of view. This creates a virtual light-sheet, which illuminates a section of a specimen just like the SPIM. Light-sheet in DSLM is uniform over the whole field of view and its height can be dynamically altered by changing the beam scan range.

3 cal plane to generate a virtual light-sheet (digital scanned light-sheet microscopy, DSLM
 4 [49]). Although this method might require higher peak intensities, it solves both draw-
 5 backs of the cylindrical lens illumination. By scanning the beam, the light-sheet height
 6 can be freely chosen, and a homogenous illumination will be provided. Focusing the
 7 beam in all directions evenly introduces more angles in the lateral direction as well,
 8 which shortens the length of the shadows.

9 The basic optical layout of a DSLM is shown on Fig. 1.13. A galvanometer controlled
 10 mirror is used to alter the beam path that can quickly turn around its axis which will
 11 result in an angular sweep of the laser beam. To change the angular movement to trans-
 12 lation, a scan lens is used to generate an intermediate scanning plane. This plane is then
 13 imaged to the specimen by the tube lens and the illumination objective, resulting in a
 1 scanned focused beam at the detection focal plane. The detection unit is identical to the
 2 wide-field detection scheme, similarly to the static light-sheet illumination. By scanning

1. LIVE IMAGING IN THREE DIMENSIONS

3 the beam at a high frequency, a virtual light-sheet is generated, and the fluorescence
4 signal is captured by a single exposure on the camera, resulting in an evenly illuminated
5 field of view.

6 1.4 Light-sheet microscopy for mouse imaging

7 Because of its optical sectioning capabilities, combined with the high specificity of flu-
8 orescent labels, confocal microscopy had an immense influence on biological research,
9 and has been the go-to technique for decades for many discoveries [59–61]. Live imaging
10 capabilities of confocal microscopy are, however, limited. This is mostly due to the illu-
11 mination scheme: to collect information from a single point, almost the whole embryo
12 has to be illuminated. This unwanted illumination can easily lead to bleaching of the
13 fluorophores, and also to phototoxic effects that can prevent further embryonic develop-
14 ment. The point scanning nature of image acquisition also implies an inherent constraint
15 to the maximum imaging speed, as it can be only increased at the expense of reducing
16 signal intensity (Fig. 1.1).

17 One improvement to address both of these drawbacks is the use of a spinning disk with
18 a specific pattern (also called Nipkow disk) of holes to generate multiple confocal spots
19 at the same time [60]. If these spots are far enough from each other, confocal rejection
20 of out-of-focus light can still occur. As the disk is spinning, the hole pattern will sweep
21 the entire field of view, eventually covering all points [62]. The image is recorded by an
22 area detector, such as a CCD or EM-CCD, which speeds up image acquisition [63].

23 Although out-of-focus illumination is still an issue, spinning disk confocal microscopy
24 was successfully used to investigate the mechanisms of symmetry breaking in early mouse
25 embryonic development [64], and the mechanisms leading to the first cell fate specification
26 that will differentiate extraembryonic tissue from the embryo proper [33, 65, 66]. Even
27 though these studies were carried out with live embryos, only a few hours of continuous
28 imaging is possible before the accumulation of phototoxic effects arrests development
29 [67]. Compared to this, just the pre-implantation phase of mouse embryonic development
30 spans 3 days, and the full development is 18 days [68].

31 1.4.1 Imaging pre-implantation

32 Pre-implantation is the first phase of mouse embryonic development, that starts right
33 after fertilization. The embryo in this phase is still in the oviduct, travelling towards
34 the uterus, where it will implant to the uterine wall. The developmental stage between
35 fertilization and the implantation is called the pre-implantation stage. Here the embryo
1 divides, and already the first cell fate specifications start when forming the trophecto-
2 derm (TE) and the inner cell mass (ICM) at the blastocyst stage. ICM cells will form

1.4 Light-sheet microscopy for mouse imaging

3 the embryo proper, while TE cell will contribute to the formation of the extraembryonic
4 tissues.

5 During this process the embryo is still self-sufficient, which makes it possible to image
6 this stage in an *ex vivo* embryo culture by providing the proper conditions [69]. Long
7 term imaging, however, is extremely challenging due to the very high light sensitivity of
8 the specimens. Imaging these embryos in a confocal microscope will lead to incomplete
9 development, even if the imaging frequency is minimized to every 15 mins [J2].

10 Imaging for just a few hours is already enough to investigate important processes, such
11 as cell fate patterning [70]. Other approaches aim to lower the phototoxicity by either
12 using 2-photon illumination which operates at longer wavelengths [71–73], or by lowering
13 imaging frequency as a compromise [74]. These approaches, however either require highly
14 specialized equipment, such as an ultra short pulsed laser, or is compromising on the time
15 resolution.

16 Light-sheet microscopy, on the other hand, drastically lowers phototoxic effect by
17 using a much more efficient illumination scheme (see Sec. 1.3), and thus makes a better
18 use of the photon budget. Using this technique, it is possible to image the full pre-
19 implantation development at high spatial and temporal resolution without any negative
20 impact on the developmental process. Such a microscope was developed by Strnad *et al.*
21 at EMBL [J2], who used it to understand when exactly is the first cell fate specification
22 decided in the embryonic cells.

23 As a mouse embryo culture is not compatible with the standard agarose-based sample
24 mounting techniques, a completely new approach was taken, which resulted in a micro-
25 scope designed around the sample. The sample holder forming a V-shape was built with
26 a bottom window, and it is lined with a thin FEP (fluorinated ethylene propylene) foil
27 that supports the embryos (Fig. 1.14A, i). This arrangement allows the utilization of
28 the standard microdrop embryo culture, while providing proper viewing access for the
29 objectives. As the embryos are relatively small (100 μm) and transparent, a single illu-
30 mination and single detection objective arrangement is enough for high quality imaging.
31 A low resolution ($\text{NA}=0.3$) objective is used to generate the scanned light-sheet, and
32 a high resolution ($\text{NA}=1.1$) objective is detecting the fluorescence at $50\times$ magnification
33 (Fig 1.14A, ii). As the foil is curved, it allows unrestricted access to the embryo, while
34 separating the imaging medium from the immersion liquid (Fig. 1.14A, iii). Furthermore,
35 its refractive index is matching the refractive index of water, so optical aberrations are
36 minimized.

37 Using this setup, Strnad *et al.* were able to pinpoint the exact timing of the first cell
38 fate decision that leads either to ICM or TE cells. More than 100 embryos expressing
1 nuclear (H2B-mCherry) and membrane (mG) markers were imaged for the entire 3 days
2 of pre-implantation development (Fig. 1.14B). The image quality was good enough to

1. LIVE IMAGING IN THREE DIMENSIONS

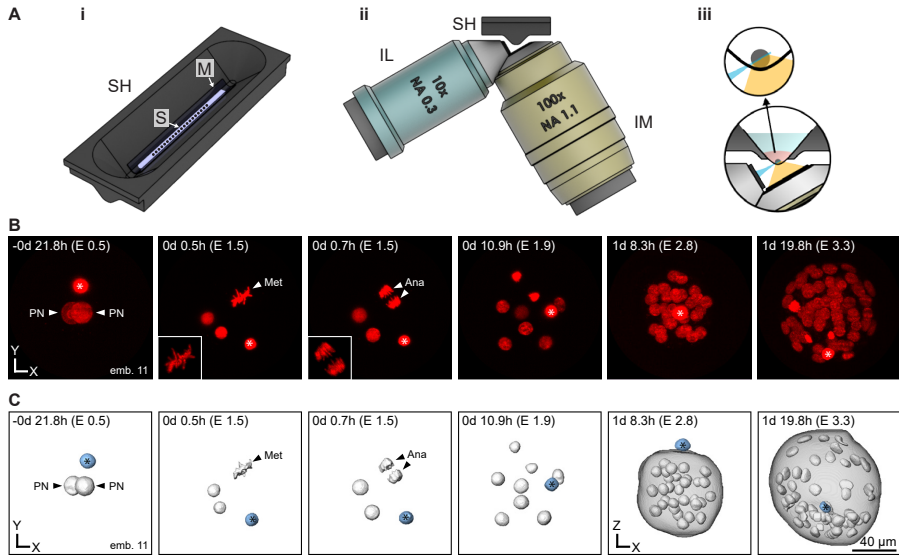


Figure 1.14: Inverted light-sheet microscope for multiple early mouse embryo imaging.. (i) A sample holder (SH), containing a transparent FEP membrane (M) allows multiple embryo samples (S) to be placed in line for multisample imaging. (ii) Inverted objective orientation with side view of the sample holder. One possible configuration is to use a 10×0.3 NA illumination objective (IL) and another 100×1.1 NA detection objective placed at a right angle to the illumination. (iii) Close up on side view of sample on FEP membrane with both objectives. Since the FEP membrane is transparent on water, it provides no hindrance to the illumination beam in penetrating the sample or for the emitted fluorescence on reaching the detection objective. (B) Still images of one particular timelapse experiment, and (C) corresponding segmented nuclei. The star depicts the polar body. Adapted from Strnad *et al.* [J2]

3 segment all nuclei in the embryos (Fig. 1.14C), and track them from 1 to 64 cell stage,
4 building the complete lineage tree. Based on the lineage trees, and the final cell fate
5 assignments, it was determined that at the 16 cell stage the final specification is already
6 decided, while earlier than this it is still random.

7 1.4.2 Imaging post-implantation development

8 After the initial 3 days of pre-implantation, the embryo undergoes the implantation
9 process, during which it is inaccessible to microscopical investigations. Although a new
10 method was recently developed that allows *in vitro* culturing of the embryos embedded
11 in a 3D gel [76], this has not reached wider adoption yet. Because of this, developmental
12 processes during implantation have only been investigated in fixed embryos.

13 Following the implantation process, at the post-implantation phase, *ex vivo* embryo
14 culturing becomes possible again [77, 78], and these embryos can be kept alive for several
15 days in an artificial environment. During this process especially interesting stages are the
16 late blastocyst (\sim E4.5), gastrulation (\sim E6.5), and somite formation (\sim E8.5). Before live
17 imaging techniques became available, these stages were mostly investigated using *in situ*
18 visualization techniques to shed light on several developmental processes [79]. Many
1 pathways playing important roles have been identified this way, however live imaging is
2 still necessary to validate these results, and ensure continuity in the same specimen [80].

1.4 Light-sheet microscopy for mouse imaging

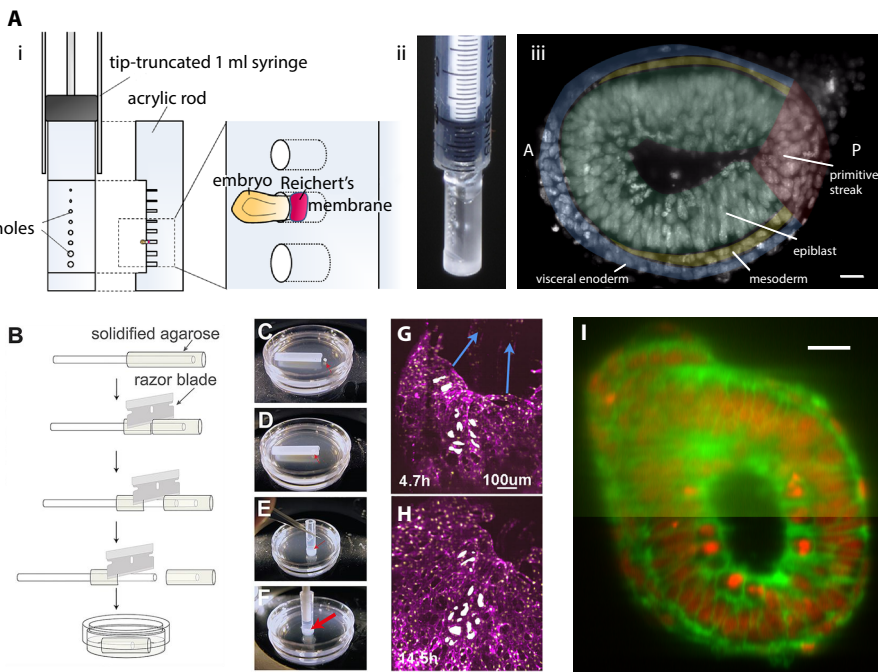


Figure 1.15: Imaging mouse post-implantation development. (A) (i, ii) Mounting technique for E5.5 to E6.5 embryos. A tip-truncated 1 mL syringe holds an acrylic rod, cut and drilled with holes of different size in order to best fit the mouse embryo by its Reichert's membrane, leaving the embryo free inside the medium. (iii) Maximum intensity projection of a 13 μm slice at 78 μm from distal end of an E6.5 mouse embryo. The different tissues corresponding to the rudimentary body plan are annotated. Scale bar: 20 μm . (B) For stages ranging between E6.5 and E8.5, mounting using a hollow agarose cylinder has also successfully been proposed. Optimal sizes for the corresponding embryonic stage to be imaged can be produced, so that the embryo can grow with least hindrance. (C–F) Steps for mounting the mouse embryo inside the agarose cylinder. The inner volume of the cylinder can be filled with optimal medium, allowing the much larger chamber volume to have less expensive medium. (G–H) Example images of a 9.8 h timelapse with the mounting shown in (B) where the expansion of the yolk sac can be observed in direction of the blue arrows. (I) In order to aid multiview light-sheet setups in overcoming the higher scattering properties of embryos at this stage, and to allow faster and easier data recording, electronic confocal slit detection allows better quality images to be taken at shorter acquisition times. Scale bar: 20 μm . Adapted from Ichikawa *et al.* [50], Udan *et al.* [51] and de Medeiros and Norlin *et al.* [75].

3 Light-sheet microscopy is a good choice for imaging these stages, just like in the case
 4 of pre-implantation embryos. These embryos, however, present new challenges for sample
 5 handling and culturing. Owing to their extreme sensitivity, dissection can be difficult,
 6 especially for earlier stages (E4.5). Furthermore, since the embryo is also growing during
 7 development, gel embedding is not an option, as this might constrain proper development.
 8 Thus, special handling and mounting techniques had to be developed in order to allow
 9 live 3D imaging of these specimens.

10 Ichikawa *et al.* [50] designed a custom mounting apparatus manufactured from acrylic
 11 in the shape of a rod that fits in a standard 1 mL syringe with its tip truncated (Fig.
 12 1.15A, i). In the rod several holes were drilled with different sizes that can accommo-
 13 date different sized embryos, which are held by an extraembryonic tissue, the Reichert's
 1 membrane (Fig. 1.15A, ii). Mounting this way doesn't disturb the embryo itself, and it
 2 can freely develop in the culturing medium, while it is also stationary for the purpose of

1. LIVE IMAGING IN THREE DIMENSIONS

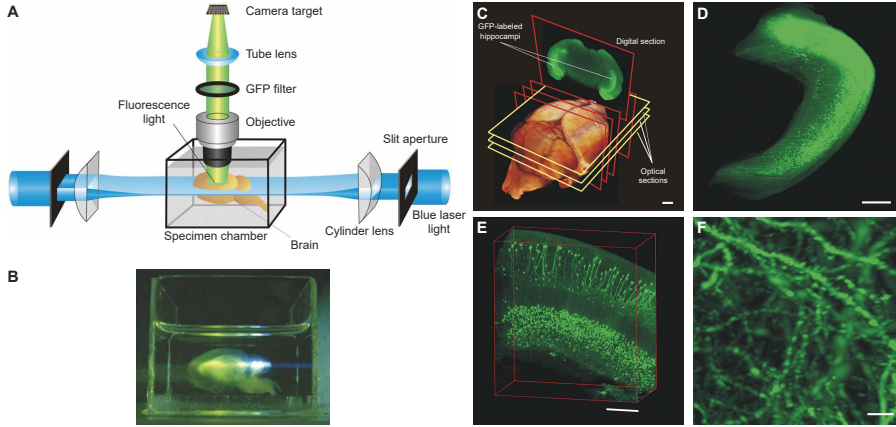


Figure 1.16: Imaging adult mouse brain with light-sheet microscopy. (A) Schematics of the ultramicroscope for brain imaging. The specimen is embedded in clearing medium to ensure necessary imaging depth. Illumination is applied from two sides to achieve even illumination for the whole field of view. Light-sheet is generated by a slit aperture flowed by a cylindrical lens. The specimen is imaged from the top using wide-field detection method. (B) Photograph of the imaging chamber with a mounted cleared specimen and light-sheet illumination. (C) Surface rendering of a whole mouse brain, reconstructed from 550 optical sections. GFP and autofluorescence signal was imaged. Hippocampal pyramidal and granule cell layers are visible in the digital section. Scale bar: 1 mm. Objective: Planapoachromat 0.5×. (D) Reconstruction of an excised hippocampus from 410 sections. Note that single cell bodies are visible. Scale bar: 500 µm. Objective: Fluar 2.5×. (E) 3D reconstruction of a smaller region of an excised hippocampus from 132 sections. Scale bar: 200 µm. Objective: Fluar 5×. (F) 3D reconstruction of CA1 pyramidal cells imaged with a higher resolution objective (LD-Plan Neofluar 20× NA 0.4) in a whole hippocampus (430 sections). Dendritic spines are also visible, even though usually a higher NA objective (>1.2) is required to visualize these. Scale bar: 5 µm. Adapted from Dodt *et al.* [7].

3 imaging. Using this technique, Ichikawa *et al.* were able to image through several stages
4 of development, including interkinetic nuclear migration at stages E5.5–6.5 (Fig. 1.15A,
5 iii).

6 A second method of sample mounting for light-sheet imaging was developed by
7 Udan *et al.* who were able to record a full 24 h time-lapse of living embryos focusing
8 on the gastrulation and yolk sac formation processes (Fig. 1.15G–I). Their mounting
9 technique comprised of producing a hollow agarose container shaped like a cylinder that
10 could support the embryo from below without constraining its growth (Fig. 1.15B–F).

11 Another consideration to keep in mind, is the growing size of the embryo. As it gets
12 bigger, illumination is less efficient, and scattering can dominate at larger depths. As
13 mentioned in earlier (Sec. 1.3) this can be alleviated by multi-view imaging: illuminating
14 and detecting from multiple directions. Electronic confocal slit detection can further
15 improve the signal to noise ratio by rejecting unwanted scattered light, which allows
16 deeper imaging in large specimens, even up to E7.5 (Fig. 1.15I) [75].

17 1.4.3 Imaging adult mice

18 Imaging adult mice is especially interesting for answering neurobiological questions. Since
1 development is over at this stage, the use of an environmental chamber is no longer neces-
2 sary. The biggest challenge for imaging these samples is their size, as they are centimeters

1.4 Light-sheet microscopy for mouse imaging

3 in size instead of less than a millimeter in the embryonic stage. Furthermore, the tissues
4 of adult mice are much more opaque which severely limits imaging depth. Light-sheet
5 microscopy can already deal with large specimens, however to achieve (sub)cellular res-
6 olution for an entire brain for example, multiple recording have to be stitched together
7 after acquisition [81].

8 Light scattering and absorption depends on the tissue composition, and also imaging
9 depth. Especially the brain with the high concentration of lipids in the myelinated fibers
10 pose a real challenge for imaging. Live imaging is usually performed with 2-photon mi-
11 croscopy which can penetrate the tissue up to 800 µm [82]. Using fixed samples, however,
12 the scattering problem can be eliminated by the use of tissue clearing methods.

13 Tissue clearing is a process that removes and/or substitutes scattering and absorbing
14 molecules by a chemical process while keeping the tissue structure intact and preserving
15 fluorescence. The most dominant contributors to these effects are the proteins and lipids.
16 Proteins in the cells locally change the refractive index of the tissue which leads to
17 scattering, while lipids absorb the light. Clearing methods tackle these problems by
18 chemically removing and substituting lipids by certain types of gel, and immersing the
19 whole sample in a medium with higher refractive index to match the optical properties
20 of proteins. Numerous methods have been developed for tissue clearing, such as ScaleA2
21 [83], 3DISCO [84, 85], ClearT2 [86], SeeDB [87], CLARITY [88, 89], CUBIC [90] and
22 iDISCO [91].

23 The first combination of optical clearing and light-sheet microscopy for whole brain
24 imaging was performed by Dodt *et al.* using a custom ultramicroscope consisting of two
25 opposing illumination arms and a single detection with an objective from above (Fig.
26 1.16A). The light-sheets were positioned horizontally, and the cleared samples could be
27 placed in a transparent imaging chamber filled with the clearing medium (Fig. 1.16B).
28 Imaging was performed from both top and bottom after rotating the sample 180°. By
29 changing the detection lens, it is possible to adapt the system to different samples:
30 low magnification is capable of imaging the whole brain (Fig. 1.16C), while for smaller,
31 dissected parts, such as the hippocampus, higher magnification with higher resolution is
32 more appropriate (Fig. 1.16D). With this configuration individual cell-cell contacts can
33 be recognized (Fig. 1.16E), and even dendritic spines can be visualized (Fig. 1.16F).

34 Although light-sheet microscopy is highly suitable for imaging cleared specimens, even
35 entire mice [92], brain imaging in live animals is more challenging due to the standard
36 two-objective setup of a conventional SPIM microscope. Two light-sheet based methods,
37 however offer a solution for this, axial plane optical microscopy (APOM) [93] and swept
38 confocally-aligned planar excitation (SCAPE) [94] both use only a single objective to
1 generate a light-sheet and detect the fluorescence as well. This is done by rotating the
2 detection plane at an intermediate image (APOM), or by rotating both the light-sheet

1. LIVE IMAGING IN THREE DIMENSIONS

³ and detection plane simultaneously (SCAPE).

⁴ **Chapter 2**

⁵ **Dual Mouse-SPIM**

⁶ As we have seen in the previous chapter, live imaging of mouse embryonic development is
⁷ an especially challenging task, but light-sheet microscopy can offer a good solution owing
⁸ to its gentle optical sectioning and fast image acquisition. The Mouse-SPIM introduced
⁹ in the previous chapter also solves the issue of live imaging with its inverted design: the
¹⁰ embryos are held by a foil that not only allows easy sample handling, but also acts as a
¹¹ barrier and isolates the embryos from the immersion medium.

¹² As all microscopes, the Mouse-SPIM also had to make a compromise: although its
¹³ design allows long term live imaging, it only has a single detection view, as rotation is
¹⁴ not possible with the sample mounting trays. Due to this configuration, its resolution is
¹⁵ inherently anisotropic, having an axial to lateral resolution ratio of around 3. Although
¹⁶ this is sufficient for many applications, such as cell tracking, for detecting subcellular
¹⁷ features it might be limiting. One such example is chromosome tracking, which could shed
¹⁸ light on chromosome missegregation mechanisms in the early embryonic development,
¹⁹ which is the cause of many congenital diseases also affecting humans.

²⁰ In this chapter, we present a novel light-sheet microscope developed to address the
²¹ above challenges by using high NA objectives for subcellular isotropic resolution and low-
²² light imaging, and offering multi-view detection without having to rotate the samples.
²³ The microscope is designed to be live imaging compatible, offering new perspectives
²⁴ in the research of mouse embryonic development. This chapter will describe the design
²⁵ concepts for the microscope, the optical layout, alignment strategies, and the result of
²⁶ various performance measurements, and its multi-view imaging capabilities.

²⁷ **2.1 Microscope design concept**

¹ As the limiting factor for subcellular imaging with the original Mouse-SPIM is the poor
² axial resolution relative to the lateral, our first aim was to increase the axial resolution
³ to ideally reach the lateral resolution. A common way to reach isotropic resolution is to

2. DUAL MOUSE-SPIM

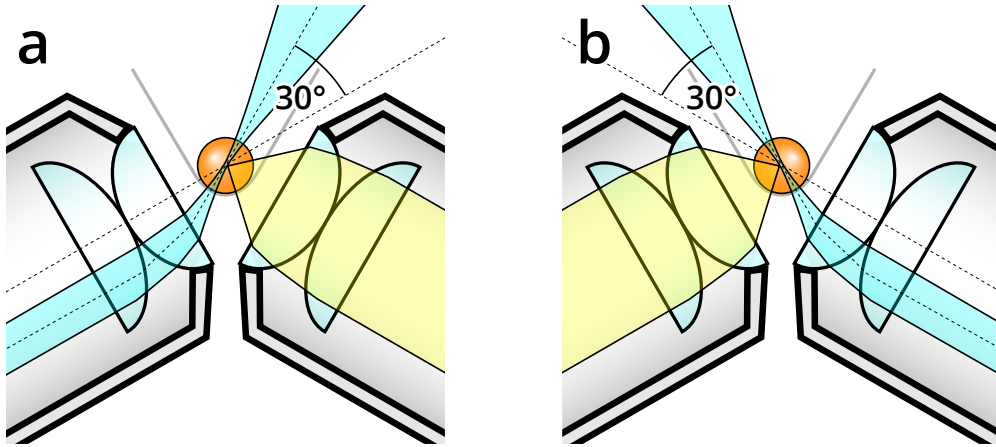


Figure 2.1: Dual view concept with high NA objectives. To achieve multi-view detection while maximizing resolution and light collection efficiency, two high NA objectives are placed in 120° arrangement. The sample (orange) is held from below by a thin FEP foil. To be able to overlap the light-sheet with the focal plane, the light-sheet is tilted 30° . The objectives are used in an alternating sequence for illumination and detection.

4 image a specimen from multiple directions, and combine the resulting images by multi-
 5 view deconvolution [28, 95, 96]. This has the benefit that the high resolution information
 6 from one view can complement the low axial resolution of the other view, thus providing
 7 better resolution in all three directions.

8 As described in the previous chapter, many SPIM implementations allow for recording
 9 multiple views either by rotating the sample, or by surrounding the sample with multiple
 10 objectives that are used for detection (Figure 1.10). For our setup, following the sample
 11 mounting technique of the original Mouse-SPIM, we wanted to keep the open-top sample
 12 mounting possibility, as this was proven to be highly compatible with mouse embryo
 13 imaging. To be able to achieve multi-view detection in this configuration, we designed a
 14 setup where both objectives can be used for illumination and detection in a sequential
 15 manner, inspired by previous symmetrical SPIM designs [43, 97].

16 To achieve the highest possible resolution from two views, the core of our design is
 17 based on the symmetric arrangement of two Nikon CFI75 Apo LWD 25x water dipping
 18 objectives, with a numerical aperture of 1.1. Due to the large light collection angle of
 19 these objectives, we arrange them in 120° instead of the conventional 90° used for light-
 20 sheet imaging. As the light-sheet still needs to coincide with the imaging focal plane of
 21 the objectives, we tilt the light-sheets by 30° (Figure 2.1). Due to the low NA of the
 22 light-sheet, this is possible without affecting illumination quality.

23 This 120° arrangement has several benefits when compared to the traditional 90°
 24 configuration. When placing the objectives in 90° , the largest possible light collection
 1 half-angle for an objective can be $\alpha_{max,90} = 45^\circ$, and the corresponding NA is $NA_{max,90} =$
 2 $n \cdot \sin \alpha_{max,90} = 0.94$, where $n = 1.33$ the refractive index of water. Considering that
 3 this is an idealized case, the practically available highest NA is only 0.8. For a 120°

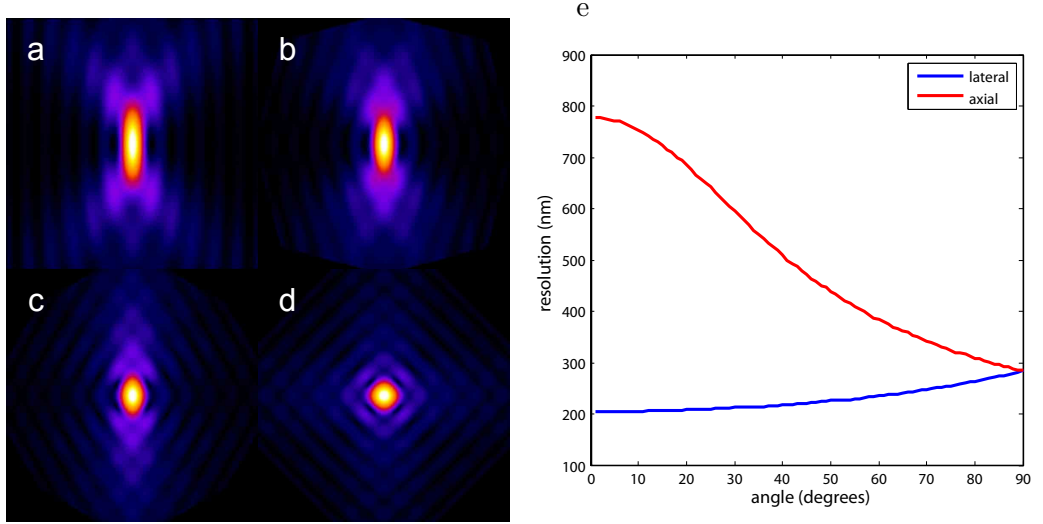


Figure 2.2: Lateral and axial resolution of a multi-view optical system. a) Simulated PSF for a single view. b)-d) Simulated compound PSF of two views aligned in b) 30, c) 60 and d) 90 degrees to each other. e) Axial and lateral resolution of a dual-view setup depending on the rotation angle of the two objectives. Parameters used for calculations: NA=1.1, $\lambda_{ex} = 488\text{nm}$, $\lambda_{det} = 510\text{nm}$, $n = 1.333$ for water immersion.

arrangement, the theoretical maximum is $\text{NA}_{max,120} = n \cdot \sin(120^\circ/2) = 1.15$, with a practical maximum NA of 1.1.

Although the resolution won't be completely isotropic when combining the images from two 120° views (Figure 2.2), as it is for 90° views, due to the higher maximum NA possible, the resolution can be higher in the 120° case. When simulating the combined multi-view PSFs (Figure 2.2), for 0.8 NA objectives in 90° the axial and lateral resolutions are both 317 nm; while for two 1.1 NA objectives in 120° the axial resolution will be identical, 317 nm, and the lateral will be better, 193 nm.

Although this difference in resolution may seem marginal, the 120° configuration has another advantage in light collection efficiency. Collecting as much of the fluorescence signal as possible is crucial in live imaging applications, due to the limited available photon budget (see Figure 1.1 and [9]). Collecting more light from the sample allows to image faster with the same contrast, or to reduce the illumination power and maintain the imaging speed. As light collection efficiency depends on the solid angle subtended by the detection lens, (see Appendix C), a 1.1 NA objective can collect twice as many photons as a 0.8 NA objective, which gives the 120° setup a clear edge in low-light imaging.

2.1.1 Light-sheet design

To allow for flexibility in the field of view height, even illumination, reduced stripes, and potential for confocal line detection, we opted to use the beam scanning technique to generate a virtual light-sheet. The effective focal length of the Nikon 25x objective, given

2. DUAL MOUSE-SPIM

⁴ the 200 mm focal length tube lens is

$$f_o = \frac{f_{tl}}{M} = \frac{200 \text{ mm}}{25} = 8 \text{ mm}, \quad (2.1)$$

⁵ and the back aperture diameter is 17.6 mm.

⁶ To generate the tilted light-sheet as shown on Fig. 2.1, the illumination beam will
⁷ need to be displaced by

$$\delta = f_o \cdot \tan 30^\circ = 4.62 \text{ mm} \quad (2.2)$$

⁸ Since the Gaussian beam is not uniform, only a smaller portion of it can be used to
⁹ maintain even illumination (Figure 1.12c). Because the size of an early mouse embryo
¹⁰ is around 80 μm , we require the length and the height of the light-sheet to be at least
¹¹ 100 μm .

¹² The length and thickness of the light-sheet

¹³ As we saw in section 1.3.1, the length of the light-sheet is determined by the Rayleigh-
¹⁴ range of the beam in the zy plane. Since $l_{fov} = 2 \cdot z_R = 100 \mu\text{m}$

$$z_R = 50 \mu\text{m} \quad (2.3)$$

¹⁵ Since the Rayleigh range and the diameter of the beam waist are coupled, the light-sheet
¹⁶ thickness can be calculated after rearranging Equation 1.20

$$2 \cdot W_0 = 2 \cdot \sqrt{\frac{z_R \cdot \lambda}{\pi}} = 5.57 \mu\text{m} \quad (2.4)$$

¹⁷ when $\lambda = 488 \text{ nm}$ for GFP excitation. As the beam width for these calculations is defined
¹⁸ as $1/e^2$ of the peak intensity, we also calculate the more commonly used full width at
¹⁹ half maximum (FWHM):

$$\text{FWHM} = W_0 \cdot \sqrt{2 \ln 2} = 3.28 \mu\text{m}. \quad (2.5)$$

¹ From this, the divergence angle of the beam is

$$\theta_0 = \frac{\lambda}{\pi W_0, y} = 55.74 \text{ mrad} = 3.196^\circ \quad (2.6)$$

² This means, the numerical aperture needed to produce this light-sheet is:

$$\text{NA}_{ls} = n \cdot \sin(\theta_0) = 0.0743 \quad (2.7)$$

³ Since $\text{NA} = 1.1$, and the diameter of the back aperture is $d = 17.6 \text{ mm}$ and the divergence

4 angle $\theta_0 \ll 1$, using paraxial approximation, the necessary beam width at the back focal
5 plane in the y direction is

$$b_y = d \cdot \frac{NA_{ls}}{NA} = 1.19 \text{ mm} \quad (2.8)$$

6 Thus, to generate a light-sheet with appropriate length to cover a whole mouse pre-
7 implantation embryo, the laser beam diameter should be $b = 1.19 \text{ mm}$. Larger than this
8 will result in a more focused beam and a shorter light-sheet, while a smaller diameter
9 beam will have worse optical sectioning capabilities.

10 **The height of the light-sheet**

11 The height of the light-sheet can be adjusted by changing the beam scanning am-
12 plitude with the galvo mirror. To scan the entire field of view of $h_{FOV} = 270 \mu\text{m}$,
13 the scanning angle range at the back focal plane of the objective will need to be
14 $\theta = \tan^{-1}(h_{FOV}/2/f_o) = \pm 0.967^\circ$.

15 **2.2 Optical layout**

16 Based on the requirements and other considerations shown in the previous section, the
17 microscope was designed in three main parts: 1) the core unit, 2) illumination and 3)
18 detection branches. The aim when integrating these units together was to allow for high
19 level of flexibility with robust operation, while also keeping efficiency in mind. After
20 finalizing the concept, the optical layout of the microscope was designed in SolidWorks.

21 **2.2.1 Core unit**

22 As the most important part of the microscope is actually the sample, the design is based
23 around a core consisting of the imaging chamber and the objectives (Figure 2.3). Also
24 part of the core are two mirror blocks placed at the back of the objectives, and three
25 custom designed rings to hold the objectives in place. The objectives are pointing slightly
26 upwards, closing a 60° angle with the horizontal plane, and 120° angle with each other.

27 **Chamber**

28 The chamber serves two purposes: it holds the immersion liquid necessary for imaging,
29 and it also keeps the objectives in the 120° position. The objectives are held by their
30 necks as opposed to the standard mounting method from the back by the threads. The
1 advantage of this is that any axial movements due to thermal expansion are greatly
2 reduced, thus the focal plane position is more stable even when changing the imaging
3 conditions.

2. DUAL MOUSE-SPIM

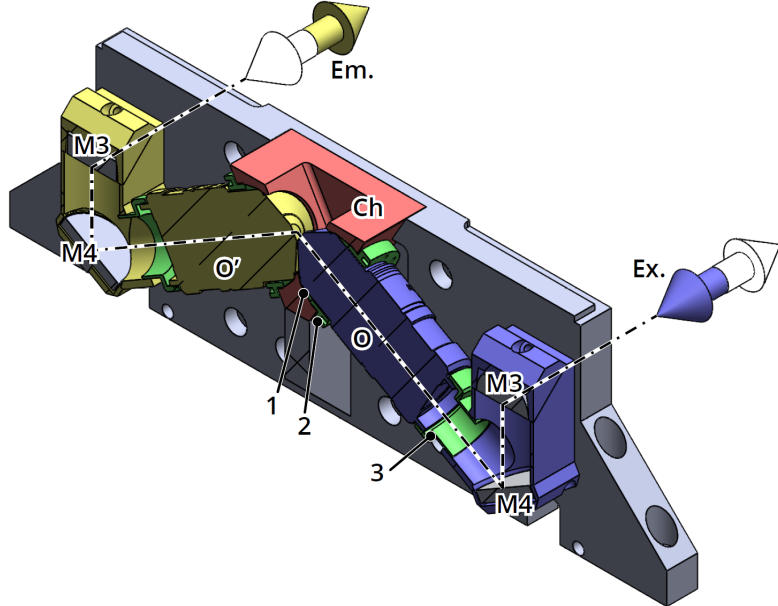


Figure 2.3: The core unit of the microscope. The two objectives (O and O') are mounted on a solid 15 mm thick aluminium plate. Fitting on the objectives, a custom chamber (Ch) is holding the immersion medium for imaging. The mirror block with mirrors $M3$ and $M4$ directs the light to 65 mm optical rails. Excitation (Ex.) and emission (Em.) light paths are indicated by the dash-dot line. Due to the symmetric arrangement, the excitation and illumination paths can be switched around. Objectives are secured with rings 1–3 (green, see main text for details).

4 The chamber is machined from a high performance plastic, polyether ether ketone
 5 (PEEK). This material has many beneficial properties: it is food safe, and chemically
 6 extremely inert, resisting to most solvents used in a biology laboratory. It can also be
 7 autoclaved. Compared to other plastics its mechanical properties are also superior. It has
 8 high tensile and compressive strength, comparable to aluminium, low thermal expansion
 9 and low thermal conductivity. This can be beneficial when implementing temperature
 10 control, as thermal loss is reduced.

11 The objectives are kept in place by two custom designed rings (Figure 2.3 1, 2).
 12 The first ring has a cross sectional shape of a wedge, and sits tightly against both the
 13 objective and the wall of the chamber. The second ring can freely slide on the objective,
 14 and has threads matching the chamber. When turned in, the threaded ring pushes the
 15 wedge ring further in, which in turn presses against the objective and the chamber wall
 16 uniformly, thus preventing the objective from moving, and sealing the chamber at the
 17 same time. As the wedge ring is made from a soft plastic (delrin), it will press evenly
 18 against the objective preventing any damage. Given the conical shape of the ring, it will
 19 also automatically center the objective, ensuring correct positioning.

1 To relieve any rotational stresses from the objective, the back of the objective is also
 2 supported by the mirror block, this is not fixed, however. A third ring, made of PEEK
 3 is threaded on the objective, and slides in the opening of the mirror block. This reduces

4 the torque on the objectives, while still allowing for some movements that might occur
5 due to thermal expansion.

6 Mirror blocks

7 Apart from supporting the objectives from the back, the mirror blocks are housing two
8 broadband dielectric mirrors (Thorlabs, BBE1-E03 and OptoSigma, TFMS-30C05-4/11)
9 to direct the light to and from the objectives on a standard 65 mm height, compatible
10 with the Owis SYS65 rail system. The combination of two mirrors have two benefits
11 compared to using just one. With a single mirror directly reflecting the light to the back,
12 the entire assembly would need to be much higher to reach the desired 65 mm height.
13 This could result in stability problems. Furthermore, due to the 60° rotation angle of the
14 objective, the image of the objective would also be rotated if using only a single mirror.
15 With two mirrors the reflection planes can be kept orthogonal to the optical table, which
16 will result in a straight image after the mirror block. This is not only beneficial when
17 recording the images, but also when aligning the illumination arm. With the use of two
18 mirrors, a convenient vertical scanning is required to produce the light-sheet; with a
19 single mirror, the scanning direction would need to be rotated by 60°.

20 2.2.2 Illumination

21 The illumination arm of the microscope directs and shapes the laser beam to generate
22 the proper light-sheet dimension at the sample. As was calculated in subsection 2.1.1, a
23 beam diameter of 1.2 mm is ideal for this setup.

24 The illumination arm has three main roles:

- 25 1. expands the laser beam to the calculated 1.2 mm size.
26 2. images the galvo scanner to the back focal plane of the objective
27 3. switches the laser light between the two objectives during imaging

28 To achieve the desired beam diameter, a 1:2 beam expander (Sill Optics, 112751) is
29 used in the reversed direction. As the output of the laser fiber produces a 3 mm diameter
30 beam, this will reduce it to 1.5 mm. As this is already the required beam diameter, the
31 lenses further in the illumination path will not introduce any magnification.

32 Switching between the two illumination arms is performed by a custom designed beam
33 splitter unit (Figure 2.4). Instead of utilizing a 50/50 beam splitter cube and mechanical
34 shutters, we exploit the fact that a galvo scanner is needed to generate the light-sheet.
1 As this galvo scanner (Cambridge Technology, 6210B) has a relatively large movement
2 range ($\pm 20^\circ$) it is also suitable for diverting the beam from one illumination arm to the
3 other.

2. DUAL MOUSE-SPIM

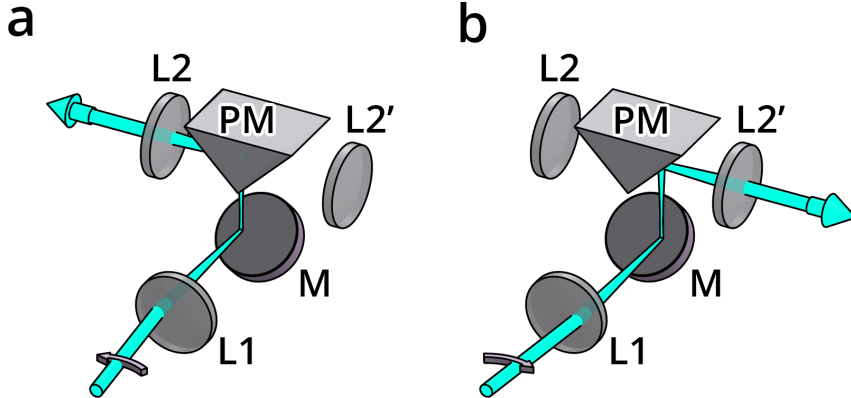


Figure 2.4: Illumination branch splitting unit. To divert the beam to either side, a right angle prism mirror is used in conjunction with a galvanometric scanning mirror. L1 acts as a scan lens, thus the beam is translated on mirror M. Depending on the galvo angle, the beam will be reflected either to the left (**a**) or to the right (**b**). L2 and L2' act as relay lenses, and will image the galvo movement to intermediate planes.

4 Switching illumination side is done the following way. As the galvo is positioned at
 5 the focus of the first lens (L1, $f_1 = 75$ mm, Edmunds Optics, #47-639), the rotational
 6 movement will result in a linear scanning movement on mirror M and the prism mirror
 7 PM (Figure 2.4). Depending on the lateral position of the beam, it will hit either the
 8 left or the right leg of the prism (Thorlabs, MRAK25-E02), and will be reflected to
 9 either direction. As the galvo mirror can be precisely controlled through our custom
 10 software, we can set and save the position when the beam is centered on the left lens L2
 11 ($f_2 = 75$ mm, Edmunds Optics, #47-639) (Figure 2.4a) and the position when the beam
 12 is centered on the right lens L2' (Figure 2.4b). Lenses L1 and L2(L2') form a 4f system,
 13 and are imaging the galvo scanner on mirror M1(M1') (Figure 2.5). This way we can use
 14 the same galvo to generate the light-sheet for both directions, depending on the initial
 15 offset position. This not only has the advantage of being able to electronically switch the
 16 illumination arms, but only requires a single galvo scanner instead of one for each arm.

17 Due to the arrangement of the bottom mirror and the prism mirror, the scanning
 18 direction will be rotated by 90°. This will result in a vertical scanning plane, which is
 19 exactly what we need to generate the light-sheet on the sample (see section 2.2.1).

20 Further following the illumination path, two achromatic lenses L3 and L4 ($f_3 = f_4 =$
 21 200 mm), in a 4f configuration relay the scanning axis to the back focal plane (BFP) of
 1 the objective. To couple in the laser with the imaging path, a quad-band dichroic mirror
 2 (DM, Semrock, Di03-R405/488/561/635-t3-25x36) is used, matching the wavelengths of
 3 the laser combiner.

2.2 Optical layout

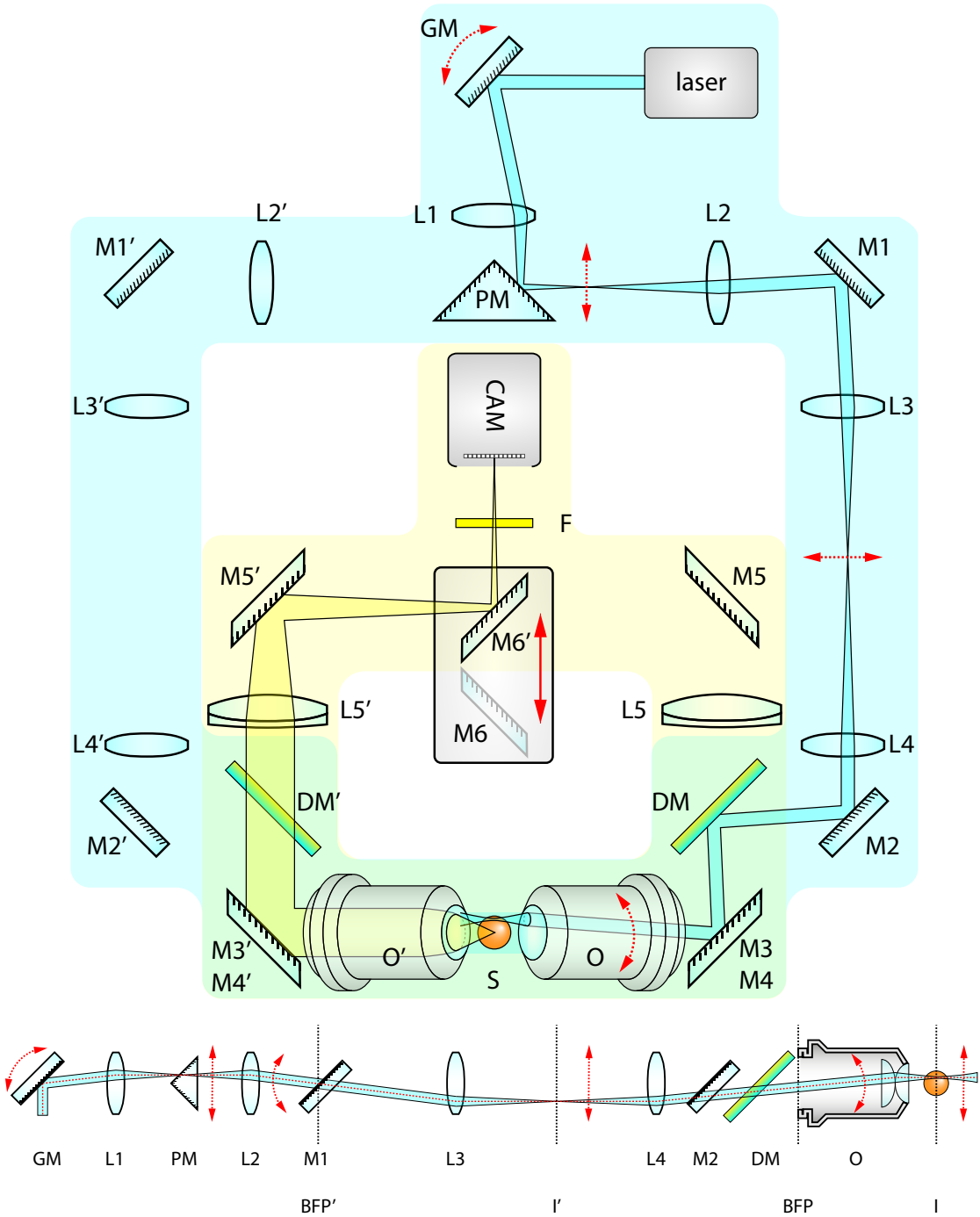


Figure 2.5: Dual Mouse SPIM optical layout. The microscope consists of two main parts, the illumination branches (blue) and detection branches (yellow). For both illumination and detection there are two identical paths implemented. Illumination direction can be changed by applying a different offset to the galvo mirror, which in turn will direct the beam to the opposite face of the prism mirror. L1 and L2 will then image the galvo on M1. Using L3 as a scan lens, and L4 as a tube lens, the scanned beam is coupled to the objective path by quad band dichroic mirror (DM) CAM – camera, DM – dichroic mirror, F – filter wheel, L – lens, M – mirror, O – objective, PM – prism mirror, S – sample

2. DUAL MOUSE-SPIM

4 2.2.3 Detection

5 As the emitted light exits the objective and the mirror block, it is decoupled from the
6 illumination path by the dichroic mirror. The light is then focused by a 400 mm achro-
7 matic lens (L5, Edmunds Optics, #49-281) onto the camera sensor (Andor Zyla 4.2
8 sCMOS). Just before the camera, a motorized filter wheel (F, LEP 96A361) is placed to
9 discriminate any unwanted wavelengths from the emission light. Although this is not in
10 the infinity space, due to the very small angles after the 400 mm tube lens, the maximum
11 axial focal shift is ~ 50 nm only, which is negligible compared to the axial resolution of
12 ~ 1.1 μ m.

13 Similarly to the common galvo in the illumination path, the two detection arms
14 share the same camera. Although two cameras could also be used, due to the operating
15 principle of the microscope, the two objective are not used for imaging at the same time.
16 This means a single camera is capable of acquiring all the images, however, the two
17 distinct detection arms need to be merged to be able to use a single detector.

18 Our solution to this problem is a custom designed view switching unit comprised of
19 two broadband dielectric elliptical mirrors (Thorlabs, BBE1-E03) facing opposite direc-
20 tions, mounted on a high precision linear rail (OptoSigma, IPWS-F3090). Depending on
21 the rail position, either the left (Figure 2.6a) or the right (Figure 2.6b) detection path
22 will be reflected upwards, to the camera.

23 Moving the switcher unit is performed by a small, 10 mm diameter pneumatic cylinder
24 (Airtac, HM-10-040) that is actuated by an electronically switchable 5/2 way solenoid
25 valve (Airtac, M-20-510-HN). This solution offers a very fast switching between views,
26 up to 5 Hz, depending on the pressure, and it is extremely simple to control, as only a
27 digital signal is necessary to switch the valve.

28 2.3 Optical alignment

29 Precise alignment of the illumination and detection paths are crucial for high quality
30 imaging, and has a pronounced importance for high magnification and high resolution
31 optical systems. The DualMouse-SPIM contains two illumination and detection paths
32 Due to the symmetrical setup of the microscope, we will only describe the alignment of
33 one side, as the same procedure is also applicable to the other side.

34 2.3.1 Alignment of illumination branches

35 The two illumination branches start with a common light source, a single mode fiber
1 coupled to laser combiner, and they also share a galvanometric mirror that performs the
2 beam scanning to generate the virtual light-sheet. Likewise shared is a scan lens focusing
3 on the galvo mirror (GM), and the illumination splitter unit (PM, see Section 2.2.2).

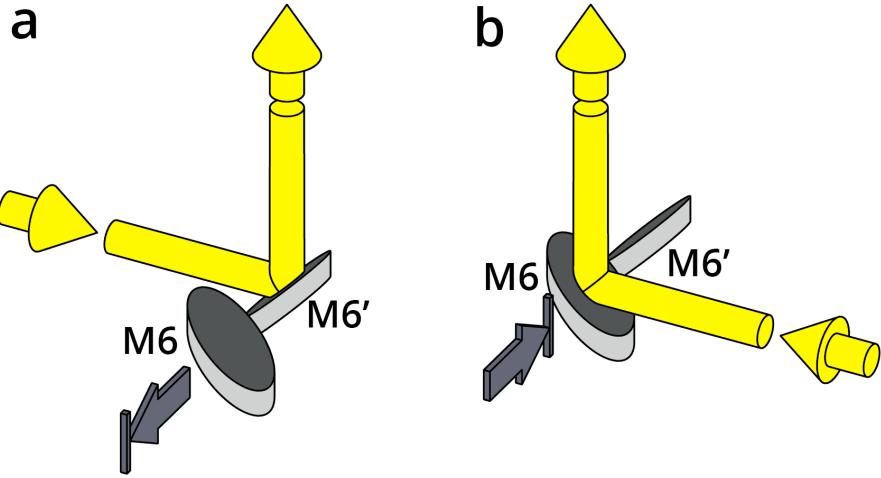


Figure 2.6: Detection branch switching unit. To be able to image both views on the same camera, a moveable mirror unit is introduced. Depending on the imaging direction, the mirror block is either moved backward (a) or forward (b) to reflect the light up to the camera. Since the movement is parallel to the mirrors' surface, the image position on the sensor is not dependent on the exact position of the mirrors.

4 Alignment for the illumination arms are done in three steps. First the laser beam
 5 is aligned on the first rail that holds the galvo, lens L1, and the splitter unit PM. This
 6 is performed by two kinematic mirrors placed between the fiber output and the galvo
 7 mirror (not shown on figure). Using these two mirrors it is possible to freely align the
 8 beam along all four degrees of freedom: translation in two orthogonal directions and
 9 rotation around two orthogonal axes. Beam alignment on the rail is tested by two irises
 10 at the two ends of the rail, if the beam passes through both of them we consider it
 11 centered and straight on the optical axis.

12 After the beam is aligned on the first rail, lens L1 and the splitter unit PM are placed
 13 in the measured positions to image the galvo mirror on mirror M1 using lenses L1 and
 14 L2. Correct positioning of the splitter unit along the rail is crucial, since this will affect
 15 the lateral position and tilt of the beam exiting the unit. To some extent, this can also
 16 be compensated by adjusting the two mirrors before the galvo mirror, but is avoided if
 17 possible as this will also displace the beam from the center of the galvo mirror.

18 After rough alignment of the illumination arms, when the laser is already coupled
 19 in the objective, the fine adjustments are performed based on the image of the beam
 20 through the other objective. The beam is visualized by filling the chamber with a 0.1%
 21 methylene blue solution. As this solution is fluorescent, and can be excited in a very large
 22 range, it is well suited to visualize the beam during adjustment.

1 **Adjusting beam position** Beam position can be adjusted by either translating the
 2 beam in a conjugated image plane (I'), or by rotating the beam in a conjugated back focal
 3 plane (BFP'). The setup was designed in a way, that BFP' coincides with mirror M1.

2. DUAL MOUSE-SPIM

4 This mirror is mounted in a gimbal mirror mount, allowing to rotate the mirror exactly
5 around its center, which avoids unwanted translational movements, and results in pure
6 rotation of the beam. Lens L3 is positioned exactly 1 focal length from the mirror, thus
7 acting as a scan lens, and transforming the rotational movements to translation. This
8 translation is further imaged and demagnified by the tube lens L4 and the objective O
9 onto the sample.

10 **Adjusting beam tilt** Beam tilt can be adjusted by either rotating the beam in an in-
11 termediate image plane (I'), or translating it at the back focal plane (BFP). As mirror M2
12 is relatively far from the back focal plane, adjusting this will mostly result in translation
13 that will rotate the beam. This movement, however, will also introduce translations, and
14 has to be compensated by adjusting mirror M1. As the light-sheet needs to be tilted by
15 30° to coincide with the focal plane of the other objective, this level of adjustment is not
16 possible with M2. In order to allow for a pure rotation of the light-sheet, we mounted the
17 dichroic mirrors on linear stages (OptoSigma, TSDH-251C). By translating the dichroic
18 mirror, the illumination laser beam gets translated at the back focal plane, which will
19 result in a pure rotational movement at the sample. Rough alignment of the light-sheet
20 is performed by adjusting the dichroic position while inspecting the light-sheet through
21 a glass window in the chamber. Precise alignment is afterwards done based on the image
22 of the beam visualized in a fluorescent medium.

23 **Adjusting scanning plane angle** After the beam is properly aligned, i.e. it is in focus
24 and in the center of field of view, it is still necessary to check if the scanning direction
25 is parallel to the imaging plane. It is possible that the beam is in focus in the center
26 position, but when moved up or down it drifts out of focus due to a tilted scanning
27 angle. This tilt can be compensated by mirror M1, that is placed at the conjugated back
28 focal plane BFP' . Between lenses L3 and L4 a magnified version of the light-sheet will
29 be visible, and the tilt can be checked by placing an alignment target in the optical path
30 while scanning the beam. By tilting mirror M1 up or down, the scanning pattern not only
31 moves up or down, but is also rotated if the mirror surface is not exactly vertical. Since
32 M1 and GM are in conjugated planes, the tilt and offset can be performed independently.
33 The tilt is first fixed by M1 while inspecting the target, and the beam is re-centered by
34 changing the offset on the galvo mirror. Moving the galvo mirror will not introduce tilt,
35 since in this case rotation axis is perpendicular to the reflection plane.

1 2.3.2 Alignment of detection branches

2 Since the detection path is equivalent to a wide-field detection scheme, its alignment is
3 much simpler than that of the illumination branches. The only difference is the detection

4 branch merging unit (see subsection 2.2.3.) that features two moving mirrors. This,
5 however, doesn't affect the alignment procedure, since the movement direction is parallel
6 to both mirrors' surfaces, meaning that the exact position of the mirrors will not affect
7 the image quality, as long as the mirrors are not clipping the image itself. A stability
8 test was performed to confirm the consistent switching performance of the mirror unit
9 before the final alignment took place (see subsection 2.5.1).

10 **Positioning the tube lens** The position of the tube lens determines the focal plane
11 that is being imaged on the camera sensor. Ideally, the tube lens' distance from the
12 camera sensor is exactly the tube lens' focal length, which will ensure the best imaging
13 performance. If the tube lens' distance is not correct, the focal plane will be slightly
14 shifted in the axial direction. Although small shifts will not necessarily have detrimen-
15 tal effect on the image quality, because the light sheet can also be shifted accordingly.
16 Because of the shifted focal and image planes, however, the magnification of the system
17 will be affected, and will change depending on the amount of defocus. For this reason we
18 aim for positioning the tube lens as close to the theoretical position as possible.

19 Our tube lens is a compound, achromatic lens with a center thickness of 12.5 mm, and
20 edge thickness of 11.3 mm. Its effective focal length is 400 mm which will produce a 50x
21 magnified image. Back focal length is 394.33 mm which we measured form the camera
22 chip, and the lens was positioned at this theoretically optimal position.

23 **Adjusting correction collar** The Nikon 25x objectives used for this setup have a
24 built in correction ring that can be used to correct spherical aberrations resulting from
25 refractive index differences when imaging samples behind a coverslip. This can be also
26 effectively used to correct for any spherical aberrations occurring from imaging through
27 the FEP foil. Although these aberrations are expected to be extremely low, due to the
28 relatively thin, 50 μm foil thickness, and the close matching of refractive index ($n_{FEP} =$
29 1.344, $n_{H_2O} = 1.333$), for optimal, aberration free image quality it can't be neglected.

30 The correction collars are adjusted by inspecting a gel suspended fluorescent bead
31 specimen with the microscope, where the beads can act as a reporter of the point spread
32 function of the microscope. The alignment can be performed "live" by inspecting the
33 bead image quality for any aberrations. By gradually changing the correction collar, the
34 ring are minimized on out-of-focus beads, and the peak intensity is maximized for in-
35 focus beads. By moving the correction ring, the focal plane is also slightly shifted, which
36 has to be compensated by shifting the light-sheet correspondingly to coincide with the
1 correct imaging plane.

2 **Adjusting field of view** To allow for proper sampling of the image, we use 50 \times magni-
3 fication, which combined with the 6.5 μm pixel pitch of our sCMOS camera, will result

2. DUAL MOUSE-SPIM

4 in a $0.13\text{ }\mu\text{m}$ pixel size. The full field of view with this magnification is $2048 \times 0.13\text{ }\mu\text{m} =$
5 $266.24\text{ }\mu\text{m}$. The full field of view the objective provide, are larger than this at $800\text{ }\mu\text{m}$.
6 To ensure the best image quality, we align the center of the objective field of view on
7 the camera sensor, since this region has the best optical properties in terms of numerical
8 aperture, aberration correction and field flatness.

9 Field of view alignment can be performed using mirror M4 just before the detection
10 merging unit. To identify the center region of the field of view, diffuse white light is
11 used to illuminate the entire sample chamber and is imaged on the camera. Then, mirror
12 M4 is adjusted until the top edge of the field of view becomes visible, *i.e.* where the
13 illumination from the chamber is clipped. This will have a circular shape. Afterwards,
14 adjusting the mirror in the orthogonal direction, the left-right position of the field of
15 view can be adjusted, by centering the visible arc on the camera sensor.

16 After the horizontal direction is centered, vertical centering is performed. This, how-
17 ever can't be centered the same way as the horizontal direction, since for that we would
18 have to misalign the already aligned horizontal position. To determine the center, we
19 move the field of view from the topmost position to the bottom. During this process
20 the number of turns of the adjustment screw is counted (this can be done accurately by
21 using a hex key). After reaching the far end of the field of view, the mirror movement is
22 reversed, and the screw is turned halfway to reach the middle.

23 2.4 Control unit

24 The microscope's control and automation is performed by an in-house designed modular
25 microscope control system developed in LabVIEW [97]. The core of the system is a
26 National Instruments cRIO-9068 embedded system that features an ARM Cortex A9
27 processor, and a Xilinx Zynq 7020 FPGA. Having both chips in the same device is a
28 great advantage, since the main processor can be used to run most of the microscope
29 control software, while the FPGA can be used to generate the necessary output signals
30 in real time and with high precision.

31 The embedded system is complemented by a high performance workstation that is
32 used to display the user interface of the microscope, and to record the images of the
33 high-speed scientific complementary metal-oxide-semiconductor (sCMOS) camera.

34 2.4.1 Hardware

35 Various components need to be synchronized with high precision to operate the mi-
1 croscope: a laser combiner to illuminate the sample; a galvo scanner to generate the
2 light-sheet; stages to move the samples; filter wheel to select the imaging wavelengths;
3 and a camera to detect the fluorescence signal. For high speed image acquisition, all of

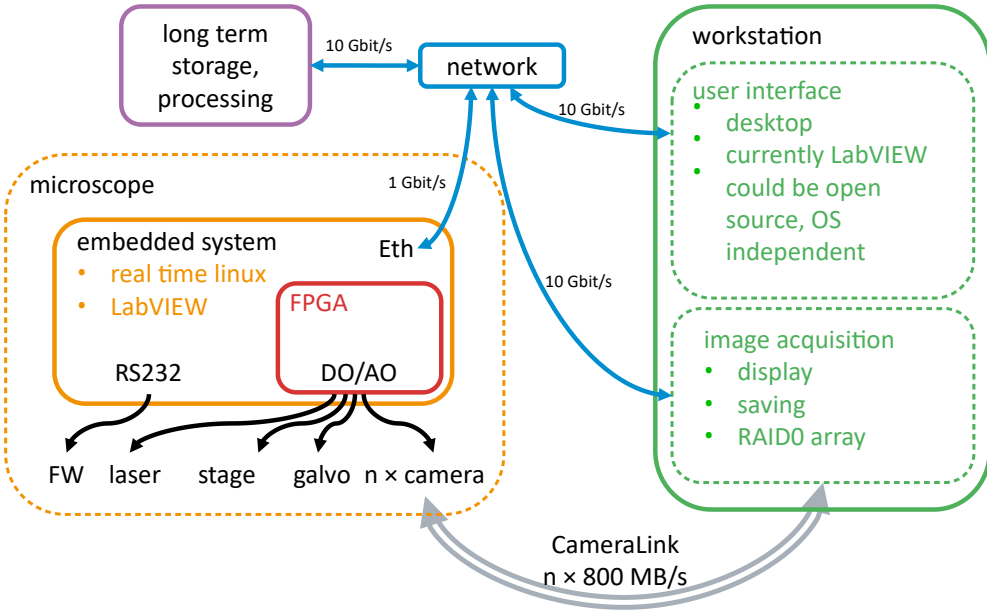


Figure 2.7: Microscope control hardware and software architecture. The embedded system responsible for the hardware control and the workstation are communicating through the network using the WebSocket protocol. The electronic devices of the microscope are either controlled through digital/analog signals, or through serial communication. The camera is also connected to the workstation with a CameraLink connection, which transmits the recorded images.

- 4 these devices have to be precisely synchronized in the millisecond range, and some even
 5 in the microsecond range. Although they require different signals to control them, we
 6 can split them into three main categories:

	digital input	analog input	serial communication
7	camera exposure	galvo position	filter wheel
	laser on/off ($\times 3$)	laser intensity ($\times 3$)	stages ($\times 2$)

8 All devices are connected to the NI cRIO 9068 embedded system, either to the built
 9 in RS232 serial port, or to the digital and analog outputs implemented by C-series
 10 expansion modules (NI 9401, NI 9263, NI 9264). The workstation with the user interface
 11 is communicating with the embedded system through the network. The only device with
 12 a connection to both systems is the camera: the embedded system triggers the image
 13 acquisition, while the images are piped to the workstation through a dual CameraLink
 14 interface, capable of a sustained 800 MB/s data transfer rate (Figure 2.7).

15 2.4.2 Software

- 1 Being able to precisely control all of the instruments not only relies on the selected hard-
 2 ware, but just as much on the software. Our custom software is developed in LabVIEW,
 3 using an object oriented approach with the Actor Framework. The embedded system is

2. DUAL MOUSE-SPIM

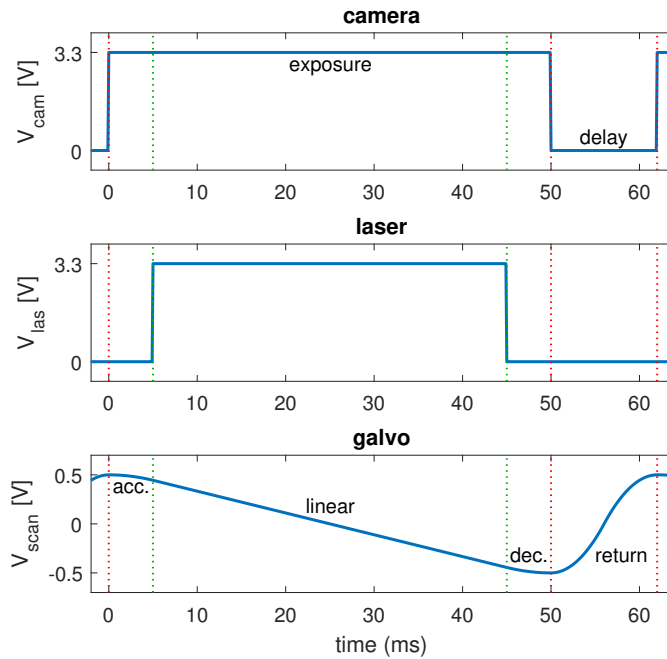


Figure 2.8: Digital and analog control signals. Example traces for recording a single plane with 50 ms exposure time and 12 ms delay. During the exposure of the camera the galvo has 3 sections: acceleration (acc.), linear, and deceleration (dec.). The laser line is synchronized with the galvo linear section to ensure even illumination.

4 responsible for the low level hardware control, for keeping track of the state of all devices,
 5 saving the user configurations, and automating and scheduling the experiments. It also
 6 offers a Javascript Object Notation (JSON) based application programming interface
 7 (API) through WebSocket communication. This is mainly used to communicate with the
 8 user interface, however it also offers the possibility of automated control by an external
 9 software.

10 **FPGA software**

11 The on-board FPGA is responsible for generating the digital and analog output signals
 12 based on the microscope settings (Figure 2.8). To avoid having to calculate all the traces
 13 for a whole stack, the main software only calculates a few key parameters of the traces
 14 that are necessary to completely describe them. The FPGA then calculates the signals
 15 in real time, and outputs them with microsecond precision.

16 To describe the traces, we define them as a concatenation of *sections*. Each section has
 17 3 or 5 parameters, depending on if their type is digital or analog. Both types have three
 18 common properties: `value`, `length`, and `type`. The analog sections additionally contain a
₁ `dValue` and a `ddValue` element describing the velocity and the acceleration of the signal.
₂ This allows us to generate piecewise functions made of second order polynomials.
₃ The `type` element contains information on which value should be updated for the

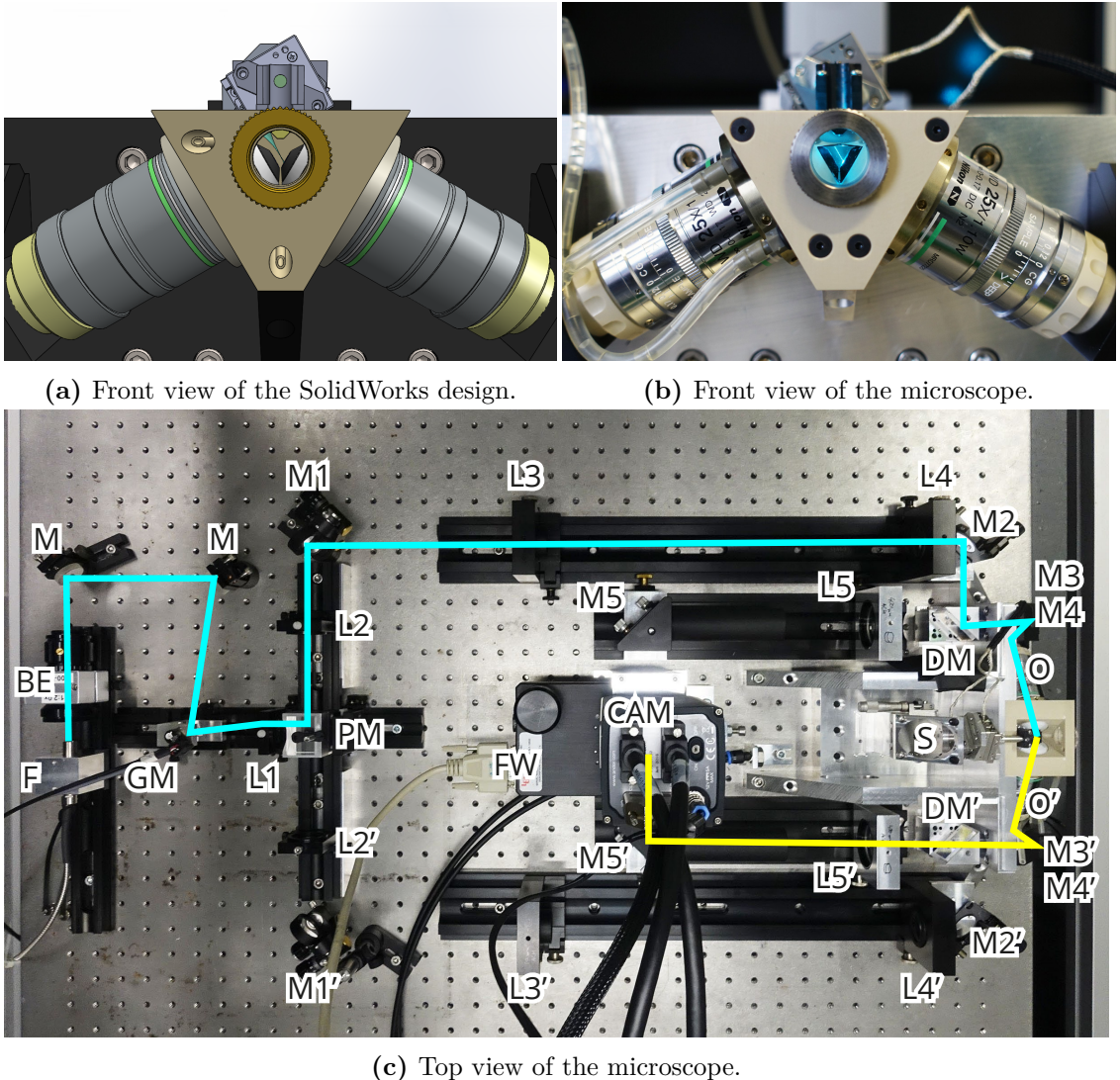


Figure 2.9: Completed DualMouse-SPIM. The excitation and emission light paths are depicted with blue and yellow lines respectively. Component numbering corresponds to Figure 2.5. Detection branch merging unit, and mirrors M6 and M6' are underneath the camera and filter wheel. BE – beam expander, CAM – camera, DM – dichroic mirror, F – fiber, FW – filter wheel, L – lens, M – mirror, O – objective, PM – prism mirror, S – stage

- 4 current section. Setting the lowest bit high will update the **value**, setting the second bit
- 5 high will update the **dValue**, and setting the third bit high will update the **ddValue**.
- 6 This feature allows to define smooth transitions between the sections, and also to define
- 7 more complex signals, as long as they are periodic in the second derivative.

1 2.5 Results

- 2 Following the design phase, all custom parts were manufactured by the EMBL mechanical
- 3 workshop, and microscope was assembled on a MellesGriot optical table (Fig. 2.9). The

2. DUAL MOUSE-SPIM

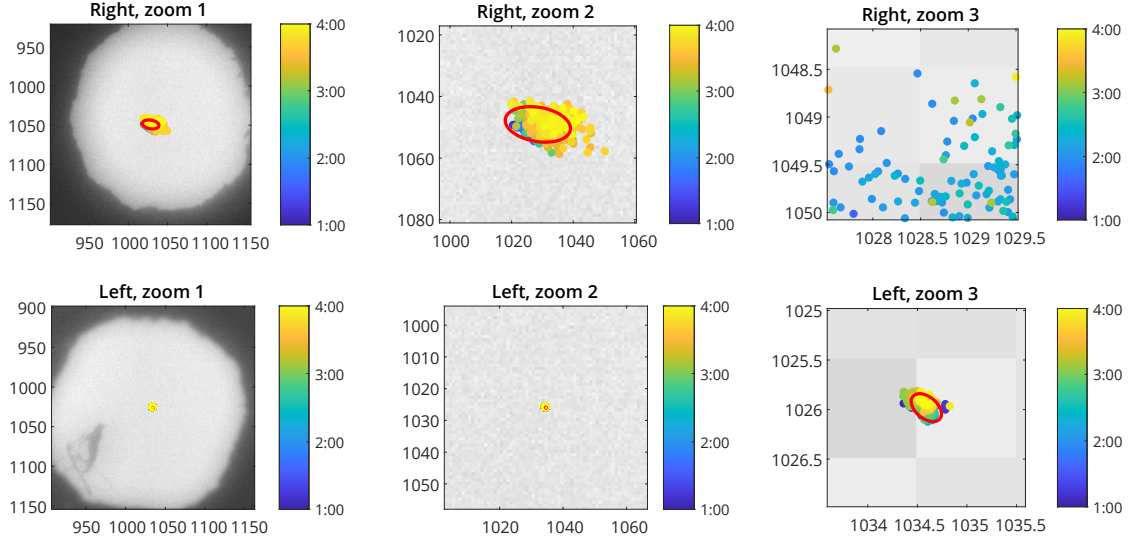


Figure 2.10: Stability measurements of view switcher unit. A closed aperture was imaged on the camera from both views, every 10s, for 4h. The dots represent the center of each frame, color coded with the time. The red ellipse represents the 95% confidence interval of the measured positions based on principal component analysis. Standard deviations for right view: $\sigma_1 = 4.37 \text{ px}$, $\sigma_2 = 2.26 \text{ px}$; for left view: $\sigma_1 = 0.07 \text{ px}$, $\sigma_2 = 0.04 \text{ px}$.

4 microscope was equipped with an Andor Zyla 4.2 sCMOS camera, that offers a large field
 5 of view of 2048×2048 pixels with a pixel pitch of $6.5 \mu\text{m}$. It offers a high dynamic range
 6 of 1:30,000, and high frame rate at 100 frames per second (fps), while readout noise is
 7 minimal (0.9 e^-).

8 To evaluate the performance of the microscope, we conducted various measurements,
 9 concerning the stability and the resolution of the system. The methods and results of
 10 these measurements will be presented in this section.

11 2.5.1 Stability of view switcher unit

12 As the view switcher unit is a custom designed solution for this microscope, it is necessary
 13 to evaluate the effect of the switching on the field of view. Given that this is a moving
 14 unit, many mechanical imprecisions can introduce a drift in the final image.

15 To assess the reproducibility in the movement of the detection branch switching unit,
 16 a long term stability test was conducted. To exclude all other factors (such as sample
 17 drift), we imaged the opening of two closed irises that were mounted on the detection
 18 optical rail. Image formation was done by two achromatic lenses ($f = 75 \text{ mm}$) positioned
 19 directly after mirrors M5 and M5'.

20 The apertures were imaged from both views every 10 seconds, for 4 h, for a total
 1 of 1440 images per view, and 2880 switches. The center of the aperture was segmented
 2 on all images using Matlab, and tracked to assess any drift occurring during the 4 h
 3 time lapse (Figure 2.10). To visualize the uncertainty of the aperture's position, we

4 performed principal component analysis (PCA) on the positions and visualized the results
 5 by plotting the 95% confidence ellipse on the images. Although the right view had a
 6 significant spread with a standard deviation of 4.37 px and 2.26 px along the long and
 7 short axes respectively, the left view was extremely stable, and the standard deviation
 8 was only 0.07 px and 0.04 px for the long and short axes respectively. This result implies
 9 that there is no conceptual limitation in reaching sub-pixel reproducibility with the view
 10 switching unit, although some optimization is still needed for the right view to reach the
 11 same stability as the left view.

12 2.5.2 Characterizing the illumination profile

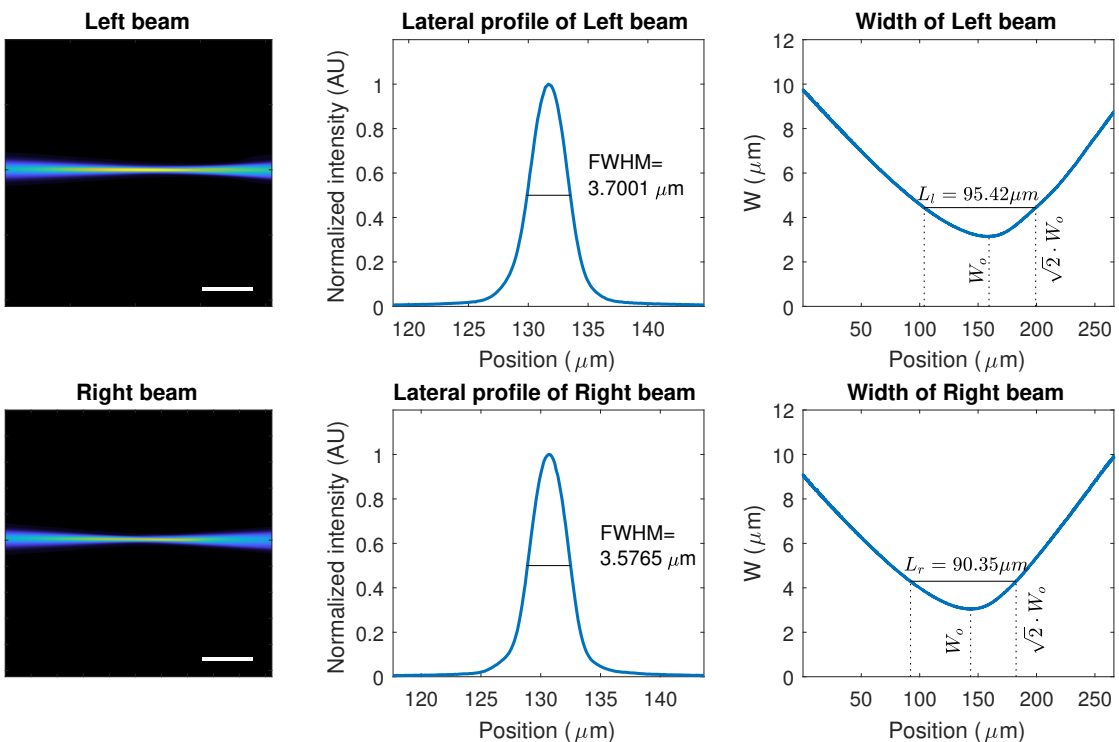


Figure 2.11: Illumination beam profile. Average of 500 stationary beam images for both left (top left) and right objectives (bottom left). Beam intensity profile along the waist of each beam is plotted in the center column. The right column shows the beam width profile of each beam ($1/e^2$).

13 Since a Gaussian beam is used for illumination, its intensity profile is dependent of
 14 the axial position (Equation 1.18). Although the total intensity at any cross section of
 15 the beam is constant, because of the divergent properties, the peak intensity varies. To
 16 assess any non-uniformities in the illumination pattern, we measured the illumination
 17 beam intensity for each view.

1 To visualize the beam, the chamber was filled with a fluorescent solution (0.1 %
 2 methylene blue in distilled water). In order to increase the signal to noise ratio of these
 3 images, a long exposure time of 200 ms was used, and 500 images of each beam was

2. DUAL MOUSE-SPIM

averaged. Dark images were acquired by repeating the image acquisition with the laser turned off. The average of the dark images were subtracted from the averaged beam images, resulting in the beam intensity profile (Figure 2.11).

To determine the beam waist position, we measured the beam thickness (FWHM) for each column of the averaged images, and located the position of the minimal width. The beam width at the waist position for the left view was $3.70\text{ }\mu\text{m}$, and for the right view it was $3.58\text{ }\mu\text{m}$ (Figure 2.11). We also measured the usable length of the beams (1.3.1). The distance between the points where the beam has expanded by a factor of $\sqrt{2}$ relative to the waist is $95.42\text{ }\mu\text{m}$ for the left view, and $90.35\text{ }\mu\text{m}$ for the right view. This corresponds well to the original requirement of a minimal field of view of $100\text{ }\mu\text{m}$. Depending on the sample and the required level of optical sectioning, the practical field of view can be larger than this, as the camera sensor allows for a field of view of $266\text{ }\mu\text{m}$.

2.5.3 Resolution and point spread function measurement

In order to establish an ideal, reference PSF, we simulated the theoretical PSF of the microscope with the Gibson-Lanni model [98], using the MicroscPSF Matlab implementation [99]. The advantage of this model is that it accounts for any differences between the experimental conditions and the design parameters of the objective, and thus it can simulate any possible aberrations that may arise. The adjustable parameters are the thicknesses (t) and refractive indices (n) of the immersion medium (i), coverslip (g), and sample (s). To simulate the reference PSF, we accounted for the slight mismatch in refractive index between the FEP foil ($n_g = 1.344$) and water ($n_i = 1.33$). The working distance of the objective is 2 mm, while the thickness of the foil is $50\text{ }\mu\text{m}$.

It is apparent from the simulations that even though the FEP refractive index is almost identical to the refractive index of water, a slight spherical aberration is still present even for the ideal case (Figure 2.12, left). The resolution measured as the FWHM of the intensity profile through the lateral and axial cross sections is 271 nm and 866 nm respectively. FWHM was measured in Fiji by fitting a Gaussian curve, and multiplying the standard deviation of the resulting fit by $2\sqrt{2 \ln 2}$.

To experimentally measure the resolution of the microscope and characterize its optical performance, we measured the point spread function using fluorescently labeled beads suspended in 0.8% GelRite (section 2.6). The gel was loaded in glass capillaries and allowed to cool. After the gel solidified, a $\sim 1\text{ mm}$ piece was cut off and placed in the microscope sample holder. The beads were imaged from both views using the 561 nm laser line with the 561 long-pass filter (Semrock, BLP02-561R-25).

From both views 12 beads were averaged using Fiji [100] and the 3D PSF estimator of the MOSAIC suite [101]. In order to acquire a more accurate PSF, the averaged bead images were deconvolved with the ideal image of the bead (uniform sphere width

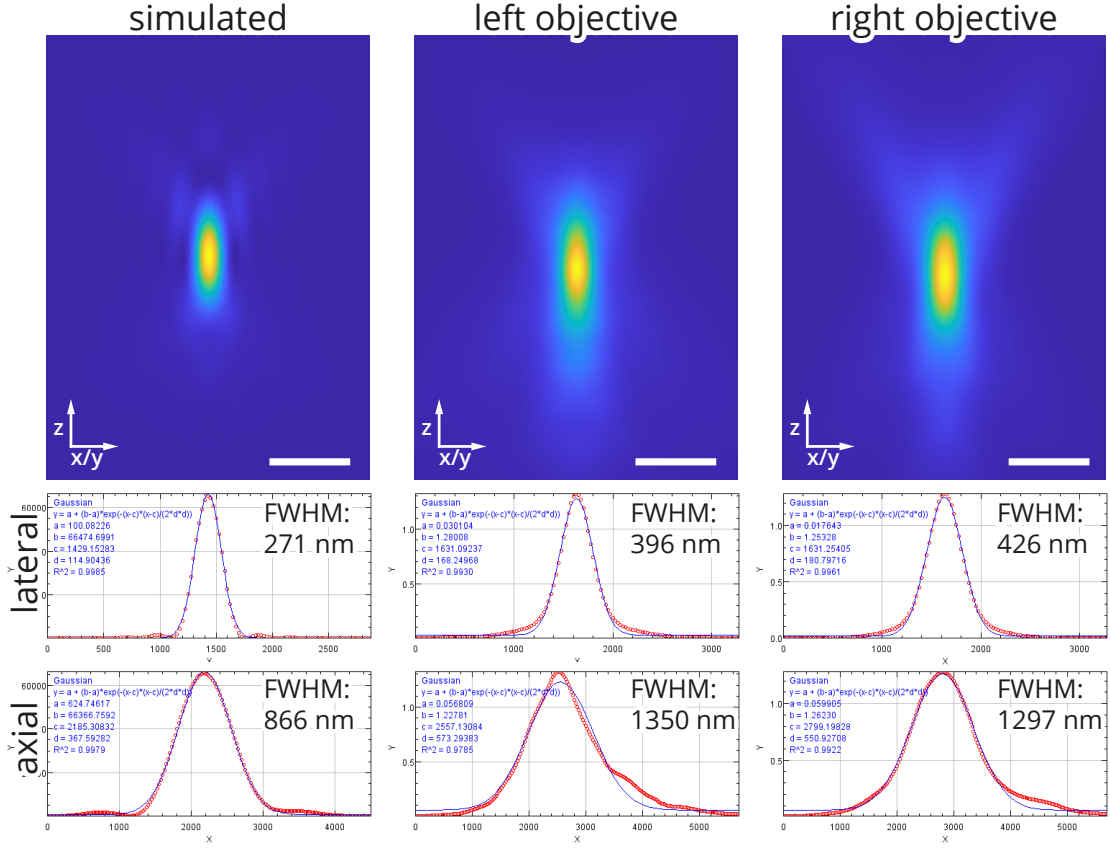


Figure 2.12: Simulated and measured PSF of Dual Mouse-SPIM. Top row: axial sections of simulated and measured point spread functions. Middle row: lateral intensity profile and Gaussian fit. Bottom row: Axial intensity profile and Gaussian fit. Simulations were performed based on the Gibson-Lanni model. Immersion medium and sample refractive index: 1.330, coverslip (FEP foil) refractive index: 1.344, coverslip distance: 1900 μm , coverslip thickness: 50 μm . Excitation wavelength: $\lambda_{ex} = 561 \text{ nm}$. Emission wavelength: $\lambda_{em} = 600 \text{ nm}$. Scale bar: 1 μm .

a diameter of 500 nm) using the DeconvolutionLab2 Fiji plugin [102]. The results of the deconvolution are shown on Figure 2.12. Similarly to the simulation, we measured the axial and lateral resolutions on the experimental PSFs. For the left view, the measured resolutions were 386 nm in the lateral direction, and 1350 nm in the axial direction. For the right view the lateral resolution was 326 nm, and the axial was 1297 nm.

To estimate the achievable multi-view resolution of the system, we combined the two measured PSFs. First, the PSFs were rotated by $\pm 60^\circ$ to correspond to the objective orientations. The PSF images were then normalized by scaling the maximum to 1, and the two rotated and normalized PSFs were multiplied (Figure 2.13). Resolution of the combined PSF is much improved in all directions: along its shortest axis the FWHM is 314 nm, and along the longest axis the FWHM is 496 nm (Figure 2.13). Both are better than the corresponding resolutions for a single view, especially along the long axis, where the FWHM is 2.67 times smaller. This is almost perfectly matching the theoretically expected increase in the axial direction (compare with section 2.1).

2. DUAL MOUSE-SPIM

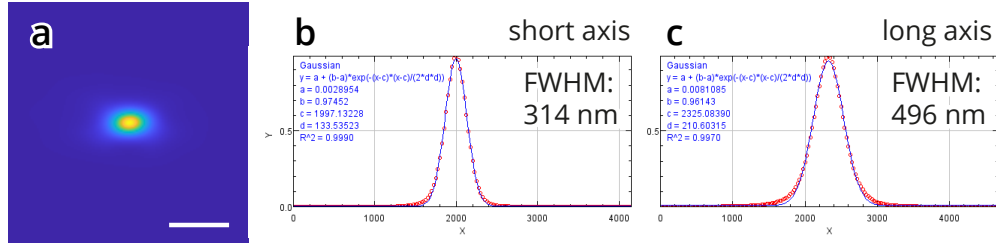


Figure 2.13: Combined PSF of 2 views. (a) The measured PSFs (Figure 2.12) were rotated to their corresponding orientations and multiplied. (b) Gaussian fit along the short axis of the combined PSF; FWHM=314 nm. (c) Gaussian fit along the long axis of the combined PSF; FWHM=496 nm.

4 2.5.4 Resolution inside a *Drosophila melanogaster* embryo

5 Apart from measuring the point spread function and resolution in an ideal bead sample,
6 we also wanted to know the resolution inside a biological sample, as the tissues usually
7 introduce some aberrations to the light path. Although these aberrations highly depend
8 on the sample, as a worst case scenario, we measured the point spread function inside
9 a *Drosophila melanogaster* embryo. As this specimen is highly opaque and scattering, it
10 gives a good estimate for the upper bound of the resolution.

11 Instead of the fluorescent beads, we imaged a *Drosophila* embryo expressing H2A-
12 mCherry marking the nuclei, and ASL-YFP marking the centrosomes (Figure 2.14a, and
13 section 2.6). As the centrosomal protein ASL is diffraction limited in size [103], its image
14 gives a good estimate for the point spread function inside the specimen.

15 Similarly to the bead recordings, 15 centriole images were averaged with the 3D PSF
16 tool of the MOSAIC plugin in Fiji (Figure 2.14c). On the averaged image we measured
17 the resolution by fitting a Gaussian function on the lateral and axial intensity profiles
18 (Figure 2.14d,e), and calculating the FWHM of the fitted Gaussian. The size of the
19 averaged centrioles was 654 nm in the lateral, and 2739 nm in the axial direction.

20 2.5.5 Multi-view imaging of a mouse zygote

21 To demonstrate the multi-view capabilities and improved image quality of the micro-
22 scope, we performed dual-view imaging of a fixed mouse zygote and combined the images
23 using the Multiview Reconstruction [96] plugin of Fiji (Figure 2.15). The microtubules
24 were stained with Alexa Fluor 488, and the zygote was imaged from both views with
25 0.5 μm inter-plane distance.

26 Anisotropy in the resolution becomes apparent in the single-view recordings, when
27 the stacks are resliced from a different direction than the imaging plane. Even though the
28 native view of each objective (Figure 2.15a,d) shows good contrast, and easy to recognize
1 features, when rotated and sliced corresponding to the view of the other objective, the
2 contrast is almost completely gone, and resolution is decreased (Figure 2.15b,e). The
3 fused stack, after the multi-view deconvolution contains the high resolution informa-

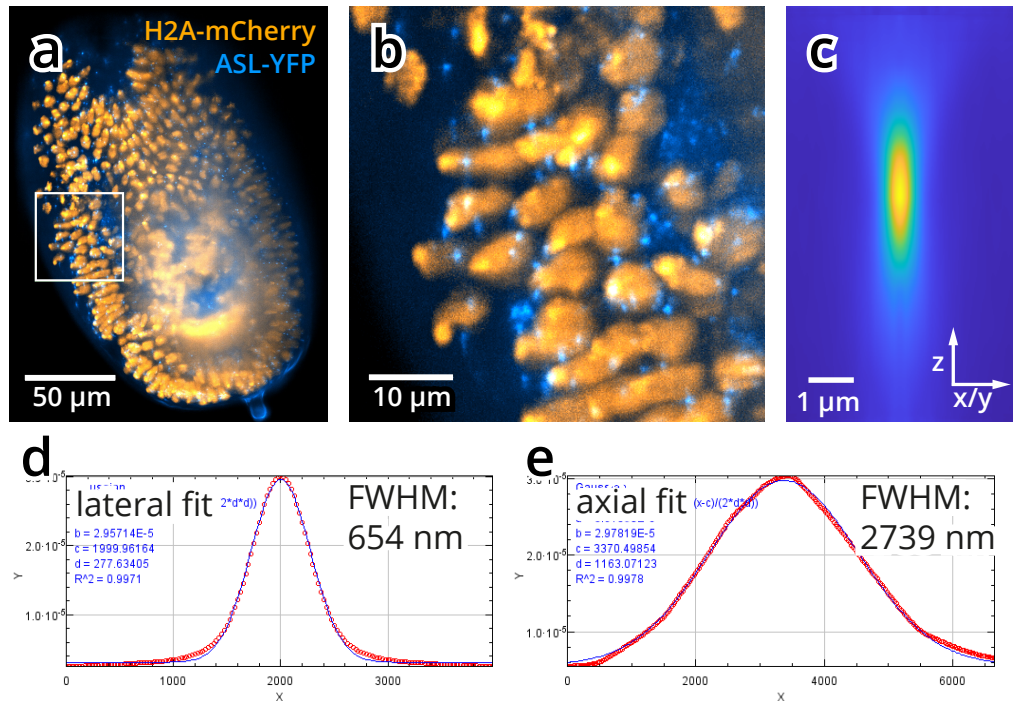


Figure 2.14: Maximum intensity projection of a *Drosophila melanogaster* embryo recording. Maximum intensity projection of a 30 μm thick substack. Orange: nuclei (H2A-mCherry), blue: centrioles (ASL-YFP). 50x magnification. (a) Overview of the embryo. (b) Zoomed in view to the region marked in (a). (c) Average image of 15 centrioles distributed evenly in the embryo. (d) Gaussian fit on the lateral intensity profile of the averaged centrioles; FWHM=654 nm. (e) Gaussian fit on the axial intensity profile of the averaged centrioles; FWHM=2739 nm.

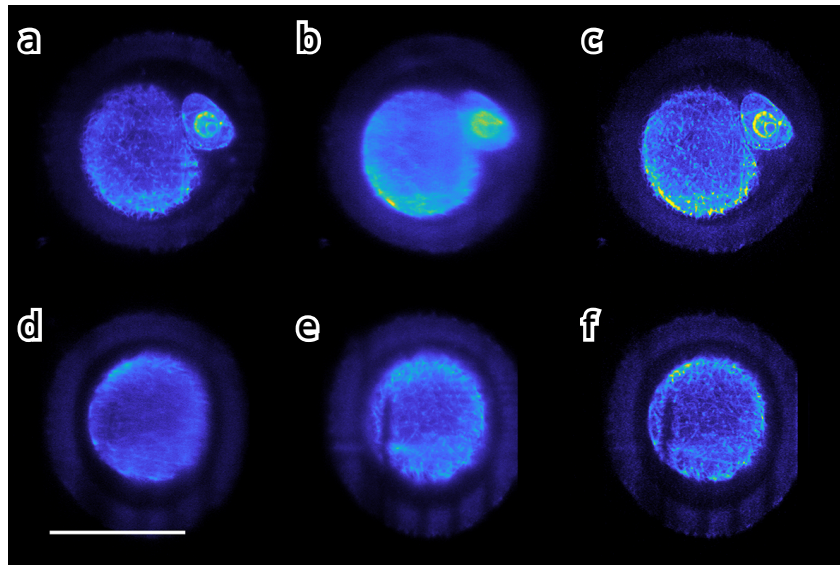


Figure 2.15: Multi-view recording of a mouse zygote. Dual-view imaging was performed on a fixed mouse zygote. Microtubules were stained with Alexa Fluor 488. Top row: view of Left objective. Bottom row: view of Right objective. (a) Raw image from left objective. (b) Rotated view of Right objective. (c) Multi-view deconvolution of stacks (a) and (b). (d) Rotated slice from left objective. (e) Raw image from right objective. (f) Multi-view deconvolution of stacks (d) and (e). Scale bar: 50 μm .

2. DUAL MOUSE-SPIM

⁴ tion form both views, and thus both directions show good quality and high contrast
⁵ (Figure 2.15c,f).

6 2.6 Methods

7 2.6.1 Preparation of fluorescent bead samples

⁸ For registration and resolution measurements we used TetraSpeck 0.5 µm diameter fluo-
⁹ rescently labeled beads (ThermoFisher, T7281). The stock bead solution was thoroughly
¹⁰ vortexed and sonicated for 5 min before diluting it 1:100 in distilled water. The diluted
¹¹ bead solution was stored at 4 °C until use. GelRite (Sigma-Aldrich, G1910) gel was pre-
¹² pared in distilled water at 0.8% concentration with 0.1% MgSO₄ · 7H₂O and kept at
¹³ 70 °C until use. 50 µl of the diluted bead solution was added with a heated pipette tip to
¹⁴ 450 µl of gel solution at 70° to prevent polymerization. The gel was thoroughly vortexed,
¹⁵ and loaded to glass micropipettes (Brand 100 µl). The gel was allowed to cool to room
¹⁶ temperature and stored in a petri dish under dH₂O at 4° until use. For imaging, a small
¹⁷ piece of gel was extruded from the capillary, cut off, and placed in the sample holder.
¹⁸ After positioning the gel to the bottom of the sample holder, the holder was filled with
¹⁹ 200 µl dH₂O.

20 2.6.2 Preparing the sample holder

²¹ The sample holder was lined with 12.5 µm (PSF measurements) or 50 µm (mouse zygote
²² and *Drosophila* embryo imaging) thin FEP foil (Lohmann, RD-FEP050A-610). The FEP
²³ foils were cut to size, washed with 70% ethanol followed by a second wash with dH₂O.
²⁴ After washing, both surfaces of the foils were chemically activated by a 20 s plasma
²⁵ treatment (PlasmaPrep2, Gala Instrumente). The foils were then stored in a petri dish
²⁶ until further use separated by lens cleaning tissues (Whatman, 2105-841). Before imaging,
²⁷ the sample holder was cleaned with dish soap, rinsed with tap water, rinsed with 70%
²⁸ ethanol, and rinsed with dH₂O. The prepared foils were glued to the inside of the cleaned
²⁹ sample holder with medical grade silicon glue (twinsil speed, picodent). During the 5 min
³⁰ curing process the foil was pressed against the sample holder by a custom made press
³¹ fitting the shape of the sample holder. Final dilution of the stock bead solution in the
³² gel is 1:1000.

33 2.6.3 Drosophila embryo imaging

¹ *Drosophila melanogaster* embryos (fly stock AH1) expressing fluorescent nuclear (H2A-
² mCherry) and centriole (ASL-YFP) markers were collected on an agar juice plates and
³ dechorionated in 50% bleach solution for 1 min. After rinsing the bleach with deionized

4 water, the embryos were placed in the sample holder under PBS solution. A small piece of
5 gel containing fluorescent beads were also placed next to the samples to aid in multi-view
6 registration.

7 **2.6.4 Mouse zygote imaging**

8 Fixed mouse zygotes labeled with Alexa-488 (microtubules) and Alexa-647 (kinetochores)
9 were kindly provided by Judith Reichmann. Zygotes were transferred to the sample
10 holder, and imaged in PBS. To allow for multi-view reconstruction, a small piece of gel
11 containing fluorescent beads was placed next to the zygote in the sample holder. Af-
12 ter imaging the zygote from both views, the beads were also recorded using the same
13 stack definitions. After data acquisition, the multi-view datasets were registered and
14 deconvolved in Fiji [100] using the Multiview Reconstruction Plugin [96, 104]. The de-
15 convolution was based on a simulated PSF generated in Fiji with the PSF Generator
16 plugin [105] using the Born-Wolf PSF model [24]. $NA_{ex} = 0.1$, $NA_{em} = 1.1$, $n=1.33$,
17 $\lambda_{ex} = 488 \text{ nm}$, $\lambda_{em} = 510 \text{ nm}$.

18 **2.7 Conclusions**

19 In this chapter we have presented a novel light-sheet microscope designed for subcellular
20 imaging of mouse embryos. The microscope has two identical, high NA (1.1) objectives,
21 positioned in a 120° angle, and operates with a 30° tilted light-sheet. Due to the symmet-
22 rical design both objectives can be used for detection and illumination as well, providing
23 multi-view capabilities without sample rotation.

24 We have characterized the optical properties of the microscope by measuring the light-
25 sheet dimensions (average length: $93 \mu\text{m}$, average thickness: $3.6 \mu\text{m}$), and by measuring
26 the point spread function. When combining the two views, the resolution is much closer
27 to an ideal isotropic shape, being 496 nm along the long axis and 314 nm along the short
28 axis as opposed to 1323 nm and 411 nm measured for a single view. This 2.67 times
29 increase in axial resolution can potentially make the difference in being able to track all
30 chromosomes in a developing mouse embryo.

31 To be able to surpass the proof-of-concept state, the microscope still needs some
32 improvements. The detection view switching unit needs to be improved to minimize
33 field of view drift of both views. Data processing for long term experiments would be
34 extremely challenging otherwise. Another necessity for long term experiments is the
35 implementation of an environmental chamber to provide the appropriate conditions for
1 live embryo imaging.

2 The use of high NA objectives also keep the door open for future upgrades, such
3 as adding structured illumination [55, 56], or coupling in a high power pulsed laser for

2. DUAL MOUSE-SPIM

¹ photomanipulation capabilities [106]. Another natural extension to the system would
² be an addition of a third objective, that would allow for truly isotropic imaging and
³ two-sided sample illumination.

⁴ Chapter 3

⁵ **Image processing for multi-view**
⁶ **microscopy**

⁷ **3.1 Multi-view image fusion**

⁸ **3.1.1 Registration**

⁹ **Image based registration**

¹⁰ **Bead based registration**

¹¹ **3.1.2 Transformation**

¹² **Rigid**

¹³ **Affine**

¹⁴ **Elastic**

¹⁵ **3.1.3 Image fusion**

¹⁶ **Average**

¹⁷ **Sigmoidal weighted average**

¹⁸ **Fourier mixing**

¹⁹ Huisken had something like this

¹ **Wavelet-based fusion**

² **Multi-view deconvolution**

³ [107] Uros thesis [95], [108] Spatially variant deconvolution

3. IMAGE PROCESSING FOR MULTI-VIEW MICROSCOPY

4 3.2 Image compression

5 3.2.1 Entropy coding

6 Information and Entropy

7 "For the purpose of data compression it is useful to quantify the amount of *information*
8 contained within a piece of data. The first rigorous definition of information was presented
9 in an extremely influential paper by Shannon, published in two parts in 1948 [109, 110]."

10 "First, let's define the amount of self-information contained in the outcome of a
11 random experiment:"

$$I(A) = \log_b \frac{1}{P(A)} = -\log_b P(A) \quad (3.1)$$

12 2 independent events:

$$P(A, B) = P(A) \cdot P(B) \quad (3.2)$$

self-information is additive:

$$I(A, B) = \log_b \frac{1}{P(A, B)} \quad (3.3)$$

$$= \log_b \frac{1}{P(A) \cdot P(B)} \quad (3.4)$$

$$= \log_b \frac{1}{P(A)} + \log_b \frac{1}{P(B)} \quad (3.5)$$

13 entropy for random variable X average or expected self-information for the random
14 variable

$$H(X) = \sum_i P(A_i) I(A_i) = -\sum_i P(A_i) \log_b P(A_i) \quad (3.6)$$

15 entropy rate for data source S average information output by the data source

16 Huffman coding

17 Huffman coding is a prefix-free, optimal code that is widely used in data compression. It
18 was developed by David A. Huffman as a course assignment on the first ever course on
19 information theory at MIT, and was published shortly afterwards [111]. It is a variable
20 length binary code which assigns different length codewords to letters of different prob-
21 abilities. It is able to achieve optimal compression, which means the total length of the
22 coded sequence will be minimal.

23 Although it produces a variable length code which can introduce some issues with
1 decoding, it is still uniquely decodable. It achieves this property by using prefix-free
2 codewords, meaning that none of the codewords are prefixes of any other codewords.
3 This property can be exploited when decoding the codeword, since during this procedure

Table 3.1: Examples of a random binary code (#1) and a prefix-free binary code (#2). Code #2 is uniquely decodable, while for code #1 it's necessary to introduce boundaries between codewords to be able to distinguish them.

Letter	Code #1	Code #2
a_1	0	10
a_2	11	11
a_3	00	00
a_4	10	010
a_5	111	011

4 the number of bits for the next codeword can not be determined in advance. However if
5 no codeword is a prefix of another codeword, by simply reading the successive bits one
6 by one until we reach a valid codeword, it's possible to uniquely decode the message.

7 Let's take the example in Table 3.2. Five letters are coded in binary code by Code
8 #1 and by Code #2. Code 1 is not a prefix code, and because of this when reading the
9 encoded sequence we can not be sure when we reach the end of a codeword. Decoding
10 the sequence 0000 for example could be interpreted as 4 letters of a_1 or 2 letters of a_3 .

11 The Huffman coding procedure is based on two observations regarding optimal and
12 prefix-free codes:

- 13 1. For a letter with higher frequency the code should produce shorter codewords, and
14 for letters with lower frequency it should produce longer codewords.
- 15 2. In an optimum code, the two least frequent codewords should have the same
16 lengths.

17 From these statements the first is trivial to see that is correct. If the more frequent
18 letters would have longer codewords than the less frequent letters, the average codeword
19 length (weighted by the probabilities) would be larger than in the opposite case. Thus,
20 more frequent letters must not have longer codewords than less frequent letter.

21 The second statement at first glance might not be so intuitive, so let's consider the
22 following situation. The two least frequent codewords do not have the same lengths, that
23 is the least frequent is longer. However, because this is a prefix code, the second longest
24 codeword is not a prefix of the longest codeword. This means, if we truncate the longest
25 codeword to the same length as the second longest, they will still be distinct codes and
1 uniquely decodable. This way we have a new coding scheme which requires less space on
2 average to code the same sequence as the original code, from which we can conclude the
3 original code was not optimal. Therefore, for an optimal code, statement 2 must be true.

To construct such a code, the following iterative procedure can be used. Let's consider an alphabet with five letters $A = [a_1, a_2, a_3, a_4, a_5]$ with $P(a_1) = P(a_3) = 0.2$, $P(a_2) = 0.4$ and $P(a_4) = P(a_5) = 0.1$ (Table 3.2). "The entropy for this source is 2.122 bits/symbol." Let's order the letters by probability, and consider the two least frequent.

3. IMAGE PROCESSING FOR MULTI-VIEW MICROSCOPY

Table 3.2: Huffman code table.

Letter	Probability	Codeword
a_2	0.4	$c(a_2)$
a_1	0.2	$c(a_2)$
a_3	0.2	$c(a_2)$
a_4	0.1	$c(a_2)$
a_5	0.1	$c(a_2)$

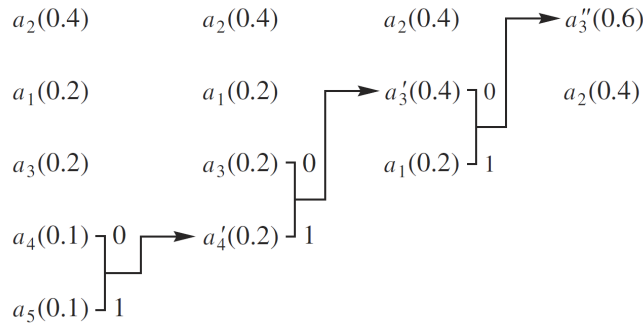


Figure 3.1: Building the binary Huffman tree. The letters are ordered by probability, these will be the final leave of the tree. To join the two branches at every iteration we join the two nodes with the smallest probability, and create a new common node with the sum of the probabilities. This process is continued until all nodes are joined in a root node with probability of 1. Now, if we traverse down the tree to each leaf, the codeword will be defined by their position.

Since the codewords assigned to these should have the same lengths, "we can assign their codewords as"

$$\begin{aligned} c(a_4) &= \alpha_1 * 0 \\ c(a_5) &= \alpha_1 * 1 \end{aligned}$$

where $c(a_i)$ is the assigned codeword for letter a_i and $*$ denotes concatenation. Now we define a new alphabet A' with only four letters a_1, a_2, a_3, a'_4 , where a'_4 is a merged letter for a_4 and a_5 with the probability $P(a'_4) = P(a_4) + P(a_5) = 0.2$. We can continue this process of merging the letters until all of them are merged and we have only one letter left. Since this contains all of the original letters, its probability is 1. We can represent the end result in a binary tree (see Figure 3.1), where the leaves are the letter of the alphabet, nodes are the merged letters, and the codewords are represented by the path from the root node to each leaf (compare with Table 3.3). "The average length of this code is"

$$l = 0.4 \times 1 + 0.2 \times 2 + 0.2 \times 3 + 0.1 \times 4 + 0.1 \times 4 = 2.2 \text{ bits/symbol} \quad (3.7)$$

"A measure of the efficiency of this code is its redundancy—the difference between the

Table 3.3: Huffman code table.

Letter	Probability	Codeword
a_2	0.4	1
a_1	0.2	01
a_3	0.2	000
a_4	0.1	0010
a_5	0.1	0011

⁴ entropy and the average length. In this case, the redundancy is 0.078 bits/symbol. The
⁵ redundancy is zero when the probabilities are negative powers of two.”

⁶ JPEG [112], JPEG-LS [113] and JPEG2000 [114]

⁷ **3.2.2 Differential pulse code modulation / LOCO-I?**

⁸ **3.3 Noise in light microscopy images**

⁹ **3.3.1 Photon shot noise**

¹⁰ **3.3.2 Camera noise**

¹¹ **CCD**

¹ **EM-CCD**

² **sCMOS**

³ **3.3.3 Variance stabilization**

3. IMAGE PROCESSING FOR MULTI-VIEW MICROSCOPY

⁴ Chapter 4

⁵ Real-time, GPU accelerated
⁶ image processing pipeline

⁷ 4.1 Challenges in data handling for light-sheet microscopy

⁸ When using any kind of microscopy in research, image processing is a crucial part of
⁹ the workflow. This is especially true for light-sheet microscopy, since it is capable of
¹⁰ imaging the same specimen for multiple days, producing immense amounts of data. A
¹¹ single overnight experiment of *Drosophila* development (which is a very typical use-case
¹² for light-sheet) can produce multiple terabytes of data.

¹³ Apart from light-sheet microscopy, many other microscopy modalities are also suf-
¹⁴ fering from this problem. Methods, such as high content screening [115–117], where tens
¹⁵ of thousands of different genotypes are imaged generating millions of images; and single
¹⁶ molecule localization microscope (SMLM) [118–120], where just a single plane of a single
¹⁷ sample is imaged hundreds of thousands of times to acquire super-resolved images.

¹⁸ Not only these methods are capable of generating data extremely fast, but with
¹⁹ the sustained high data rate a single experiment can easily reach multiples of terabytes
²⁰ (Figure 4.1). Handling this amount of data can quickly become the bottleneck for many
²¹ discoveries, which is a more and more common issue in biological research [121–123].

²² This chapter will focus on addressing these challenges, by presenting a real-time,
²³ GPU-based image preprocessing pipeline consisting of two parts (Figure 4.2). The first
²⁴ part is a fast image fusion method for our workhorse light-sheet microscope, the MuVi-
²⁵ SPIM [45], that enables live fusion of the images arriving from two opposing cameras.
¹ The second part of the pipeline, which can also be used in a standalone way, is a real-time
² image compression library that allows lossless and within noise level compression of the
³ data already during acquisition.

4. REAL-TIME, GPU ACCELERATED IMAGE PROCESSING PIPELINE

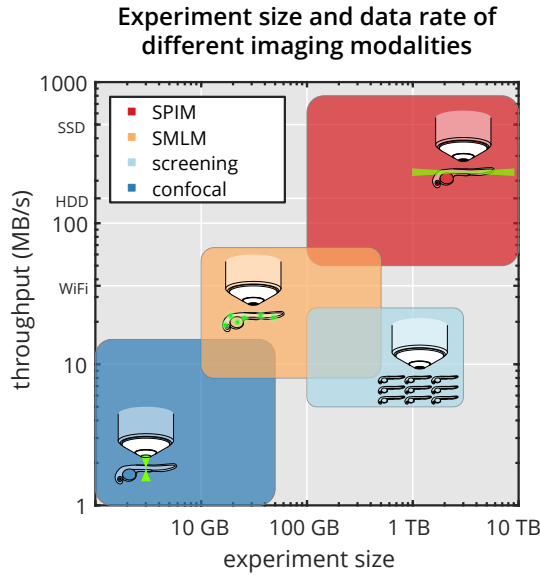


Figure 4.1: Experiment sizes and data rate of different imaging modalities. Comparison of single-plane illumination microscopy (SPIM, red rectangle), high-content screening (light blue), single molecule localization microscopy (SMLM, orange) and confocal microscopy (blue) by typical experiment size and data production rate (see also Table B1).

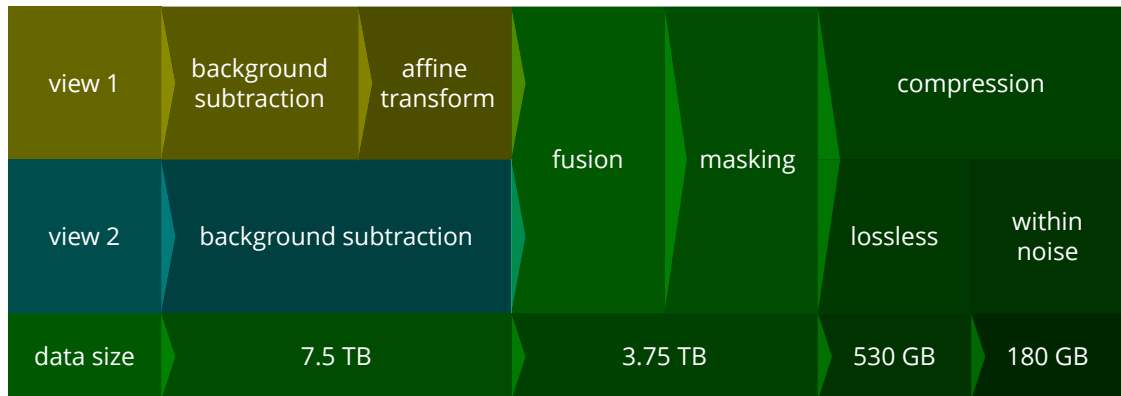


Figure 4.2: Real-time image processing pipeline for multi-view light-sheet microscopy.

4.1.1 CUDA architecture

5 CUDA [124] CUDA programming Guide [125]

4.2 Live fusion

7 Similarly to the DualMouse-SPIM, our currently used production microscope, the
8 Multiview-SPIM (MuVi-SPIM) [45] also uses multiple imaging directions to improve
1 the image quality. In this case, however, the aim is completeness rather than increasing
2 the resolution. As the MuVi-SPIM is capable of imaging much larger specimens, such as
3 entire *Drosophila* embryos, the sample size itself can present some challenges, especially

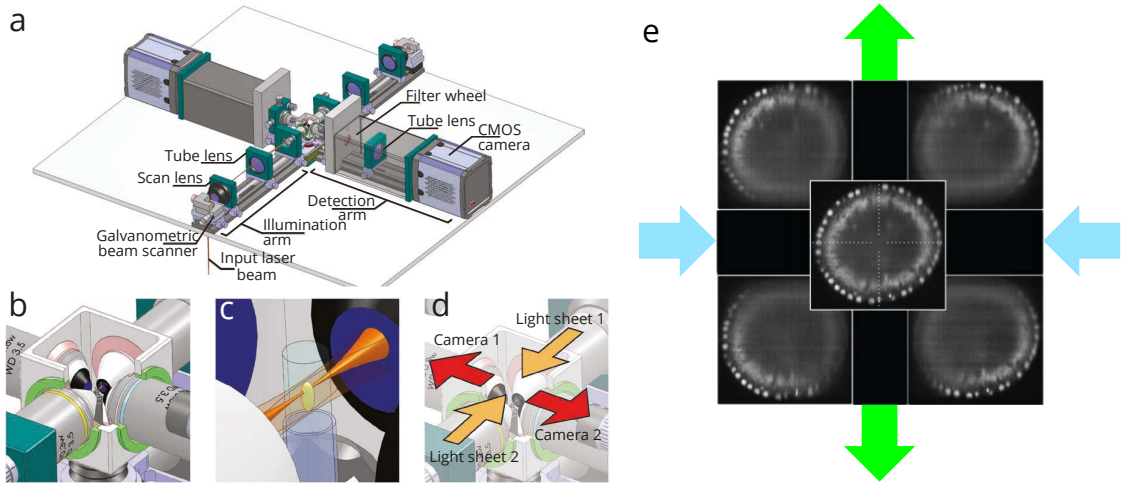


Figure 4.3: Operating principle of MuVi-SPIM. (a) The microscope consists of two illumination and two detection arms for simultaneous multi-view illumination and detection. (b) The 4 arms meet in the imaging chamber that is filled with water, and contains the sample. (c) The sample is held by a glass capillary, in a GelRite cylinder. Optical sectioning is achieved by a virtual light-sheet. (d) The light-sheets can be generated from two sides (Light sheet 1 and 2), and detection is also double sided (Camera 1 and 2). Adapted from [45].

for opaques specimens. As light scattering and absorption impacts both the illumination and detection optics, the negative effects for SPIM are more pronounced compared to single-lens systems [126].

4.2.1 Multiview SPIM for *in toto* imaging

MuVi-SPIM provides an elegant solution for multi-view imaging. A standard SPIM setup with a single detection and a single illumination lens would rotate the sample to acquire images from multiple directions. MuVi-SPIM, on the other hand, utilizes two opposing objectives for illumination, and two opposing objectives for detection (Figure 4.3a). As the sample is held by an aqueous gel inside the imaging chamber, all objectives have unobstructed view of it from multiple directions (Figure 4.3b,c).

Data acquisition is done in two steps: the sample is illuminated by Light sheet 1, and fluorescence is collected by both detection objectives at the same time, after which Light sheet 2 is activated, and both cameras record the fluorescence again (Figure 4.3d). This process will result in 4 datasets, all with partial information due to scattering effects. The 4 views are later fused to a single, high quality dataset (Figure 4.3e). This fusion process is necessary before any further analysis steps can be performed, however, due to the sheer size of the data, it takes a considerable amount of time after the acquisition.

By combining scanned light-sheet [49] with confocal slit detection on the camera chip [127], it is possible to exclude out of focus, scattered illumination light. This way it is possible to illuminate simultaneously with both light-sheets, which leaves us with only two views, the views of the two opposing cameras [75].

4. REAL-TIME, GPU ACCELERATED IMAGE PROCESSING PIPELINE

4.2.2 Image registration

To perform image fusion of multiple views, first image registration is necessary: the coordinate systems of both views have to be properly overlapped. Ideally a single mirroring transformation would be enough to superpose the two camera images, however in practice the microscope can never be aligned with such precision. Other types of transformations are also necessary: translation to account for offsets in the field of view; scaling in case of slightly different magnifications; and also shearing if the detection plane is not perfectly perpendicular to the sample movement direction [107]. To combine all of these effects, a full, 3D affine transformation is necessary to properly align the two camera images (Fig. 4.4 a). This transformation can be represented by a matrix multiplication with 12 different parameters:

$$\begin{pmatrix} a & b & c & d \\ e & f & g & h \\ i & j & k & l \\ 0 & 0 & 0 & 1 \end{pmatrix} \times \begin{pmatrix} x \\ y \\ z \\ 1 \end{pmatrix} = \begin{pmatrix} ax + by + cz + d \\ ex + fy + gz + h \\ ix + jy + kz + l \\ 1 \end{pmatrix}$$

where x, y, z are the coordinates of the original 3D image, and a, b, \dots, l are the affine transformation parameters.

These parameters are traditionally acquired by a bead based registration algorithm after imaging fluorescent beads from each view of the microscope [104, 128]. The beads are segmented by using a difference of Gaussian filter, and the registration parameters are acquired by matching the segmented bead coordinates in each view. Identifying the corresponding beads in each view is done by a translation and rotation invariant local geometric descriptor. This matches the beads based on their relative position to their nearest neighbors. After the matching beads are identified, the affine transformation parameters are calculated by minimizing the global displacement for each pair of beads.

For the two opposing views of MuVi-SPIM, these parameters are only dependent on the optical setup itself, and not the sample or the experiment. Because of this, it is sufficient to determine the transformation parameters only after modifying the microscope (*e.g.* after realignment).

In our previous fusion pipeline, after the parameters were acquired, the 3D stacks are fused by transforming one of the views to the coordinate system of the other (using the affine transformation parameters from the bead based registration), and fusing the two stack by applying a sigmoidal weighted average. The weights are determined in a way to exclude the parts of a stack that has worse image quality, and complement is from the other view. When using the electronic confocal slit detection (eCSD) weighting is not necessary, as the scattered light is already rejected in these recordings, and a simple sum of the two stacks gives the best results regardless of the sample [75].

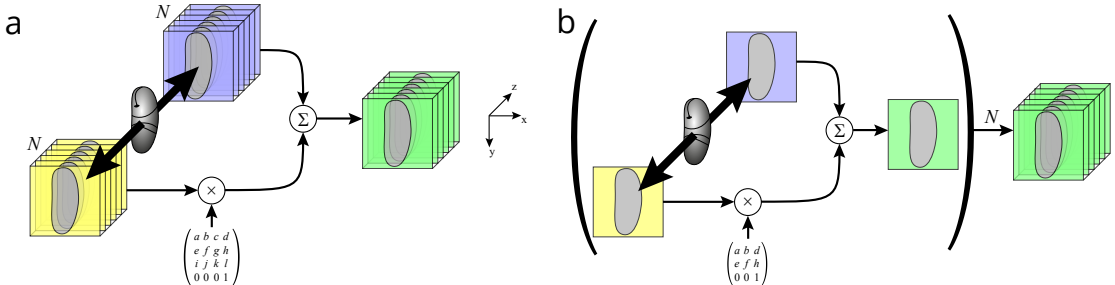


Figure 4.4: Multi-view fusion methods for light-sheet microscopy. a) Full 3D stacks are acquired from the opposing views (yellow and blue), which are then registered in 3D space using previously acquired affine transformation parameters. Registered stacks are then weighted averaged to create the final fused stack (green). b) Images from opposing views are directly fused plane by plane. Registration takes place in 2D space thus reducing computational effort and memory requirements. The registered planes are then weighted averaged to create the final fused image.

3 The fusion process itself, however can be very resource intensive, and take a considerable amount of time. This is simply due to the size of the 3D stacks: a single stack is 5 usually between 2 and 4 GB in size. Thus, the necessary memory requirement to fuse 2 of these stacks is $3 \cdot 4 \text{ GB} = 12 \text{ GB}$, as the result will also take up the same space. Just 7 reading and writing this amount of information to the hard disk takes a considerable 8 amount of time. When using an SSD drive for example, with a 500 MB/s read/write 9 speed, just the I/O operations will take around $\frac{12 \text{ GB}}{500 \text{ MB/s}} = 24 \text{ s}$.

10 It would be much more practical to already fuse the opposing views before displaying 11 or saving the image. Since the two cameras ideally image the same z plane, it should be 12 possible to reduce the alignment problem to a 2D affine transformation:

$$\begin{pmatrix} a & b & d \\ e & f & h \\ 0 & 0 & 1 \end{pmatrix} \times \begin{pmatrix} x \\ y \\ 1 \end{pmatrix} = \begin{pmatrix} ax + by + d \\ ex + fy + g \\ 1 \end{pmatrix}$$

If this is possible, then fusion can be carried out separately for each image plane (Fig. 4.4 b), which would greatly facilitate live image fusion. The requirements for this are the following:

$$|cz| < \sigma_{xy} \quad \forall z \quad (4.1)$$

$$|gz| < \sigma_{xy} \quad \forall z \quad (4.2)$$

$$|ix + jy + (k - 1)z + l| < \sigma_z \quad \forall x, y, z \quad (4.3)$$

13 where σ_{xy} is the lateral resolution, and σ_z is the axial resolution of the microscope, which 14 are 277 nm and 1099 nm respectively.

1 If these conditions hold (*i.e.* the microscope is properly aligned), then direct plane 2 by plane fusion will not result in any loss of information compared to the full 3D image

4. REAL-TIME, GPU ACCELERATED IMAGE PROCESSING PIPELINE

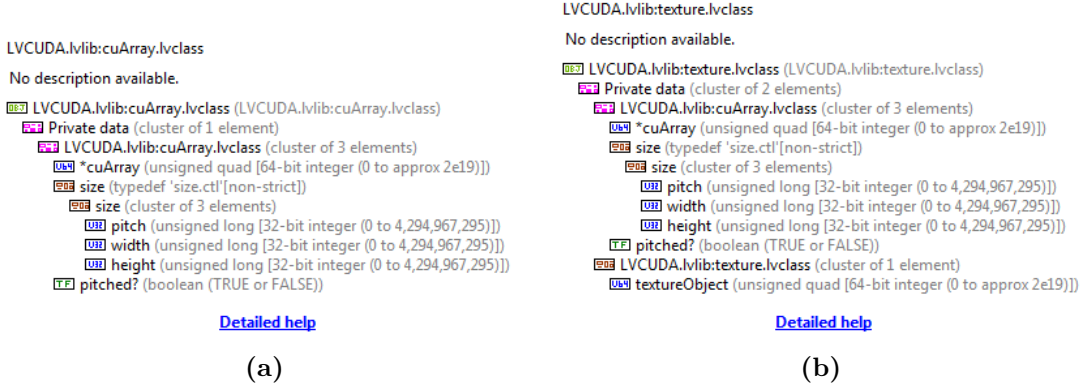


Figure 4.5: Classes of LVCUDA library. (a) **CuArray** class, wrapping a 1D or 2D pitched device memory for use in LabVIEW. (b) **Texture** class, wrapping a CUDA texture object for use in LabVIEW.

3 fusion.

4 4.2.3 CUDA implementation of direct fusion

5 As our custom microscope control software (subsection 2.4.2) is implemented in Lab-
 6 VIEW, we implemented the pipeline as a combination of a CUDA and a LabVIEW
 7 library. The CUDA library implements all the necessary low level functions, and exposes
 8 these in a dynamically linked library (dll). The LabVIEW library, **LVCUDA.lvlib** imple-
 9 ments two high level classes: **cuArray**, and **Texture** (Figure 4.5). These interface to the
 10 CUDA dll, and allow to easily build a flexible CUDA-based image processing pipeline in
 11 LabVIEW.

12 **cuArray** LabVIEW class

13 **Texture** LabVIEW class

14 4.2.4 Results

15 The image preprocessing pipeline was tested on our previously described Multi-View
 16 Single Plane Illumination Microscope (MuVi-SPIM)[45]. For the background subtraction
 17 we recorded 1500 dark images with each camera and averaged them, to obtain the camera
 18 specific background images. Before image acquisition these were uploaded to the GPU
 19 memory, and were readily available for the pipeline.

20 After careful alignment of the microscope to meet the previously discussed require-
 21 ments (Eqs. (4.1) – (4.3)), we imaged fluorescent beads in a gel suspension to obtain
 22 the affine transformation parameters. After making sure that these parameters indeed
 23 fulfill the previously set requirements, these were also uploaded to the GPU memory for
 24 further use in our pipeline.

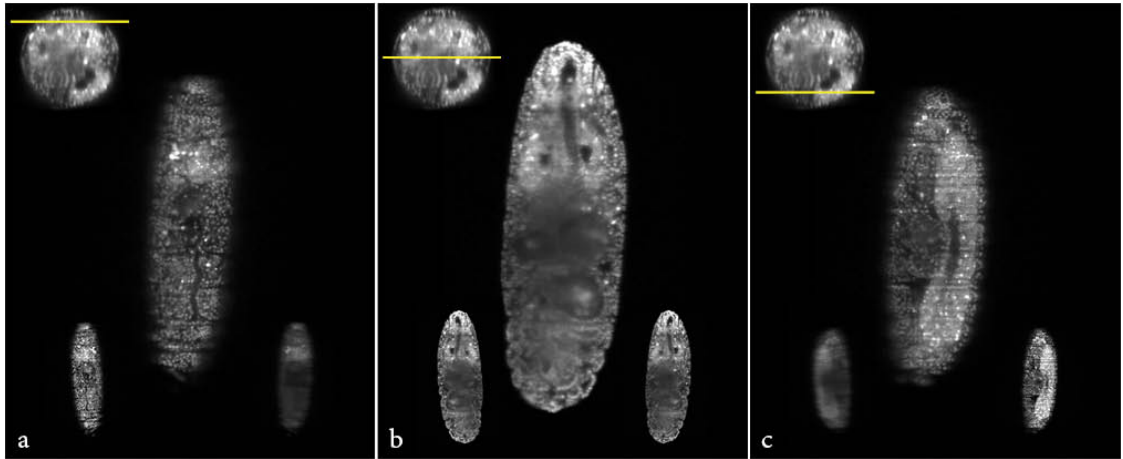


Figure 4.6: GPU fused images of a *Drosophila melanogaster* embryo. Two stacks were taken in quick succession first without fusion, then with fusion enabled. Fused images are shown in the middle of each subfigure, while the individual camera images are in the bottom insets. The top-left inset depicts the z-position of the shown images. a) Image from closer to the left camera. b) Image from the center of the embryo. c) Image from closer to the right camera.

1 To validate our hypotheses, that 2D direct image fusion is sufficient instead of the
 2 full 3D fusion, we image several samples. First, we imaged the fluorescent beads again,
 3 now with the live fusion enabled, to make sure our registration parameters are correct.
 4 Manual evaluation of the data revealed that the fusion indeed worked, without any
 5 artifacts, such as double beads which would indicate an imprecision in alignment or in
 6 the transformation parameters.

7 We also applied the live fusion to a real biological specimen, namely *Drosophila*
 8 *melanogaster* embryos expressing H2Av-mCherry histone marker. The embryos were im-
 9 aged first without direct fusion enabled, and immediately afterwards with direct fusion
 10 enabled (Fig. 4.6). Image quality dependency on the depth of the imaging plane is es-
 11 pecially apparent in single-view stacks. Planes closer to the camera give a sharp, high
 12 contrast image, while planes further than the middle of the embryo are severely degraded
 13 due to scattering.

14 Stacks obtained with the live fusion enabled show a consistently high image qual-
 15 ity throughout the entire stack, independent of the depth. This allows us to keep only
 16 the already fused data, thus effectively reducing the storage requirement by half, and
 17 facilitating further data processing steps.

18 4.3 B³D image compression

19 The second part of our GPU-based image preprocessing pipeline is a new image com-
 20 pression algorithm that allows for extremely fast image compression to efficiently reduce
 21 data sizes already during acquisition.

4. REAL-TIME, GPU ACCELERATED IMAGE PROCESSING PIPELINE

1 A straightforward solution to these problems would be to compress the images during acquisition. Although this would not reduce the requirements for image processing power and time, it still has a big impact on the necessary background infrastructure.
2 By reducing the data size, not only the cost for storage can be reduced, but the time it takes to transfer the data during the various steps of data processing. A fast compression method would also greatly improve 3D data browsing possibilities, as more data could be piped to the rendering software.

3 Despite these advantages, not many microscopists have implemented real time compression strategies during acquisition, and this is mostly due to the lack of appropriate compression methods suitable for scientific imaging that also offers the high throughput demanded by these applications. Typically used lossless compression methods, such as JPEG2000 [114] although offer good compression ratios, are very slow in processing speed, at least compared to the data rate of a modern microscope ($\sim 1 \text{ GB/s}$). High speed compression methods that could deal with this data rate have been developed for ultra high definition 4K and 8K digital cameras, such as the high efficiency video codec (HEVC) [129]. These methods, however, have been optimized for lossy image compression which is generally not acceptable for scientific data [130], and rarely support compression of high bit rate originals, which is typically the case for modern sCMOS sensors. Although the HEVC recommendation does specify bit rates up to 16 bits, and lossless compression, we

4 To address these issues, we developed B³D, a GPU based image compression method that is capable of high speed compression of microscopy images during the image acquisition process. By utilizing the massively parallel processing architecture of a GPU, we were not only able to reach a compression and decompression speed of 1 GB/s, but our algorithm also keeps the load off the CPU, making it available for other computing tasks related to operating the microscope itself.

5 A second feature of our compression library is a novel algorithm for noise dependent lossy compression of scientific images. As mentioned before, lossy compression is not recommended for scientific images, and the reason for this, is all practical lossy compression algorithms are designed with the intent of fooling the human visual system [131]. While the images compressed by these algorithms may appear identical to the eye, any downstream data analysis could be negatively impacted by the compression artifacts. To our knowledge, only a single algorithm allows to set the loss in a deterministic manner: the near-lossless operating mode of JPEG-LS [113]. In this mode it is possible to set the maximum allowable error a pixel can have after decompression. Although this can be useful for certain applications, it has not been widely implemented, as the visual quality loss is more severe compared to other algorithms with the same compression ratio [132].

6 B³D image compression light-sheet (Sec. 1.3) data handling is bottleneck

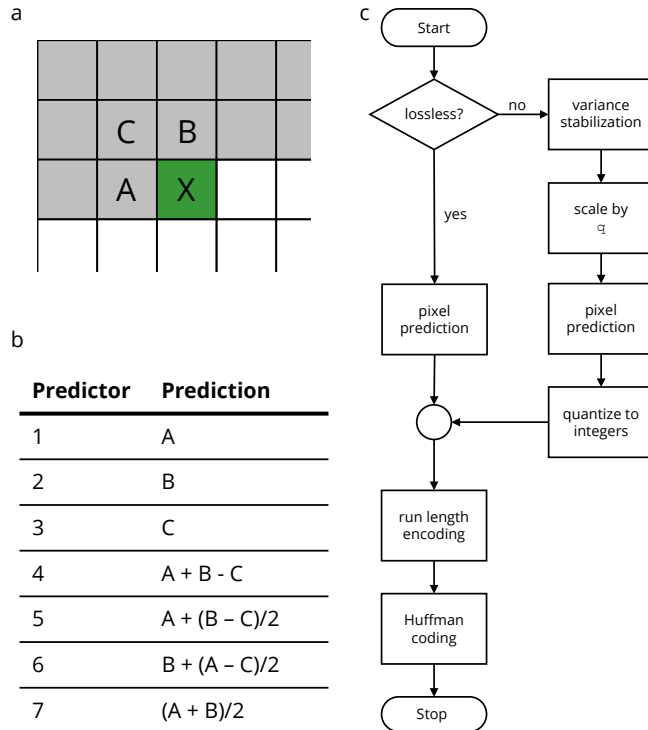


Figure 4.7: B³D algorithm schematics. (a) Prediction context for pixel X, the next sample to be encoded. Three neighboring pixels are considered: left (A), top (B) and top left (C) neighbors. (b) Lossless JPEG predictors for X, based on the context showed in (a). The first three predictors are one-dimensional, while the rest are two-dimensional. Using a two dimensional predictor while increases complexity slightly, also increases the achievable compression ratio. We found that for fluorescence microscopy images predictor 7 performs best, hence its inclusion in the B³D algorithm. (c) Complete algorithm flowchart depicting the main stages of the compression. First, if the result should be lossless, pixel prediction is performed on the original image values. If within noise level mode is selected, the image noise is stabilized first (see “Supplementary Note”), which is then scaled by the quantization step q. Prediction is performed, and the prediction errors are rounded to the nearest integer. The prediction errors for both lossless and lossy modes are then run-length encoded, and finally Huffman coding is applied to effectively reduce data size. The output of the Huffman coder is saved as the compressed file.

1 KLB [133]

2 big data viewer [134] Fiji [100]

3 FLIC [135] SFALIC [136] FELICS [137] -> this was before JPEG-LS Treib terrain
4 editing [138] Treib turbulence [139]

5 4.3.1 Compression algorithm

6 compression scheme: modeling+ coding [140]

4. REAL-TIME, GPU ACCELERATED IMAGE PROCESSING PIPELINE

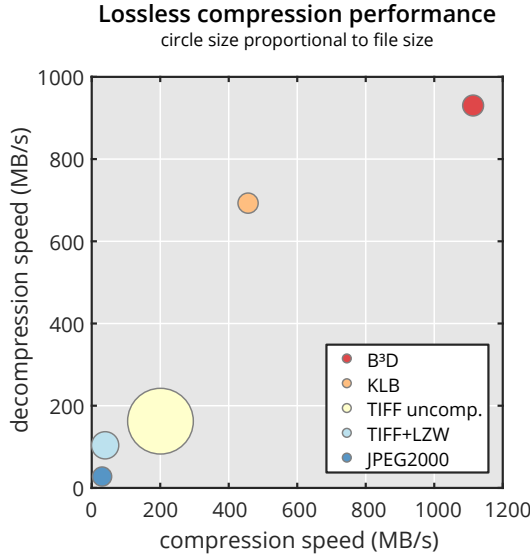


Figure 4.8: Lossless compression performance. Performance comparison of our B³D compression algorithm (red circle) vs. KLB (orange), uncompressed TIFF (light yellow), LZW compressed TIFF (light blue) and JPEG2000 (blue) regarding write speed (horizontal axis), read speed (vertical axis) and file size (circle size). (see also Table B2).

¹ **4.3.2 Benchmarking**

² **4.4 Noise dependent lossy compression**

³ square root compression [141] noise and bias in square root compression [142] quantiza-
⁴ tion [143] Anscombe [144] optimal inverse Anscombe [145, 146] optimal inverse general-
⁵ ized Anscombe [147]

⁶ **4.5 Methods**

⁷ **Compression benchmarking**

⁸ For all presented benchmarks, TIFF and JPEG2000 performance was measured through
⁹ MATLAB's imwrite and imread functions, while KLB and B³D performance was mea-
¹⁰ sured in C++. All benchmarks were run on a computer featuring 32 processing cores
¹¹ (2×Intel Xeon E5-2620 v4), 128 GB RAM and an NVIDIA GeForce GTX 970 graphics
¹² processing unit. Read and write measurements were performed in RAM to minimize I/O
¹³ overhead, and are an average of 5 runs.

¹⁴ **Light-sheet imaging**

¹⁵ *Drosophila* embryos were imaged in our MuVi-SPIM setup [45] using the electronic con-
¹⁶ focal slit detection (eCSD) [75]. Embryos were collected on an agar juice plate, and

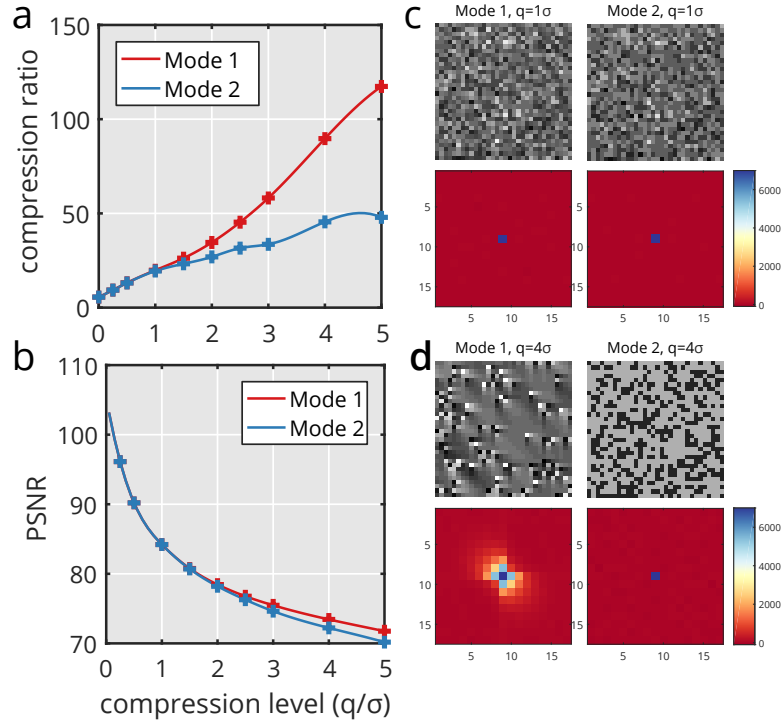


Figure 4.9: Options for noise dependent lossy compression. Comparing Mode 1 (prediction then quantization) and Mode 2 (quantization then prediction) of noise dependent lossy compression in terms of compression ratio, peak signal to noise ratio (PSNR) and spatial correlations introduced to random noise. (a) Compression ratio as a function of the quantization step for Mode 1 and Mode 2. (b) PSNR as a function of the quantization step for Mode 1 and Mode 2. (c, d) Random noise was compressed at various quantization steps both for Mode 1 and Mode 2. Autocorrelation was calculated for the compressed images to see whether the compression introduces any spatial correlation between the pixels. For $q=1\sigma$ both modes are free of correlation (c, top: compressed images, bottom: autocorrelation), however, for $q=2\sigma$ Mode 1 exhibits a correlation pattern (d, top left: compressed image, bottom left: autocorrelation) that is not present in Mode 2 (d, top right compressed image, bottom right: autocorrelation). For more discussion, see "Supplementary Note".

17 dechorionated in 50% bleach solution for 1 min. The embryos were then mounted in a
 18 shortened glass capillary (Brand 100 μ l) filled with 0.8% GelRite (Sigma-Aldrich), and
 1 pushed out of the capillary to be supported only by the gel.

2 3D nucleus segmentation

3 3D nucleus segmentation of *Drosophila* embryos was performed using Ilastik [148]. The
 4 original dataset was compressed at different quantization levels, then upscaled in z to ob-
 5 tain isotropic resolution. To identify the nuclei, we used the pixel classification workflow,
 6 and trained it on the uncompressed dataset. This training was then used to segment the
 7 compressed datasets as well. Segmentation overlap was calculated in Matlab ("Supple-
 8 mentary Code") using the Sørensen–Dice index [149, 150]:

$$QS = 2 |A \cap B| / (|A| + |B|) \quad (4.4)$$

4. REAL-TIME, GPU ACCELERATED IMAGE PROCESSING PIPELINE

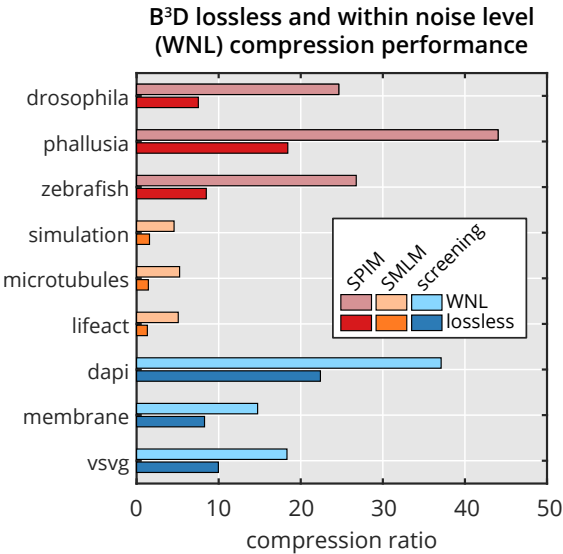


Figure 4.10: Within noise level compression performance. WNL compression performance compared with lossless performance for 9 different dataset representing 3 imaging modalities (SPIM, SMLM, screening). Compression ratio = original size / compressed size. For description of datasets see Table B3 in Appendix B.

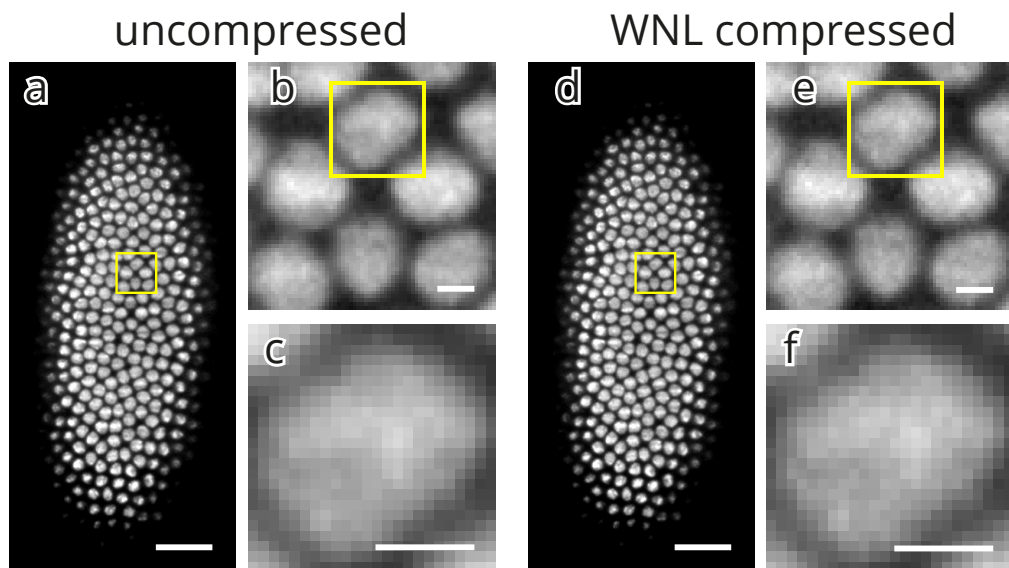


Figure 4.11: Image quality of a WNL compressed dataset. WNL compression performance compared with lossless performance for 9 different dataset representing 3 imaging modalities (SPIM, SMLM, screening). Compression ratio = original size / compressed size. For description of datasets see Table B3.

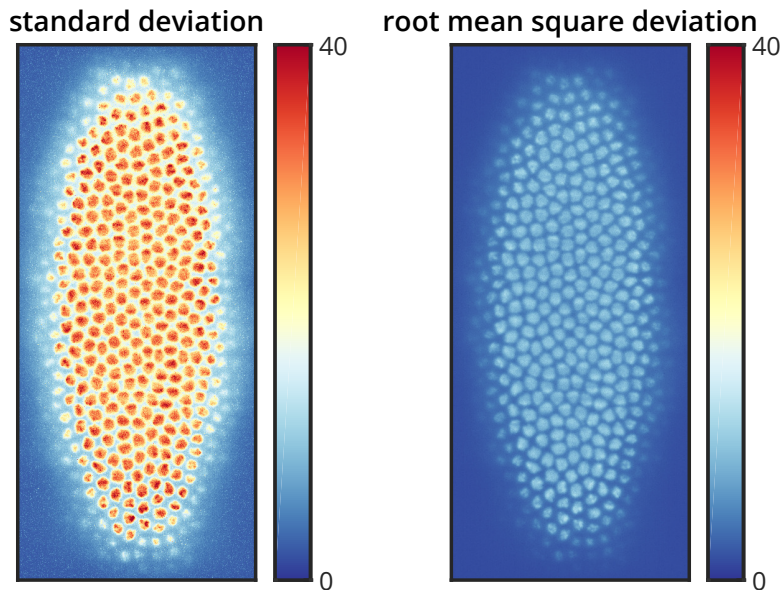


Figure 4.12: Compression error compared to image noise. To compare the difference arising from WNL compression to image noise, we imaged a single plane 100 times in a *Drosophila melanogaster* embryo expressing H2Av-mCherry nuclear marker at 38 ms intervals. The whole acquisition took 3.8 s, for which the sample can be considered stationary. To visualize image noise, the standard deviation was calculated for the uncompressed images (left). All images were then WNL compressed, and the root mean square deviation was calculated compared to the uncompressed images (right). The root mean square deviation on average is 3.18 times smaller than the standard deviation of the uncompressed images.

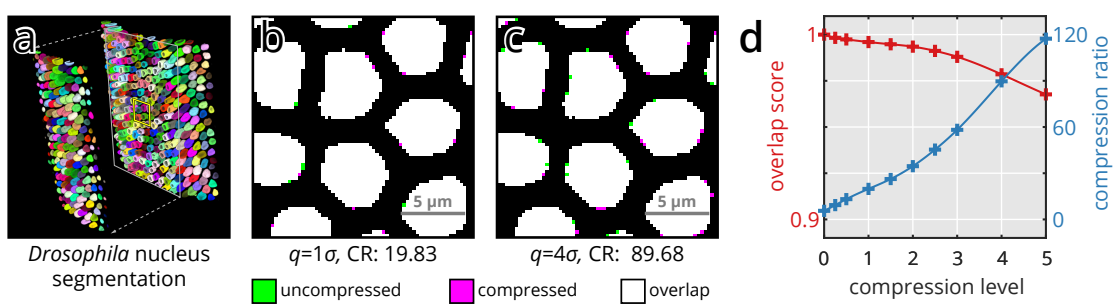


Figure 4.13: Influence of noise dependent lossy compression on 3D nucleus segmentation. A *Drosophila melanogaster* embryo expressing H2Av-mCherry nuclear marker was imaged in MuVi-SPIM [45], and 3D nucleus segmentation was performed ("Online Methods") (a). The raw data was subsequently compressed at increasingly higher compression levels, and segmented based on the training of the uncompressed data. To visualize segmentation mismatch, the results of the uncompressed (green) and compressed (magenta) datasets are overlaid in a single image (b, c; overlap in white). Representative compression levels were chosen at two different multiples of the photon shot noise, at $q=1\sigma$ (b) and $q=4\sigma$ (c). For all compression levels the segmentation overlap score ("Online Methods") was calculated and is plotted in (g) along with the achieved compression ratios.

4. REAL-TIME, GPU ACCELERATED IMAGE PROCESSING PIPELINE

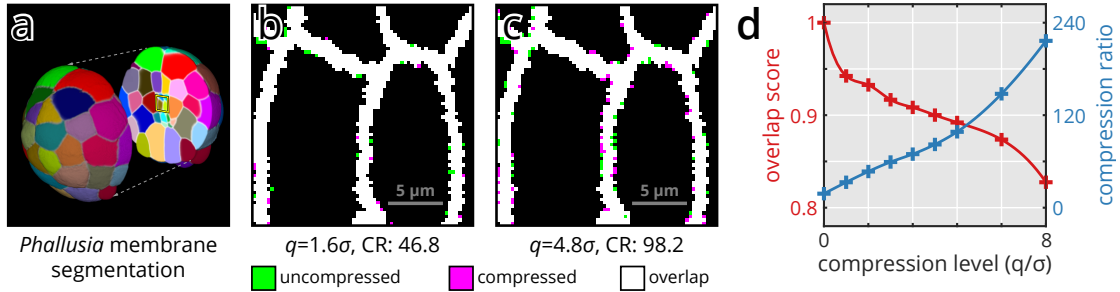


Figure 4.14: Influence of noise dependent lossy compression on 3D membrane segmentation. A *Phallusia mammillata* embryo expressing PH-citrine membrane marker was imaged in MuVi-SPIM [45], and 3D membrane segmentation was performed (“Supplementary Methods”) (a). The raw data was subsequently compressed at increasingly higher compression levels, and segmented using the same settings as the uncompressed data. To visualize segmentation mismatch, the results of the uncompressed (green) and compressed (magenta) datasets are overlaid in a single image (b, c; overlap in white). Representative compression levels were chosen at two different multiples of the photon shot noise, at $q=1.6\sigma$ (b) and $q=4.8\sigma$ (c). For all compression levels the segmentation overlap score (“Supplementary Methods”) was calculated and is plotted in (d) along with the achieved compression ratios.

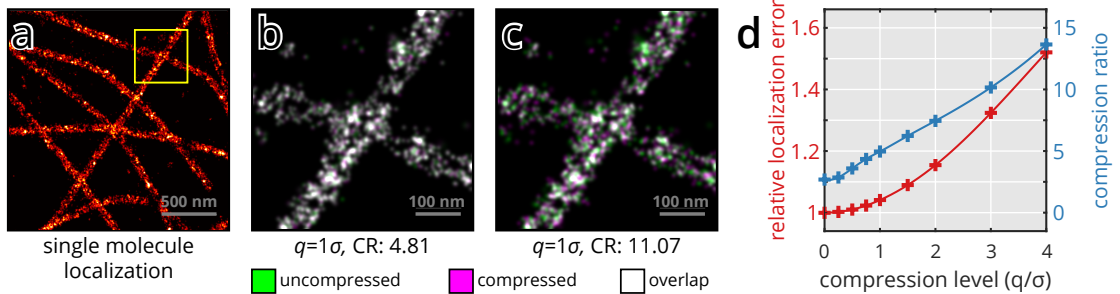


Figure 4.15: Influence of noise dependent lossy compression on single-molecule localization. Microtubules, immunolabeled with Alexa Fluor 647 were imaged by SMLM (a). The raw data was compressed at increasingly higher compression levels, and localized using the same settings as the uncompressed data. To visualize localization mismatch, the results of the uncompressed (green) and compressed (magenta) datasets are overlaid in a single image (b, c; overlap in white). Two representative compression levels were chosen at $q=1\sigma$ (b) and $q=4\sigma$ (c). To assess the effects of compression on localization precision, a simulated dataset with known emitter positions was compressed at various levels. For all compression levels the relative localization error (normalized to the Cramér–Rao lower bound) was calculated and is plotted in (d) along with the achieved compression factors.

9 where the sets A and B represent the pixels included in two different segmentations.

10 3D membrane segmentation

1 Raw MuVi-SPIM recordings of *Phallusia mammillata* embryos expressing PH-citrine
2 membrane marker were kindly provided by Ulla-Maj Fiuza (EMBL, Heidelberg). Each
3 recording consisted of 4 views at 90 degree rotations. The views were fused using an image
4 based registration algorithm followed by a sigmoidal blending of the 4 views. The fused
5 stack was then segmented using the MARS algorithm [151] with an hmin parameter
6 of 10. The raw data (all 4 views) was compressed at different levels, and segmented
7 using the same pipeline. Segmentation results were then processed in Matlab to calculate
8 the overlap score for the membranes using the Sørensen–Dice index (“Supplementary

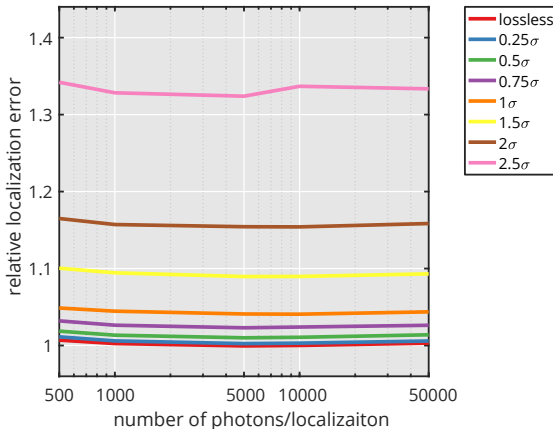


Figure 4.16: Change in localization error only depends on selected quantization step. We simulated multiple datasets (“Supplementary Methods”) with different average photon numbers per localization. Background was kept at a constant average of 20 photons/pixel. Datasets were compressed at multiple compression levels (see legend), and localization error relative to the Cramér-Rao lower bound was calculated. The relative localization error only depends on the compression level, and not on the signal to background illumination ratio.

9 Code”).

10 Single-molecule localization imaging

1 In order to visualize microtubules, U2OS cells were treated as in [152] and imaged in a
 2 dSTORM buffer [153]. In brief, the cells were permeabilized and fixed with glutaralde-
 3 hyde, washed, then incubated with primary tubulin antibodies and finally stained with
 4 Alexa Fluor 647 coupled secondary antibodies. The images were recorded on a home-built
 5 microscope previously described [152], in its 2D single-channel mode.

6 Single-molecule localization data analysis

7 Analysis of single-molecule localization data was performed on a custom-written MAT-
 8 LAB software as in [154]. Pixel values were converted to photon counts according to
 9 measured offset and calibrated gain of the camera (EMCCD iXon, Andor). The back-
 10 ground was estimated with a wavelet filter [155], background-subtracted images were
 11 thresholded and local maxima were detected on the same images. 7-pixel ROIs around
 12 the detected local maxima were extracted from the raw images and fitted with a GPU
 13 based MLE fitter [156]. Drift correction was performed based on cross-correlation. Fi-
 14 nally, images were reconstructed by filtering out localizations with a high uncertainty
 15 (>30 nm and large PSF (>150 nm) and Gaussian rendering.

4. REAL-TIME, GPU ACCELERATED IMAGE PROCESSING PIPELINE

16 Simulation of single-molecule localization data

17 Single molecule localization data was simulated in Matlab ("Supplementary Code") by
18 generating a grid of pixelated Gaussian spots with standard deviation of 1 pixel. With a
1 pixel size of a 100 nm, this corresponds to a FWHM of 235.48 nm. The center of each spot
2 was slightly offset from the pixel grid at 0.1 pixel increments in both x and y directions.
3 To this ground truth image a constant value was added for illumination background, and
1 finally Poisson noise was applied to the image. This process was repeated 10000 times
2 to obtain enough images for adequate accuracy.

3 Code availability

4 Code used for analyzing data, B³D source code and compiled binaries, including a filter
5 plugin for HDF5, is available for download at <https://git.embl.de/balazs/B3D>.

⁶ **Chapter 5**

⁷ **Discussion**

⁸ **5.1 New scientific results**

⁹ **Thesis I.** *I have designed and constructed a new light-sheet microscope suitable for*
¹⁰ *high sensitivity imaging of delicate samples. A novel arrangement of two high numerical*
¹¹ *aperture objectives in 120 degrees allows for near isotropic resolution while increasing*
¹² *light collection efficiency by a factor of two.*

¹³ Corresponding publications: [J3], [J2], [J1]

¹⁴ Live imaging of light sensitive specimens, such as a developing mouse embryo is a chal-
¹⁵ lenging task

¹⁶ **Thesis II.** *I have developed a GPU-based image processing pipeline for multi-view light-*
¹⁷ *sheet microscopy that enables real time fusion of opposing views.*

¹⁸ Corresponding publications: [C1], [C2], [C3]

¹⁹ **Thesis III.** *I have developed a new image compression algorithm that enables noise*
²⁰ *dependent lossy compression of light microscopy images, and can reach a compression*
²¹ *ratio of 100 fold while preserving the results of downstream data analysis steps.*

²² Corresponding publications: [J4], [C1], [C2], [C3]

²³ All microscopy images contain inherent noise, that is

²⁴ **Thesis IV.** *I have developed a new GPU-based image compression library, B^3D , that*
¹ *implements the algorithm described in Thesis III, and allows for real time compression*
² *of microscopy images with a throughput of up to 1 GB/s.*

¹ Corresponding publications: [J4], [C1], [C2], [C3]

¹ B^3D is an efficient, GPU-based image compression library allowing lossless and noise
² dependent lossy compression of microscopy images. Since many high-speed microscopy

5. DISCUSSION

- ³ methods generate immense amounts of data, easily reaching terabytes per experiment,
- ⁴ image compression is especially important to efficiently deal with such datasets.

⁵ Acknowledgements

ACKNOWLEDGEMENTS

⁶ **Appendix A**

⁷ **Bill of materials**

⁸ **Bill of Materials**

⁹ **Optical components**

¹⁰ • Lenses

- ¹¹ – 2×Nikon CFI75 Apo LWD 25x/1.10w water dipping objectives
- ¹² – 2×Nikon ITL200 200 mm tube lens
- ¹³ – 2×200 mm x 25 mm Dia. achromatic lens (Edmunds Optics, #47-645)
- ¹⁴ – 2×400 mm x 40 mm Dia. achromatic lens (Edmunds Optics, #49-281)
- ¹⁵ – 3×75 mm x 25 mm Dia. achromatic lens (Edmunds Optics, #47-639)
- ¹⁶ – SILL 112751 1:2 beam expander

¹⁷ • Filters

- ¹⁸ – 2×BrightLine quad-edge dichroic beam splitter (Semrock, Di03-R405/488/561/635-t3-25x36)
- ¹⁹ – EdgeBasic 488 nm long pass filter (Semrock, BLP01-488R-25)
- ²⁰ – BrightLine 525/50 band pass filter (Semrock, FF03-525/50-25)
- ²¹ – EdgeBasic 561 nm long pass filter (Semrock, BLP02-561R-25)
- ²² – RazorEdge 647 nm long pass filter (Semrock, LP02-647RU-25)

²⁴ • Mirrors

- ²⁵ – 6×1” Broadband Dielectric Elliptical Mirror (Thorlabs, BBE1-E03)
- ²⁶ – 2×30 mm Broadband 1/10λ Mirror (OptoSigma, TFMS-30C05-4/11)
- ²⁷ – 10 Pack of 1” Protected Silver Mirrors (Thorlabs, PF10-03-P01-10)
- ²⁸ – Knife-Edge Right-Angle Prism Dielectric Mirror (Thorlabs, MRAK25-E02)

²⁹ **Mechanical components**

- ¹ • 40 mm travel range pneumatic cylinder (Airtac, HM-10-040)
- ² • 5/2-way electric valve (Airtac, M-20-510-HN)
- ³ • 2×25 mm extended contact bearing steel stage (OptoSigma, TSDH-251C)
- ⁴ • 30x90 mm stainless steel slide (OptoSigma, IPWS-F3090)
- ⁵ • close proximity gimbal mirror mount (Thorlabs, GMB1/M)

APPENDIX A

- 6 • 30 mm cage elliptical mirror mount (Thorlabs, KCB1E)
- 7 • Melles Griot Performance Plus Optical Breadboard
- 8 • 4×Newport Stabilizer, High Performance laminar Flow Isolator, I-2000 Series

9 Custom parts

- 10 All parts are (anodized) aluminium, unless stated otherwise.
- 11 • 2×mirror holder block
- 12 • Front plate for objective, chamber and mirror mounting
- 13 • Imaging chamber (PEEK)
- 14 • Wedge ring and matching threaded ring to fasten objectives
- 15 • Camera bridge
- 16 • Illumination splitter unit
- 17 • adapter plates to mount stages

18 Electronics

- 19 • Embedded system (National Instruments, cRIO-9068) equipped with:
 - 20 – 2×C series digital I/O card (NI 9401)
 - 21 – 1×C Series 100 kS/s 4-channel Voltage Output Module (NI 9263)
 - 22 – 1×C Series 25 kS/s 16-channel Voltage Output Module (NI 9264)
- 23 • Omicron SOLE-3 laser combiner, with 488, 561 and 638 nm laser lines
- 24 • Andor Zyla 4.2 sCMOS Camera
- 1 • Galvanometric scanner mirror (Cambridge Technology, 6210B)
- 2 • 6 position filter wheel (Ludl Electronic Products, 96A361)
- 3 • Filter wheel controller unit (Ludl Electronic Products, MAC5000)
- 4 • 2 piezoelectric stages (Nanos Instruments, LPS-30-30-1-V2_61-S-N)
- 5 • 2 stage controller boards (Nanos Instruments, BMC101)

¹ Appendix B

² Appendix B

³ Data sizes in microscopy

⁴ Lossless compression performnace

⁵ Benchmarking datasets

	imaging device	image size	frame rate	data rate	data size
SPIM	2x sCMOS camera (e.g. Hamamatsu ORCA Flash4.0)	2048x2048	50/s	800 MB/s	10 TB
SMLM	2x EMCCD camera (e.g. Andor iXon Ultra 897)	512x512	56/s	56 MB/s	500 GB
screening	CCD camera (e.g. Hamamatsu ORCA-R2)	1344x1024	8.5s/	22 MB/s	5 TB
confocal	Zeiss LSM 880, 10 channels	512x512	5/s	12.5 MB/s	50 GB

Table B1: Data sizes in microscopy. Typical devices used for confocal microscopy, high-content screening, single-molecule localization microscopy and light-sheet microscopy and their data production characteristics. Data visualized on Figure 4.1

APPENDIX B

	write speed	read speed	CR	file size
B³D	1,115.08 MB/s	928.97 MB/s	9.861	100%
KLB	283.19 MB/s	619.95 MB/s	10.571	93.28%
JPEG2000	31.94 MB/s	26.38 MB/s	11.782	83.69%
JPEG2000	202.32 MB/s	161.08 MB/s	1.00	986.1%
TIFF + LZW	40.85 MB/s	102.37 MB/s	5.822	169.37%

Table B2: Lossless compression performance. B³D is compared with various popular lossless image compression methods regarding write speed, read speed and compression ratio (original size / compressed size). Data visualized on Figure 4.8.

Dataset name	Imaging modality	Description	Size (MB)
drosophila	SPIM	dataset acquired in MuVi-SPIM of a Drosophila melanogaster embryo expressing H2Av-mCherry nuclear marker	494.53
zebrafish	SPIM	dataset acquired in MuVi-SPIM of a zebrafish embryo expressing b-actin::GCaMP6f calcium sensor	2,408.00
phallusia	SPIM	dataset acquired in MuVi-SPIM of a Phallusia mammillata embryo expressing PH-citrine membrane marker	1,323.88
simulation	SMLM	MT0.N1.LD-2D simulated dataset of microtubules labeled with Alexa Fluor 647 from SMLMS 2016 challenge	156.22
microtubules	SMLM	microtubules immuno-labeled with Alexa Fluor 674-bound antibodies in U2OS cells	1,643.86
lifeact	SMLM	actin network labeled with LifeAct-tdEOS in U2OS cells	3,316.15
dapi	screening	wide field fluorescence images of DAPI stained HeLa Kyoto cells [157]	1,005.38
vsvg	screening	wide field fluorescence images of CFP-tsO45G proteins in HeLa Kyoto cells [157]	1,005.38
membrane	screening	wide field fluorescence images of membrane localized CFP-tsO45G proteins labeled with AlexaFluor647 in HeLa Kyoto cells [157]	1,005.38

Table B3: Datasets used for benchmarking compression performance.

APPENDIX B

⁶ Appendix C

⁷ Light collection efficiency of an ⁸ objective

⁹ Let's define light collection efficiency η as the ratio of collected photons and all emitted
¹⁰ photons:

$$\eta = \frac{N_{collected}}{N_{emitted}}$$

¹¹ Since we can assume that the direction of photons emitted from a fluorescent molecule
¹² are random, the light collection efficiency will correspond to the solid angle subtended
¹³ by the objective front lens at the focal point. To calculate this, let's consider the unit
¹⁴ sphere centered at the focal point, and calculate the surface area of the spherical cap
¹⁵ corresponding to the objective acceptance angle α (Fig. C.1a). The area of the cap can
¹⁶ be expressed as a function of the angle:

$$A_{cap} = 2\pi r^2(1 - \cos \alpha)$$

¹ The surface area of the full sphere is calculated as:

$$A_{sph} = 4\pi r^2$$

² For both equations r is the radius of the sphere. From here, the light collection efficiency
³ can be calculated as:

$$\eta = \frac{N_{collected}}{N_{emitted}} = \frac{A_{cap}}{A_{sph}} = \frac{1 - \cos \alpha}{2}$$

⁴ As most objectives are characterized by the numerical aperture, we also plot η as a
⁵ function of the NA on Figure C.1b.

APPENDIX C

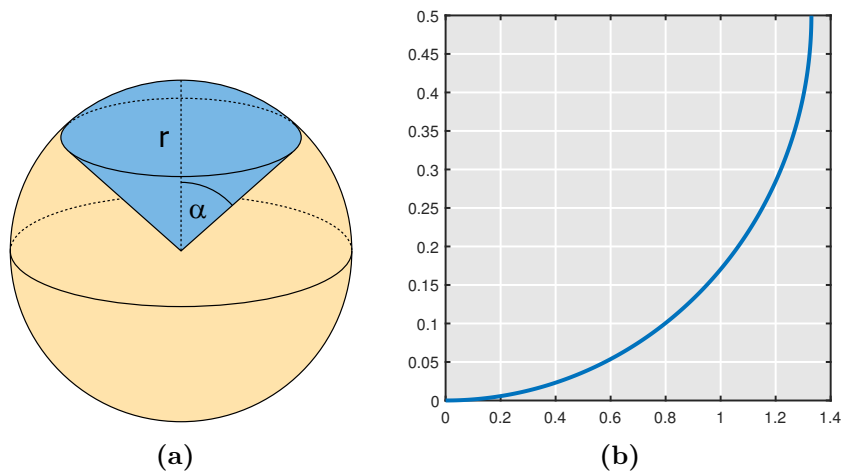


Figure C.1: Light collection efficiency of an objective. (a) Light collection efficiency is the ratio of photons collected by the objective and all emitted photons. If the fluorophores are emitted randomly in all directions, it will be the surface ratio of the conical section (blue) to the whole sphere. (b) Light collection efficiency (η) as a function of the numerical aperture (NA).

⁶ References

⁷ The author's publications

- ⁸ [J1] Patrick Hoyer, Gustavo de Medeiros, Bálint Balázs, Nils Norlin, Christina Besir, Janina Hanne, Hans-Georg Kräusslich, Johann Engelhardt, Steffen J. Sahl, Stefan W. Hell, and Lars Hufnagel. "Breaking the diffraction limit of light-sheet fluorescence microscopy by RESOLFT". *Proceedings of the National Academy of Sciences* 113.13 (Mar. 2016), pp. 3442–3446. DOI: [10.1073/pnas.1522292113](https://doi.org/10.1073/pnas.1522292113) (cit. on pp. 16, 17, 77).
- ¹⁴ [J2] Petr Strnad, Stefan Gunther, Judith Reichmann, Uros Krzic, Balint Balazs, Gustavo de Medeiros, Nils Norlin, Takashi Hiirogi, Lars Hufnagel, and Jan Ellenberg. "Inverted light-sheet microscope for imaging mouse pre-implantation development". *Nature Methods* 13.2 (Feb. 2016), pp. 139–142. DOI: [10.1038/nmeth.3690](https://doi.org/10.1038/nmeth.3690) (cit. on pp. 16, 23, 24, 77).
- ¹⁹ [J3] Gustavo de Medeiros, Bálint Balázs, and Lars Hufnagel. "Light-sheet imaging of mammalian development". *Seminars in Cell & Developmental Biology*. Mammalian development 55 (July 2016), pp. 148–155. DOI: [10.1016/j.semcdb.2015.11.001](https://doi.org/10.1016/j.semcdb.2015.11.001) (cit. on pp. 16, 77).
- ²³ [J4] Balint Balazs, Joran Deschamps, Marvin Albert, Jonas Ries, and Lars Hufnagel. "A real-time compression library for microscopy images". *bioRxiv* (July 2017), p. 164624. DOI: [10.1101/164624](https://doi.org/10.1101/164624) (cit. on p. 77).

² The author's others publications

- ³ [J5] Zoltán Jakus, Edina Simon, Bálint Balázs, and Attila Mócsai. "Genetic deficiency of Syk protects mice from autoantibody-induced arthritis". *Arthritis and Rheumatism* 62.7 (July 2010), pp. 1899–1910. DOI: [10.1002/art.27438](https://doi.org/10.1002/art.27438).

References cited in the thesis

- 6 [J6] Balázs Győrffy, Zsombor Benke, András Lánczky, Bálint Balázs, Zoltán Szallási,
7 József Timár, and Reinhold Schäfer. “RecurrenceOnline: an online analysis tool to
8 determine breast cancer recurrence and hormone receptor status using microarray
9 data”. *Breast Cancer Research and Treatment* (July 2011). DOI: 10.1007/s10549-
10 011-1676-y.
- 11 [J7] Weiwei Shi, Balint Balazs, Balazs Györffy, Tingting Jiang, W. Fraser Symmans,
12 Christos Hatzis, and Lajos Pusztai. “Combined analysis of gene expression, DNA
13 copy number, and mutation profiling data to display biological process anomalies
14 in individual breast cancers”. *Breast Cancer Research and Treatment* 144.3 (Mar.
15 2014), pp. 561–568. DOI: 10.1007/s10549-014-2904-z.

16 The author’s conference presentations

- 17 [C1] Bálint Balázs, Marvin Albert, and Lars Hufnagel. “GPU-based image processing
18 for multiview microscopy data”. *Light Sheet Fluorescence Microscopy International
19 Conference*. Sheffield, UK, Sept. 2016 (cit. on p. 77).
- 20 [C2] Bálint Balázs, Marvin Albert, and Lars Hufnagel. “GPU-based image processing
21 for multi-view microscopy data”. *Focus on Microscopy*. Taipei, Taiwan, Mar. 2016
22 (cit. on p. 77).
- 23 [C3] Bálint Balázs, Marvin Albert, and Lars Hufnagel. “GPU-based image processing
24 for multi-view microscopy data”. *Focus on Microscopy*. Bordeaux, France, Apr.
25 2017 (cit. on p. 77).

26 References cited in the thesis

- 27 [1] Scott F. Gilbert. *Developmental Biology*. 10th. Sinauer Associates, 2013 (cit. on
28 p. 3).
- 29 [2] Alberto Diaspro. *Optical Fluorescence Microscopy: From the Spectral to the Nano
30 Dimension*. 1st ed. Springer-Verlag Berlin Heidelberg, 2011 (cit. on pp. 3, 4).
- 31 [3] Philipp J Keller and Ernst HK Stelzer. “Quantitative in vivo imaging of en-
32 tire embryos with Digital Scanned Laser Light Sheet Fluorescence Microscopy”.
1 *Current Opinion in Neurobiology* 18.6 (Dec. 2008). review, pp. 624–632. DOI:
2 10.1016/j.conb.2009.03.008 (cit. on p. 3).
- 3 [4] Jan Huisken and Didier Y. R. Stainier. “Selective plane illumination microscopy
4 techniques in developmental biology”. *Development* 136.12 (June 2009), pp. 1963–
5 1975. DOI: 10.1242/dev.022426 (cit. on pp. 3, 16).

- 6 [5] Michael Weber and Jan Huisken. “Light sheet microscopy for real-time developmental biology”. *Current Opinion in Genetics & Development* 21.5 (2011),
7 pp. 566–572. DOI: [10.1016/j.gde.2011.09.009](https://doi.org/10.1016/j.gde.2011.09.009) (cit. on p. 3).
- 9 [6] Raju Tomer, Khaled Khairy, and Philipp J Keller. “Shedding light on the system: 10 studying embryonic development with light sheet microscopy”. *Current Opinion in 11 Genetics & Development*. Developmental mechanisms, patterning and evolution 21.5 (Oct. 2011). Review from 2011, pp. 558–565. DOI: [10.1016/j.gde.2011.07.003](https://doi.org/10.1016/j.gde.2011.07.003) (cit. on p. 3).
- 14 [7] Hans-Ulrich Dodt, Ulrich Leischner, Anja Schierloh, Nina Jährling, Christoph 15 Peter Mauch, Katrin Deininger, Jan Michael Deussing, Matthias Eder, Walter 16 Ziegglänsberger, and Klaus Becker. “Ultramicroscopy: three-dimensional visual- 17 ization of neuronal networks in the whole mouse brain”. *Nature Methods* 4.4 (Mar. 18 2007), pp. 331–336. DOI: [10.1038/nmeth1036](https://doi.org/10.1038/nmeth1036) (cit. on pp. 3, 16, 26).
- 19 [8] Bi-Chang Chen et al. “Lattice light-sheet microscopy: Imaging molecules to 20 embryos at high spatiotemporal resolution”. *Science* 346.6208 (Oct. 2014), 21 p. 1257998. DOI: [10.1126/science.1257998](https://doi.org/10.1126/science.1257998) (cit. on pp. 3, 17).
- 22 [9] P. Philippe Laissue, Rana A. Alghamdi, Pavel Tomancak, Emmanuel G. Reynaud, 23 and Hari Shroff. “Assessing phototoxicity in live fluorescence imaging”. *Nature 24 Methods* 14.7 (July 2017), pp. 657–661. DOI: [10.1038/nmeth.4344](https://doi.org/10.1038/nmeth.4344) (cit. on pp. 3, 25 4, 31).
- 26 [10] Jeff W. Lichtman and José-Angel Conchello. “Fluorescence microscopy”. *Nature 27 Methods* 2.12 (Dec. 2005), pp. 910–919. DOI: [10.1038/nmeth817](https://doi.org/10.1038/nmeth817) (cit. on p. 4).
- 28 [11] G. G. Stokes. “On the Change of Refrangibility of Light”. *Philosophical Transac- 29 tions of the Royal Society of London* 142 (Jan. 1852), pp. 463–562. DOI: [10.1098/rstl.1852.0022](https://doi.org/10.1098/rstl.1852.0022) (cit. on p. 4).
- 31 [12] *Spectra Viewer*. Text (cit. on p. 5).
- 32 [13] Robert Bacallao, Morgane Bomsel, Ernst H. K. Stelzer, and Jan De Mey. “Guiding 33 Principles of Specimen Preservation for Confocal Fluorescence Microscopy”. *Hand- 34 book of Biological Confocal Microscopy*. DOI: [10.1007/978-1-4615-7133-9_18](https://doi.org/10.1007/978-1-4615-7133-9_18). 1 Springer, Boston, MA, 1990, pp. 197–205 (cit. on p. 5).
- 2 [14] O. Shimomura, F. H. Johnson, and Y. Saiga. “Extraction, purification and prop- 3 erties of aequorin, a bioluminescent protein from the luminous hydromedusan, 4 Aequorea”. *Journal of Cellular and Comparative Physiology* 59 (June 1962). first 5 purification of GFP from jellyfish, pp. 223–239 (cit. on p. 5).

References cited in the thesis

- [15] Douglas C. Prasher, Virginia K. Eckenrode, William W. Ward, Frank G. Prendergast, and Milton J. Cormier. “Primary structure of the *Aequorea victoria* green-fluorescent protein”. *Gene* 111.2 (Feb. 1992). cloning GFP cDNA, pp. 229–233. DOI: [10.1016/0378-1119\(92\)90691-H](https://doi.org/10.1016/0378-1119(92)90691-H) (cit. on p. 5).
- [16] M. Chalfie, Y. Tu, G. Euskirchen, W. W. Ward, and D. C. Prasher. “Green fluorescent protein as a marker for gene expression”. *Science* 263.5148 (Feb. 1994). GFP in *c. elegans* / nematodes, pp. 802–805. DOI: [10.1126/science.8303295](https://doi.org/10.1126/science.8303295) (cit. on p. 5).
- [17] Adam Amsterdam, Shuo Lin, and Nancy Hopkins. “The *Aequorea victoria* Green Fluorescent Protein Can Be Used as a Reporter in Live Zebrafish Embryos”. *Developmental Biology* 171.1 (Sept. 1995). first GFP zebrafish, pp. 123–129. DOI: [10.1006/dbio.1995.1265](https://doi.org/10.1006/dbio.1995.1265) (cit. on p. 5).
- [18] Masaru Okabe, Masahito Ikawa, Katsuya Kominami, Tomoko Nakanishi, and Yoshitake Nishimune. “‘Green mice’ as a source of ubiquitous green cells”. *FEBS Letters* 407.3 (May 1997). first EGFP mouse, pp. 313–319. DOI: [10.1016/S0014-5793\(97\)00313-X](https://doi.org/10.1016/S0014-5793(97)00313-X) (cit. on p. 5).
- [19] R Heim, D C Prasher, and R Y Tsien. “Wavelength mutations and posttranslational autoxidation of green fluorescent protein.” *Proceedings of the National Academy of Sciences of the United States of America* 91.26 (Dec. 1994), pp. 12501–12504 (cit. on p. 5).
- [20] Roger Heim and Roger Y Tsien. “Engineering green fluorescent protein for improved brightness, longer wavelengths and fluorescence resonance energy transfer”. *Current Biology* 6.2 (Feb. 1996), pp. 178–182. DOI: [10.1016/S0960-9822\(02\)00450-5](https://doi.org/10.1016/S0960-9822(02)00450-5) (cit. on p. 5).
- [21] Brendan P. Cormack, Raphael H. Valdivia, and Stanley Falkow. “FACS-optimized mutants of the green fluorescent protein (GFP)”. *Gene. Flourescent Proteins and Applications* 173.1 (1996), pp. 33–38. DOI: [10.1016/0378-1119\(95\)00685-0](https://doi.org/10.1016/0378-1119(95)00685-0) (cit. on p. 5).
- [22] Robert F. Service. “Three Scientists Bask in Prize’s Fluorescent Glow”. *Science* 322.5900 (Oct. 2008), pp. 361–361. DOI: [10.1126/science.322.5900.361](https://doi.org/10.1126/science.322.5900.361) (cit. on p. 5).
- [23] E. Abbe. “Beiträge zur Theorie des Mikroskops und der mikroskopischen Wahrnehmung”. *Archiv für mikroskopische Anatomie* 9.1 (1873), pp. 413–418. DOI: [10.1007/BF02956173](https://doi.org/10.1007/BF02956173) (cit. on p. 8).

- 6 [24] Max Born and Emil Wolf. *Principles of Optics: Electromagnetic Theory of Propagation, Interference and Diffraction of Light*. Elsevier, June 2013 (cit. on pp. 8,
7 9, 53).
- 9 [25] C. J. R. Sheppard and H. J. Matthews. “Imaging in high-aperture optical systems”. *JOSA A* 4.8 (Aug. 1987), pp. 1354–1360. DOI: [10.1364/JOSAA.4.001354](https://doi.org/10.1364/JOSAA.4.001354) (cit. on p. 8).
- 12 [26] Lord Rayleigh F.R.S. “XXXI. Investigations in optics, with special reference to
13 the spectroscope”. *Philosophical Magazine* 8.49 (Oct. 1879), pp. 261–274. DOI:
14 [10.1080/14786447908639684](https://doi.org/10.1080/14786447908639684) (cit. on p. 9).
- 15 [27] Jim Swoger, Jan Huisken, and Ernst H. K. Stelzer. “Multiple imaging axis mi-
16 croscopy improves resolution for thick-sample applications”. *Optics Letters* 28.18
17 (Sept. 2003), p. 1654. DOI: [10.1364/OL.28.001654](https://doi.org/10.1364/OL.28.001654) (cit. on p. 11).
- 18 [28] Jim Swoger, Peter Verveer, Klaus Greger, Jan Huisken, and Ernst H. K. Stelzer.
19 “Multi-view image fusion improves resolution in three-dimensional microscopy”.
20 *Optics Express* 15.13 (2007), p. 8029. DOI: [10.1364/OE.15.008029](https://doi.org/10.1364/OE.15.008029) (cit. on pp. 11,
21 30).
- 22 [29] Marvin Minsky. “Microscopy apparatus”. US3013467 A. U.S. Classification
23 356/432, 359/389, 348/79, 250/215; International Classification G02B21/00;
24 Cooperative Classification G02B21/0024, G02B21/002; European Classification
25 G02B21/00M4A, G02B21/00M4. Dec. 1961 (cit. on p. 12).
- 26 [30] Paul Davidovits and M. David Egger. “Scanning Laser Microscope”. *Nature*
27 223.5208 (Aug. 1969), pp. 831–831. DOI: [10.1038/223831a0](https://doi.org/10.1038/223831a0) (cit. on p. 12).
- 28 [31] Ernst H.K. Stelzer and Steffen Lindek. “Fundamental reduction of the observation
29 volume in far-field light microscopy by detection orthogonal to the illumination
30 axis: confocal theta microscopy”. *Optics Communications* 111.5–6 (Oct. 1994),
31 pp. 536–547. DOI: [10.1016/0030-4018\(94\)90533-9](https://doi.org/10.1016/0030-4018(94)90533-9) (cit. on p. 14).
- 32 [32] Silvia Aldaz, Luis M. Escudero, and Matthew Freeman. “Live Imaging of
33 Drosophila Imaginal Disc Development”. *Proceedings of the National Academy of
34 Sciences* 107.32 (Aug. 2010), pp. 14217–14222. DOI: [10.1073/pnas.1008623107](https://doi.org/10.1073/pnas.1008623107)
1 (cit. on p. 14).
- 2 [33] Jean-Léon Maître, Hervé Turlier, Rukshala Illukkumbura, Björn Eismann, Rit-
3 suya Niwayama, François Nédélec, and Takashi Hiiragi. “Asymmetric division
4 of contractile domains couples cell positioning and fate specification”. *Nature*
5 536.7616 (Aug. 2016), pp. 344–348. DOI: [10.1038/nature18958](https://doi.org/10.1038/nature18958) (cit. on pp. 14,
6 22).

References cited in the thesis

- [34] Emmanuel G. Reynaud, Uroš Kržič, Klaus Greger, and Ernst H.K. Stelzer. “Light sheet-based fluorescence microscopy: more dimensions, more photons, and less photodamage”. *HFSP Journal* 2.5 (Oct. 2008), pp. 266–275. DOI: 10.2976/1.2974980 (cit. on p. 14).
- [35] Stelzer. “Contrast, resolution, pixelation, dynamic range and signal-to-noise ratio: fundamental limits to resolution in fluorescence light microscopy”. *Journal of Microscopy* 189.1 (Jan. 1998). This is also the reason why it is sufficient to store the square root of the count rate. That number will contain all the available information., pp. 15–24. DOI: 10.1046/j.1365-2818.1998.00290.x (cit. on p. 14).
- [36] H. Siedentopf and R. Zsigmondy. “Über Sichtbarmachung und Größenbestimmung ultramikroskopischer Teilchen, mit besonderer Anwendung auf Goldrubiingläser”. *Annalen der Physik* 315.1 (1902), pp. 1–39. DOI: 10.1002/andp.19023150102 (cit. on p. 15).
- [37] A H Voie, D H Burns, and F A Spelman. “Orthogonal-plane fluorescence optical sectioning: three-dimensional imaging of macroscopic biological specimens”. *Journal of Microscopy* 170.Pt 3 (June 1993), pp. 229–36. DOI: 8371260 (cit. on p. 15).
- [38] Arne H. Voie and Francis A. Spelman. “Three-dimensional reconstruction of the cochlea from two-dimensional images of optical sections”. *Computerized Medical Imaging and Graphics* 19.5 (Sept. 1995), pp. 377–384. DOI: 10.1016/0895-6111(95)00034-8 (cit. on p. 15).
- [39] Eran Fuchs, Jules S. Jaffe, Richard A. Long, and Farooq Azam. “Thin laser light sheet microscope for microbial oceanography”. *Optics Express* 10.2 (Jan. 2002), pp. 145–154. DOI: 10.1364/OE.10.000145 (cit. on p. 15).
- [40] Jan Huisken, Jim Swoger, Filippo Del Bene, Joachim Wittbrodt, and Ernst H. K Stelzer. “Optical Sectioning Deep Inside Live Embryos by Selective Plane Illumination Microscopy”. *Science* 305.5686 (2004), pp. 1007–1009 (cit. on pp. 16, 18).
- [41] Jérémie Capoulade, Malte Wachsmuth, Lars Hufnagel, and Michael Knop. “Quantitative fluorescence imaging of protein diffusion and interaction in living cells”. *Nature Biotechnology* 29.9 (Sept. 2011), pp. 835–839. DOI: 10.1038/nbt.1928 (cit. on p. 16).
- [42] Yicong Wu, Alireza Ghitani, Ryan Christensen, Anthony Santella, Zhuo Du, Gary Rondeau, Zhirong Bao, Daniel Colón-Ramos, and Hari Shroff. “Inverted selective plane illumination microscopy (iSPIM) enables coupled cell identity lineage and

- 7 neurodevelopmental imaging in *Caenorhabditis elegans*”. *Proceedings of the National Academy of Sciences* 108.43 (Oct. 2011). iSPIM, tracking *c. elegans* nuclei,
8 pp. 17708–17713. DOI: 10.1073/pnas.1108494108 (cit. on p. 16).
- 9
- 10 [43] Yicong Wu et al. “Spatially isotropic four-dimensional imaging with dual-
11 view plane illumination microscopy”. *Nature Biotechnology* 31.11 (Nov. 2013),
12 pp. 1032–1038. DOI: 10.1038/nbt.2713 (cit. on pp. 16, 30).
- 13 [44] Jan Huisken and Didier Y. R. Stainier. “Even fluorescence excitation by multidirectional
14 selective plane illumination microscopy (mSPIM)”. *Optics Letters* 32.17
15 (2007), pp. 2608–2610. DOI: 10.1364/OL.32.002608 (cit. on pp. 16, 17, 20).
- 16 [45] Uros Krzic, Stefan Gunther, Timothy E. Saunders, Sebastian J. Streichan, and
17 Lars Hufnagel. “Multiview light-sheet microscope for rapid *in toto* imaging”. *Nature Methods* 9.7 (July 2012). MuVi-SPIM, pp. 730–733. DOI: 10.1038/nmeth.2064 (cit. on pp. 16, 17, 61–63, 66, 70, 73, 74).
- 18
- 19 [46] Raju Tomer, Khaled Khairy, Fernando Amat, and Philipp J. Keller. “Quantitative
20 high-speed imaging of entire developing embryos with simultaneous multiview
21 light-sheet microscopy”. *Nature Methods* 9.7 (July 2012). SimView, pp. 755–763.
22 DOI: 10.1038/nmeth.2062 (cit. on pp. 16, 17).
- 23
- 24 [47] Benjamin Schmid, Gopi Shah, Nico Scherf, Michael Weber, Konstantin Thierbach,
25 Citlali Pérez Campos, Ingo Roeder, Pia Aanstad, and Jan Huisken. “High-speed
26 panoramic light-sheet microscopy reveals global endodermal cell dynamics”. *Nature Communications* 4 (July 2013). zebrafish sphere projection + FEP tube. DOI:
27 10.1038/ncomms3207 (cit. on pp. 16, 17).
- 28
- 29 [48] Raghav K. Chhetri, Fernando Amat, Yinan Wan, Burkhard Höckendorf, William
30 C. Lemon, and Philipp J. Keller. “Whole-animal functional and developmental
31 imaging with isotropic spatial resolution”. *Nature Methods* 12.12 (Dec. 2015),
32 pp. 1171–1178. DOI: 10.1038/nmeth.3632 (cit. on pp. 16, 17).
- 33
- 34 [49] Philipp J. Keller, Annette D. Schmidt, Joachim Wittbrodt, and Ernst H. K.
35 Stelzer. “Reconstruction of Zebrafish Early Embryonic Development by Scanned
36 Light Sheet Microscopy”. *Science* 322.5904 (Nov. 2008), pp. 1065–1069. DOI: 10.
1126/science.1162493 (cit. on pp. 16, 18, 21, 63).
- 1 [50] Takehiko Ichikawa, Kenichi Nakazato, Philipp J. Keller, Hiroko Kajiura-
2 Kobayashi, Ernst H. K. Stelzer, Atsushi Mochizuki, and Shigenori Nonaka. “Live
3 Imaging of Whole Mouse Embryos during Gastrulation: Migration Analyses of
4 Epiblast and Mesodermal Cells”. *PLoS ONE* 8.7 (July 2013). post implantation,
5 e64506. DOI: 10.1371/journal.pone.0064506 (cit. on pp. 16, 25).

References cited in the thesis

- [51] Ryan S. Udan, Victor G. Piazza, Chih-wei Hsu, Anna-Katerina Hadjantonakis, and Mary E. Dickinson. “Quantitative imaging of cell dynamics in mouse embryos using light-sheet microscopy”. *Development* (Oct. 2014). post implantation, dev.111021. DOI: 10.1242/dev.111021 (cit. on pp. 16, 25).
- [52] Abhishek Kumar et al. “Dual-view plane illumination microscopy for rapid and spatially isotropic imaging”. *Nature Protocols* 9.11 (Nov. 2014). diSPIM, pp. 2555–2573. DOI: 10.1038/nprot.2014.172 (cit. on p. 16).
- [53] Francesca Cella Zanacchi, Zeno Lavagnino, Michela Perrone Donnorso, Alessio Del Bue, Laura Furia, Mario Faretta, and Alberto Diaspro. “Live-cell 3D super-resolution imaging in thick biological samples”. *Nature Methods* 8.12 (Dec. 2011), pp. 1047–1049. DOI: 10.1038/nmeth.1744 (cit. on p. 17).
- [54] Mike Friedrich, Qiang Gan, Vladimir Ermolayev, and Gregory S. Harms. “STED-SPIM: Stimulated Emission Depletion Improves Sheet Illumination Microscopy Resolution”. *Biophysical Journal* 100.8 (Apr. 2011), pp. L43–L45. DOI: 10.1016/j.bpj.2010.12.3748 (cit. on p. 17).
- [55] Philipp J. Keller, Annette D. Schmidt, Anthony Santella, Khaled Khairy, Zhirong Bao, Joachim Wittbrodt, and Ernst H. K. Stelzer. “Fast, high-contrast imaging of animal development with scanned light sheet-based structured-illumination microscopy”. *Nature Methods* 7.8 (Aug. 2010). light-sheet structured illumination, pp. 637–642. DOI: 10.1038/nmeth.1476 (cit. on pp. 17, 53).
- [56] Bo-Jui Chang, Victor Didier Perez Meza, and Ernst H. K. Stelzer. “csiLSFM combines light-sheet fluorescence microscopy and coherent structured illumination for a lateral resolution below 100 nm”. *Proceedings of the National Academy of Sciences* 114.19 (May 2017), pp. 4869–4874. DOI: 10.1073/pnas.1609278114 (cit. on pp. 17, 53).
- [57] K. Greger, J. Swoger, and E. H. K. Stelzer. “Basic building units and properties of a fluorescence single plane illumination microscope”. *Review of Scientific Instruments* 78.2 (Feb. 2007), pp. 023705–023705–7. DOI: doi:10.1063/1.2428277 (cit. on p. 18).
- [58] Bahaa E. A. Saleh and Malvin Carl Teich. *Fundamentals of Photonics*. John Wiley & Sons, Mar. 2007 (cit. on p. 19).
- [59] David M. Shotton. “Confocal scanning optical microscopy and its applications for biological specimens”. *Journal of Cell Science* 94.2 (Oct. 1989), pp. 175–206 (cit. on p. 22).

- 4 [60] Ralph Gräf, Jens Rietdorf, and Timo Zimmermann. “Live Cell Spinning Disk
5 Microscopy”. *Microscopy Techniques*. Advances in Biochemical Engineering. DOI:
6 10.1007/b102210. Springer, Berlin, Heidelberg, 2005, pp. 57–75 (cit. on p. 22).
- 7 [61] James Jonkman and Claire M. Brown. “Any Way You Slice It—A Comparison
8 of Confocal Microscopy Techniques”. *Journal of Biomolecular Techniques : JBT*
9 26.2 (July 2015), pp. 54–65. DOI: 10.7171/jbt.15-2602-003 (cit. on p. 22).
- 10 [62] G. S. Kino. “Intermediate Optics in Nipkow Disk Microscopes”. *Handbook of*
11 *Biological Confocal Microscopy*. DOI: 10.1007/978-1-4615-7133-9_10. Springer,
12 Boston, MA, 1990, pp. 105–111 (cit. on p. 22).
- 13 [63] Akihiko Nakano. “Spinning-disk Confocal Microscopy — A Cutting-Edge Tool for
14 Imaging of Membrane Traffic”. *Cell Structure and Function* 27.5 (2002), pp. 349–
15 355. DOI: 10.1247/csf.27.349 (cit. on p. 22).
- 16 [64] Ekaterina Korotkevich, Ritsuya Niwayama, Aurélien Courtois, Stefanie Friese,
17 Nicolas Berger, Frank Buchholz, and Takashi Hiiragi. “The Apical Domain Is
18 Required and Sufficient for the First Lineage Segregation in the Mouse Embryo”.
19 *Developmental Cell* 40.3 (2017), 235–247.e7. DOI: <http://dx.doi.org/10.1016/j.devcel.2017.01.006> (cit. on p. 22).
- 21 [65] Jean-Léon Maître, Ritsuya Niwayama, Hervé Turlier, François Nédélec, and
22 Takashi Hiiragi. “Pulsatile cell-autonomous contractility drives compaction in
23 the mouse embryo”. *Nature Cell Biology* 17.7 (July 2015), pp. 849–855. DOI:
24 10.1038/ncb3185 (cit. on p. 22).
- 25 [66] Jens-Erik Dietrich, Laura Panavaite, Stefan Gunther, Sebastian Wennekamp,
26 Anna C. Groner, Anton Pigge, Stefanie Salvenmoser, Didier Trono, Lars Huf-
27 nagel, and Takashi Hiiragi. “Venus trap in the mouse embryo reveals distinct
28 molecular dynamics underlying specification of first embryonic lineages”. *EMBO*
29 *reports* 16.8 (Aug. 2015), pp. 1005–1021. DOI: 10.15252/embr.201540162 (cit. on
30 p. 22).
- 31 [67] Sonja Nowotschin, Anna Ferrer-Vaquer, and Anna-Katerina Hadjantonakis.
32 “Chapter 20 - Imaging Mouse Development with Confocal Time-Lapse Mi-
33 croscopy”. *Methods in Enzymology*. Ed. by Paul M. Wassarman and Philippe M.
34 Soriano. Vol. 476. Guide to Techniques in Mouse Development, Part A: Mice,
35 Embryos, and Cells, 2nd Edition. Academic Press, 2010, pp. 351–377 (cit. on
1 p. 22).
- 2 [68] Lewis Wolpert. *Principles of Development*. OUP Oxford, Jan. 2011 (cit. on p. 22).

References cited in the thesis

- [69] Adam S. Doherty and Richard M. Schultz. “Culture of Preimplantation Mouse Embryos”. *Developmental Biology Protocols*. Methods in Molecular Biology™. DOI: 10.1385/1-59259-685-1:47. Humana Press, 2000, pp. 47–52 (cit. on p. 23).
- [70] Jens-Erik Dietrich and Takashi Hiiragi. “Stochastic patterning in the mouse pre-implantation embryo”. *Development* 134.23 (Dec. 2007), pp. 4219–4231. DOI: 10.1242/dev.003798 (cit. on p. 23).
- [71] W. Denk, J. H. Strickler, and W. W. Webb. “Two-photon laser scanning fluorescence microscopy”. *Science* 248.4951 (Apr. 1990), pp. 73–76. DOI: 10.1126/science.2321027 (cit. on p. 23).
- [72] Jayne M. Squirrell, David L. Wokosin, John G. White, and Barry D. Bavisster. “Long-term two-photon fluorescence imaging of mammalian embryos without compromising viability”. *Nature Biotechnology* 17.8 (Aug. 1999). low damage live-cell imaging with two-photon caser scanning hamster, pp. 763–767. DOI: 10.1038/11698 (cit. on p. 23).
- [73] Katie McDole, Yuan Xiong, Pablo A. Iglesias, and Yixian Zheng. “Lineage mapping the pre-implantation mouse embryo by two-photon microscopy, new insights into the segregation of cell fates”. *Developmental Biology* 355.2 (July 2011), pp. 239–249. DOI: 10.1016/j.ydbio.2011.04.024 (cit. on p. 23).
- [74] Kazuo Yamagata, Rinako Suetsugu, and Teruhiko Wakayama. “Long-Term, Six-Dimensional Live-Cell Imaging for the Mouse Preimplantation Embryo That Does Not Affect Full-Term Development”. *Journal of Reproduction and Development* 55.3 (2009), pp. 343–350. DOI: 10.1262/jrd.20166 (cit. on p. 23).
- [75] Gustavo de Medeiros, Nils Norlin, Stefan Gunther, Marvin Albert, Laura Panavaite, Ulla-Maj Fiuza, Francesca Peri, Takashi Hiiragi, Uros Krzic, and Lars Hufnagel. “Confocal multiview light-sheet microscopy”. *Nature Communications* 6 (Nov. 2015), p. 8881. DOI: 10.1038/ncomms9881 (cit. on pp. 25, 26, 63, 64, 70).
- [76] Laura Panavaite, Balint Balazs, Tristan Rodriguez, Shankar Srinivas, Jerome Collignon, Lars Hufnagel, and Takashi Hiiragi. “3D-geec: a method for studying mouse peri-implantation development”. *Mechanisms of Development*. 18th International Congress of Developmental Biology 18-22 June, University Cultural Centre, National University of Singapore 145.Supplement (July 2017), S78–S79. DOI: 10.1016/j.mod.2017.04.189 (cit. on p. 24).
- [77] Yu-Chih Hsu. “In vitro development of individually cultured whole mouse embryos from blastocyst to early somite stage”. *Developmental Biology* 68.2 (Feb. 1979). post-implantation culture, pp. 453–461. DOI: 10.1016/0012-1606(79)90217-3 (cit. on p. 24).

- 4 [78] Fu-Jen Huang, Tsung-Chieh J. Wu, and Meng-Yin Tsai. “Effect of retinoic acid
5 on implantation and post-implantation development of mouse embryos in vitro”.
6 *Human Reproduction* 16.10 (Oct. 2001). post-implantation culture, pp. 2171–2176.
7 DOI: 10.1093/humrep/16.10.2171 (cit. on p. 24).
- 8 [79] Sonja Nowotschin and Anna-Katerina Hadjantonakis. “Cellular dynamics in the
9 early mouse embryo: from axis formation to gastrulation”. *Current Opinion in*
10 *Genetics & Development*. Developmental mechanisms, patterning and evolution
11 20.4 (Aug. 2010), pp. 420–427. DOI: 10.1016/j.gde.2010.05.008 (cit. on p. 24).
- 12 [80] Monica D. Garcia, Ryan S. Udan, Anna-Katerina Hadjantonakis, and Mary E.
13 Dickinson. “Live Imaging of Mouse Embryos”. *Cold Spring Harbor Protocols*
14 2011.4 (Apr. 2011), pdb.top104. DOI: 10.1101/pdb.top104 (cit. on p. 24).
- 15 [81] Alessandro Bria and Giulio Iannello. “TeraStitcher - A tool for fast automatic
16 3D-stitching of teravoxel-sized microscopy images”. *BMC Bioinformatics* 13 (Nov.
17 2012), p. 316. DOI: 10.1186/1471-2105-13-316 (cit. on p. 27).
- 18 [82] Gergely Katona, Gergely Szalay, Pál Maák, Attila Kaszás, Máté Veress, Dániel
19 Hillier, Balázs Chiovini, E. Sylvester Vizi, Botond Roska, and Balázs Rózsa. “Fast
20 two-photon in vivo imaging with three-dimensional random-access scanning in
21 large tissue volumes”. *Nature Methods* 9.2 (Feb. 2012), pp. 201–208. DOI: 10.
22 1038/nmeth.1851 (cit. on p. 27).
- 23 [83] Hiroshi Hama, Hiroshi Kurokawa, Hiroyuki Kawano, Ryoko Ando, Tomomi Shi-
24 mogori, Hisayori Noda, Kiyoko Fukami, Asako Sakaue-Sawano, and Atsushi
25 Miyawaki. “Scale: a chemical approach for fluorescence imaging and recon-
26 struction of transparent mouse brain”. *Nature Neuroscience* 14.11 (Nov. 2011),
27 pp. 1481–1488. DOI: 10.1038/nn.2928 (cit. on p. 27).
- 28 [84] Ali Ertürk, Klaus Becker, Nina Jährling, Christoph P. Mauch, Caroline D. Hojer,
29 Jackson G. Egen, Farida Hellal, Frank Bradke, Morgan Sheng, and Hans-Ulrich
30 Dodt. “Three-dimensional imaging of solvent-cleared organs using 3DISCO”. *Na-
31 ture Protocols* 7.11 (Nov. 2012), pp. 1983–1995. DOI: 10.1038/nprot.2012.119
32 (cit. on p. 27).
- 33 [85] Ali Ertürk et al. “Three-dimensional imaging of the unsectioned adult spinal cord
34 to assess axon regeneration and glial responses after injury”. *Nature Medicine* 18.1
35 (Jan. 2012), pp. 166–171. DOI: 10.1038/nm.2600 (cit. on p. 27).
- 1 [86] Takaaki Kuwajima, Austen A. Sitko, Punita Bhansali, Chris Jurgens, William
2 Guido, and Carol Mason. “ClearT: a detergent- and solvent-free clearing method
3 for neuronal and non-neuronal tissue”. *Development* 140.6 (Mar. 2013), pp. 1364–
4 1368. DOI: 10.1242/dev.091844 (cit. on p. 27).

References cited in the thesis

- [87] Meng-Tsen Ke, Satoshi Fujimoto, and Takeshi Imai. “SeeDB: a simple and morphology-preserving optical clearing agent for neuronal circuit reconstruction”. *Nature Neuroscience* 16.8 (Aug. 2013), pp. 1154–1161. DOI: [10.1038/nn.3447](https://doi.org/10.1038/nn.3447) (cit. on p. 27).
- [88] Kwanghun Chung and Karl Deisseroth. “CLARITY for mapping the nervous system”. *Nature Methods* 10.6 (June 2013), pp. 508–513. DOI: [10.1038/nmeth.2481](https://doi.org/10.1038/nmeth.2481) (cit. on p. 27).
- [89] Raju Tomer, Li Ye, Brian Hsueh, and Karl Deisseroth. “Advanced CLARITY for rapid and high-resolution imaging of intact tissues”. *Nature Protocols* 9.7 (July 2014), pp. 1682–1697. DOI: [10.1038/nprot.2014.123](https://doi.org/10.1038/nprot.2014.123) (cit. on p. 27).
- [90] Etsuo A. Susaki et al. “Whole-Brain Imaging with Single-Cell Resolution Using Chemical Cocktails and Computational Analysis”. *Cell* 157.3 (Apr. 2014), pp. 726–739. DOI: [10.1016/j.cell.2014.03.042](https://doi.org/10.1016/j.cell.2014.03.042) (cit. on p. 27).
- [91] Nicolas Renier, Zhuhao Wu, David J. Simon, Jing Yang, Pablo Ariel, and Marc Tessier-Lavigne. “iDISCO: A Simple, Rapid Method to Immunolabel Large Tissue Samples for Volume Imaging”. *Cell* 159.4 (Nov. 2014), pp. 896–910. DOI: [10.1016/j.cell.2014.10.010](https://doi.org/10.1016/j.cell.2014.10.010) (cit. on p. 27).
- [92] Kazuki Tainaka, Shimpei I. Kubota, Takeru Q. Suyama, Etsuo A. Susaki, Dimitri Perrin, Maki Ukai-Tadenuma, Hideki Ukai, and Hiroki R. Ueda. “Whole-Body Imaging with Single-Cell Resolution by Tissue Decolorization”. *Cell* 159.4 (Nov. 2014), pp. 911–924. DOI: [10.1016/j.cell.2014.10.034](https://doi.org/10.1016/j.cell.2014.10.034) (cit. on p. 27).
- [93] Tongcang Li, Sadao Ota, Jeongmin Kim, Zi Jing Wong, Yuan Wang, Xiaobo Yin, and Xiang Zhang. “Axial Plane Optical Microscopy”. *Scientific Reports* 4 (Dec. 2014). DOI: [10.1038/srep07253](https://doi.org/10.1038/srep07253) (cit. on p. 27).
- [94] Matthew B. Bouchard, Venkatakaushik Voleti, César S. Mendes, Clay Lacefield, Wesley B. Grueber, Richard S. Mann, Randy M. Bruno, and Elizabeth M. C. Hillman. “Swept confocally-aligned planar excitation (SCAPE) microscopy for high-speed volumetric imaging of behaving organisms”. *Nature Photonics* 9.2 (Feb. 2015), pp. 113–119. DOI: [10.1038/nphoton.2014.323](https://doi.org/10.1038/nphoton.2014.323) (cit. on p. 27).
- [95] M. Temerinac-Ott, O. Ronneberger, P. Ochs, W. Driever, T. Brox, and H. Burkhardt. “Multiview Deblurring for 3-D Images from Light-Sheet-Based Fluorescence Microscopy”. *IEEE Transactions on Image Processing* 21.4 (Apr. 2012), pp. 1863–1873. DOI: [10.1109/TIP.2011.2181528](https://doi.org/10.1109/TIP.2011.2181528) (cit. on pp. 30, 55).
- [96] Stephan Preibisch, Fernando Amat, Evangelia Stamatakis, Mihail Sarov, Robert H. Singer, Eugene Myers, and Pavel Tomancak. “Efficient Bayesian-based multiview

- 5 deconvolution”. *Nature Methods* 11.6 (June 2014), pp. 645–648. DOI: 10.1038/nmeth.2929 (cit. on pp. 30, 50, 53).
- 6
- 7 [97] Bálint Balázs. “Development of a symmetric single-plane illumination micro-
8 scope”. Master’s Thesis. Hungary: Pázmány Péter Catholic University, 2013 (cit.
9 on pp. 30, 42).
- 10 [98] Sarah Frisken Gibson and Frederick Lanni. “Experimental test of an analytical
11 model of aberration in an oil-immersion objective lens used in three-dimensional
12 light microscopy”. *JOSA A* 9.1 (Jan. 1992), pp. 154–166. DOI: 10.1364/JOSAA.9.000154 (cit. on p. 48).
- 13
- 14 [99] Jizhou Li, Feng Xue, and Thierry Blu. “Fast and accurate three-dimensional point
15 spread function computation for fluorescence microscopy”. *JOSA A* 34.6 (June
16 2017), pp. 1029–1034. DOI: 10.1364/JOSAA.34.001029 (cit. on p. 48).
- 17 [100] Johannes Schindelin et al. “Fiji: an open-source platform for biological-image
18 analysis”. *Nature Methods* 9.7 (July 2012), pp. 676–682. DOI: 10.1038/nmeth.2019
19 (cit. on pp. 48, 53, 68).
- 20 [101] Janick Cardinale. *An ImageJ Plugin to Measure 3D Point Spread Functions*. 2010
21 (cit. on p. 48).
- 22 [102] Daniel Sage, Lauréne Donati, Ferréol Soulez, Denis Fortun, Guillaume Schmit,
23 Arne Seitz, Romain Guiet, Cédric Vonesch, and Michael Unser. “Deconvolution-
24 Lab2: An open-source software for deconvolution microscopy”. *Methods. Image
25 Processing for Biologists* 115 (Feb. 2017), pp. 28–41. DOI: 10.1016/j.jybmeth.2016.12.015 (cit. on p. 49).
- 26
- 27 [103] Pierre Gönczy. “Towards a molecular architecture of centriole assembly”. *Nature
28 Reviews Molecular Cell Biology* 13 (2012). DOI: 10.1038/nrm3373 (cit. on p. 50).
- 29 [104] Stephan Preibisch, Stephan Saalfeld, Johannes Schindelin, and Pavel Tomancak.
30 “Software for bead-based registration of selective plane illumination microscopy
31 data”. *Nature Methods* 7.6 (June 2010), pp. 418–419. DOI: 10.1038/nmeth0610-
32 418 (cit. on pp. 53, 64).
- 33 [105] H. Kirshner, D. Sage, and M. Unser. “3D PSF Models for Fluorescence Microscopy
34 in ImageJ”. *Proceedings of the Twelfth International Conference on Methods and
35 Applications of Fluorescence Spectroscopy, Imaging and Probes (MAF’11)*. ImageJ
1 PSF generator. Strasbourg, French Republic, Sept. 2011, p. 154 (cit. on p. 53).
- 2 [106] M. Rauzi. “Probing tissue interaction with laser-based cauterization in the early
3 developing Drosophila embryo”. *Methods in Cell Biology. Cell Polarity and Mor-
4 phogenesis* 139 (Jan. 2017), pp. 153–165. DOI: 10.1016/bs.mcb.2016.11.003
5 (cit. on p. 54).

References cited in the thesis

- [107] Uroš Kržič. “Multiple-view microscopy with light-sheet based fluorescence microscope”. PhD thesis. Germany: Ruperto-Carola University of Heidelberg, 2009 (cit. on pp. 55, 64).
- [108] M. Temerinac-Ott, O. Ronneberger, R. Nitschke, W. Driever, and H. Burkhardt. “Spatially-variant Lucy-Richardson deconvolution for multiview fusion of microscopical 3D images”. *2011 IEEE International Symposium on Biomedical Imaging: From Nano to Macro*. Mar. 2011, pp. 899–904. DOI: [10.1109/ISBI.2011.5872549](https://doi.org/10.1109/ISBI.2011.5872549) (cit. on p. 55).
- [109] Claude E. Shannon. “A mathematical theory of communication”. *The Bell System Technical Journal* 27.4 (Oct. 1948), pp. 623–656. DOI: [10.1002/j.1538-7305.1948.tb00917.x](https://doi.org/10.1002/j.1538-7305.1948.tb00917.x) (cit. on p. 56).
- [110] Claude E. Shannon. “A mathematical theory of communication”. *The Bell System Technical Journal* 27.3 (July 1948), pp. 379–423. DOI: [10.1002/j.1538-7305.1948.tb01338.x](https://doi.org/10.1002/j.1538-7305.1948.tb01338.x) (cit. on p. 56).
- [111] David A. Huffman. “A Method for the Construction of Minimum-Redundancy Codes”. *Proceedings of the IRE* 40.9 (Sept. 1952), pp. 1098–1101. DOI: [10.1109/JRPROC.1952.273898](https://doi.org/10.1109/JRPROC.1952.273898) (cit. on p. 56).
- [112] William B. Pennebaker and Joan L. Mitchell. *JPEG: Still Image Data Compression Standard*. Springer Science & Business Media, Dec. 1992 (cit. on p. 59).
- [113] M.J. Weinberger, G. Seroussi, and G. Sapiro. “The LOCO-I lossless image compression algorithm: principles and standardization into JPEG-LS”. *IEEE Transactions on Image Processing* 9.8 (Aug. 2000), pp. 1309–1324. DOI: [10.1109/83.855427](https://doi.org/10.1109/83.855427) (cit. on pp. 59, 68).
- [114] Michael D. Adams. *The JPEG-2000 still image compression standard*. 2001 (cit. on pp. 59, 68).
- [115] Anne E. Carpenter and David M. Sabatini. “Systematic genome-wide screens of gene function”. *Nature Reviews Genetics* 5.1 (Jan. 2004), pp. 11–22. DOI: [10.1038/nrg1248](https://doi.org/10.1038/nrg1248) (cit. on p. 61).
- [116] Christophe J. Echeverri and Norbert Perrimon. “High-throughput RNAi screening in cultured cells: a user’s guide”. *Nature Reviews Genetics* 7.5 (May 2006), pp. 373–384. DOI: [10.1038/nrg1836](https://doi.org/10.1038/nrg1836) (cit. on p. 61).
- [117] Rainer Pepperkok and Jan Ellenberg. “High-throughput fluorescence microscopy for systems biology”. *Nature Reviews Molecular Cell Biology* 7.9 (Sept. 2006), pp. 690–696. DOI: [10.1038/nrm1979](https://doi.org/10.1038/nrm1979) (cit. on p. 61).

- 7 [118] Eric Betzig, George H. Patterson, Rachid Sougrat, O. Wolf Lindwasser, Scott
8 Olenych, Juan S. Bonifacino, Michael W. Davidson, Jennifer Lippincott-Schwartz,
9 and Harald F. Hess. “Imaging Intracellular Fluorescent Proteins at Nanome-
10 ter Resolution”. *Science* 313.5793 (Sept. 2006), pp. 1642–1645. DOI: 10.1126/
11 science.1127344 (cit. on p. 61).
- 12 [119] Samuel T. Hess, Thanu P. K. Girirajan, and Michael D. Mason. “Ultra-High
13 Resolution Imaging by Fluorescence Photoactivation Localization Microscopy”.
14 *Biophysical Journal* 91.11 (Dec. 2006), pp. 4258–4272. DOI: 10.1529/biophysj.
15 106.091116 (cit. on p. 61).
- 16 [120] Michael J. Rust, Mark Bates, and Xiaowei Zhuang. “Sub-diffraction-limit imaging
17 by stochastic optical reconstruction microscopy (STORM)”. *Nature Methods* 3.10
18 (Oct. 2006), pp. 793–796. DOI: 10.1038/nmeth929 (cit. on p. 61).
- 19 [121] Roy Wollman and Nico Stuurman. “High throughput microscopy: from raw images
20 to discoveries”. *Journal of Cell Science* 120.21 (Nov. 2007), pp. 3715–3722. DOI:
21 10.1242/jcs.013623 (cit. on p. 61).
- 22 [122] Emmanuel G. Reynaud, Jan Peychl, Jan Huisken, and Pavel Tomancak. “Guide
23 to light-sheet microscopy for adventurous biologists”. *Nature Methods* 12.1 (Jan.
24 2015), pp. 30–34. DOI: 10.1038/nmeth.3222 (cit. on p. 61).
- 25 [123] Jeffrey M. Perkel. “The struggle with image glut”. *Nature* 533.7601 (Apr. 2016),
26 pp. 131–132. DOI: 10.1038/533131a (cit. on p. 61).
- 27 [124] John Nickolls, Ian Buck, Michael Garland, and Kevin Skadron. “Scalable Parallel
28 Programming with CUDA”. *Queue* 6.2 (Mar. 2008), pp. 40–53. DOI: 10.1145/
29 1365490.1365500 (cit. on p. 62).
- 30 [125] NVIDIA. *CUDA C Programming Guide*. Sept. 2015 (cit. on p. 62).
- 31 [126] Gustavo Q. G. de Medeiros. “Deep tissue light-sheet microscopy”. PhD thesis.
32 Germany: Ruperto-Carola University of Heidelberg, 2016 (cit. on p. 63).
- 33 [127] Eugen Baumgart and Ulrich Kubitscheck. “Scanned light sheet microscopy with
34 confocal slit detection”. *Optics Express* 20.19 (2012), pp. 21805–21814. DOI: 10.
35 1364/0E.20.021805 (cit. on p. 63).
- 36 [128] Stephan Preibisch, Stephan Saalfeld, Torsten Rohlfing, and Pavel Tomancak.
1 “Bead-based mosaicing of single plane illumination microscopy images using ge-
2 ometric local descriptor matching”. Ed. by Josien P. W. Pluim and Benoit M.
3 Dawant. Feb. 2009, 72592S. DOI: 10.1117/12.812612 (cit. on p. 64).
- 4 [129] International Telecommunications Union. *H.265 : High efficiency video coding*.
5 Dec. 2016 (cit. on p. 68).

References cited in the thesis

- [130] Douglas W. Cromejy. “Digital Images Are Data: And Should Be Treated as Such”. *Methods in molecular biology (Clifton, N.J.)* 931 (2013), pp. 1–27. DOI: 10.1007/978-1-62703-056-4_1 (cit. on p. 68).
- [131] Khalid Sayood. *Introduction to Data Compression, Fourth Edition*. 4th ed. The Morgan Kaufmann Series in Multimedia Information and Systems. Morgan Kaufmann, 2012 (cit. on p. 68).
- [132] D. Santa-Cruz and T. Ebrahimi. “A study of JPEG 2000 still image coding versus other standards”. *2000 10th European Signal Processing Conference*. Sept. 2000, pp. 1–4 (cit. on p. 68).
- [133] Fernando Amat, Burkhard Höckendorf, Yinan Wan, William C. Lemon, Katie McDole, and Philipp J. Keller. “Efficient processing and analysis of large-scale light-sheet microscopy data”. *Nature Protocols* 10.11 (Nov. 2015), pp. 1679–1696. DOI: 10.1038/nprot.2015.111 (cit. on p. 68).
- [134] Tobias Pietzsch, Stephan Saalfeld, Stephan Preibisch, and Pavel Tomancak. “Big-DataViewer: visualization and processing for large image data sets”. *Nature Methods* 12.6 (June 2015), pp. 481–483. DOI: 10.1038/nmeth.3392 (cit. on p. 68).
- [135] Z. Wang, M. Klaiber, Y. Gera, S. Simon, and T. Richter. “Fast lossless image compression with 2D Golomb parameter adaptation based on JPEG-LS”. *Signal Processing Conference (EUSIPCO), 2012 Proceedings of the 20th European*. Aug. 2012, pp. 1920–1924 (cit. on p. 68).
- [136] Roman Starosolski. “Simple fast and adaptive lossless image compression algorithm”. *Software: Practice and Experience* 37.1 (Jan. 2007), pp. 65–91. DOI: 10.1002/spe.746 (cit. on p. 68).
- [137] P. G. Howard and J. S. Vitter. “Fast and efficient lossless image compression”. *[Proceedings] DCC ‘93: Data Compression Conference*. 1993, pp. 351–360. DOI: 10.1109/DCC.1993.253114 (cit. on p. 68).
- [138] Marc Treib, Florian Reichl, Stefan Auer, and Rüdiger Westermann. “Interactive Editing of GigaSample Terrain Fields”. *Computer Graphics Forum* 31.2pt2 (May 2012), pp. 383–392. DOI: 10.1111/j.1467-8659.2012.03017.x (cit. on p. 68).
- [139] M. Treib, K. Burger, F. Reichl, C. Meneveau, A. Szalay, and R. Westermann. “Turbulence Visualization at the Terascale on Desktop PCs”. *IEEE Transactions on Visualization and Computer Graphics* 18.12 (Dec. 2012), pp. 2169–2177. DOI: 10.1109/TVCG.2012.274 (cit. on p. 68).
- [140] J. Rissanen and G. Langdon. “Universal modeling and coding”. *IEEE Transactions on Information Theory* 27.1 (Jan. 1981), pp. 12–23. DOI: 10.1109/TIT.1981.1056282 (cit. on p. 69).

- 9 [141] Robert A. Gowen and Alan Smith. “Square root data compression”. *Review of*
 10 *Scientific Instruments* 74.8 (Aug. 2003), pp. 3853–3861. DOI: 10.1063/1.1593811
 11 (cit. on p. 69).
- 12 [142] Gary M. Bernstein, Chris Bebek, Jason Rhodes, Chris Stoughton, R. Ali Van-
 13 derveld, and Penshu Yeh. “Noise and bias in square-root compression schemes”.
 14 *Publications of the Astronomical Society of the Pacific* 122.889 (Mar. 2010). arXiv:
 15 0910.4571, pp. 336–346. DOI: 10.1086/651281 (cit. on p. 69).
- 16 [143] R. M. Gray and D. L. Neuhoff. “Quantization”. *IEEE Transactions on Information*
 17 *Theory* 44.6 (Oct. 1998), pp. 2325–2383. DOI: 10.1109/18.720541 (cit. on p. 69).
- 18 [144] F. J. Anscombe. “The Transformation of Poisson, Binomial and Negative-
 19 Binomial Data”. *Biometrika* 35.3-4 (Dec. 1948), pp. 246–254. DOI: 10.1093/
 20 biomet/35.3-4.246 (cit. on p. 69).
- 21 [145] M. Makitalo and A. Foi. “Optimal Inversion of the Anscombe Transformation in
 22 Low-Count Poisson Image Denoising”. *IEEE Transactions on Image Processing*
 23 20.1 (Jan. 2011), pp. 99–109. DOI: 10.1109/TIP.2010.2056693 (cit. on p. 69).
- 24 [146] M. Makitalo and A. Foi. “A Closed-Form Approximation of the Exact Unbiased
 25 Inverse of the Anscombe Variance-Stabilizing Transformation”. *IEEE Transac-*
 26 *tions on Image Processing* 20.9 (Sept. 2011), pp. 2697–2698. DOI: 10.1109/TIP.
 27 2011.2121085 (cit. on p. 69).
- 28 [147] M. Makitalo and A. Foi. “Optimal Inversion of the Generalized Anscombe Trans-
 29 formation for Poisson-Gaussian Noise”. *IEEE Transactions on Image Processing*
 30 22.1 (Jan. 2013), pp. 91–103. DOI: 10.1109/TIP.2012.2202675 (cit. on p. 69).
- 31 [148] C. Sommer, C. Straehle, U. Köthe, and F. A. Hamprecht. “Ilastik: Interac-
 32 tive learning and segmentation toolkit”. *2011 IEEE International Symposium*
 33 *on Biomedical Imaging: From Nano to Macro*. Mar. 2011, pp. 230–233. DOI:
 34 10.1109/ISBI.2011.5872394 (cit. on p. 70).
- 35 [149] Thorvald Julius Sørensen. *A method of establishing groups of equal amplitude*
 36 *in plant sociology based on similarity of species content and its application to*
 1 *analyses of the vegetation on Danish commons*. København: I kommission hos E.
 2 Munksgaard, 1948 (cit. on p. 71).
- 3 [150] Lee R. Dice. “Measures of the Amount of Ecologic Association Between Species”.
 4 *Ecology* 26.3 (July 1945), pp. 297–302. DOI: 10.2307/1932409 (cit. on p. 71).
- 5 [151] Romain Fernandez, Pradeep Das, Vincent Mirabet, Eric Moscardi, Jan Traas,
 6 Jean-Luc Verdeil, Grégoire Malandain, and Christophe Godin. “Imaging plant
 7 growth in 4D: robust tissue reconstruction and lineaging at cell resolution”. *Nature*
 8 *Methods* 7.7 (July 2010), pp. 547–553. DOI: 10.1038/nmeth.1472 (cit. on p. 71).

REFERENCES

- 9 [152] Joran Deschamps, Markus Mund, and Jonas Ries. “3D superresolution microscopy
10 by supercritical angle detection”. *Optics Express* 22.23 (Nov. 2014), pp. 29081–
11 29091 (cit. on p. 74).
- 12 [153] Mike Heilemann, Sebastian van de Linde, Mark Schüttelpelz, Robert Kasper,
13 Britta Seefeldt, Anindita Mukherjee, Philip Tinnefeld, and Markus Sauer.
14 “Subdiffraction-Resolution Fluorescence Imaging with Conventional Fluorescent
15 Probes”. *Angewandte Chemie International Edition* 47.33 (Aug. 2008), pp. 6172–
16 6176. DOI: 10.1002/anie.200802376 (cit. on p. 74).
- 17 [154] Joran Deschamps, Andreas Rowald, and Jonas Ries. “Efficient homogeneous illu-
18 mination and optical sectioning for quantitative single-molecule localization mi-
19 croscopy”. *Optics Express* 24.24 (Nov. 2016), pp. 28080–28090. DOI: 10.1364/OE.
2298 24.028080 (cit. on p. 75).
- 2299 [155] I. Izeddin, J. Boulanger, V. Racine, C. G. Specht, A. Kechkar, D. Nair, A. Triller,
2300 D. Choquet, M. Dahan, and J. B. Sibarita. “Wavelet analysis for single molecule
2301 localization microscopy”. *Optics Express* 20.3 (Jan. 2012), pp. 2081–2095 (cit. on
2302 p. 75).
- 2303 [156] Carlas S. Smith, Nikolai Joseph, Bernd Rieger, and Keith A. Lidke. “Fast, single-
2304 molecule localization that achieves theoretically minimum uncertainty”. *Nature
2305 Methods* 7.5 (May 2010), pp. 373–375. DOI: 10.1038/nmeth.1449 (cit. on p. 75).
- 2306 [157] Jeremy C. Simpson et al. “Genome-wide RNAi screening identifies human proteins
2307 with a regulatory function in the early secretory pathway”. *Nature Cell Biology*
2308 14.7 (July 2012), pp. 764–774. DOI: 10.1038/ncb2510 (cit. on p. 85).